NOVEL ^{1}H MR PROBES TO INTERROGATE THE TUMOR MICROENVIRONMENT

by

PRAVEEN K. GULAKA

Presented to the Faculty of the Graduate School of

The University of Texas at Arlington in Partial Fulfillment

of the Requirements

for the Degree of

DOCTOR OF PHILOSOPHY

THE UNIVERSITY OF TEXAS AT ARLINGTON

August 2011

ACKNOWLEDGEMENTS

During the last 4 years there have been many people who contributed directly or indirectly to this work. To all of them, named or unnamed, I like to express my gratitude and deepest appreciation.

First and foremost, I would like to thank my mentor and advisor, Dr. Vikram D. Kodibagkar for training me to be a good researcher. I am grateful for his constant encouragement and advice. His insightful thinking and passion towards solving problems will always be an inspiration to me.

I would like to thank my committee members Dr. Ralph Mason, Dr. Hanli Liu, Dr. A. Dean Sherry, Dr. Hanzhang Lu and Dr. Robert Eberhart for the stimulating discussions and guidance over the years.

I am indebted to my lab mate Sairam Geethanath, student colleagues of the BME & RDS program and research staff of the Laboratory of Prognostic Radiology (LPR) for providing a stimulating and enjoyable work environment. I am also grateful to the administrative staff of the departments of biomedical engineering (BME at UTA – UTSW) and Advanced Radiological Sciences (UTSW) for assisting me in many different ways.

Lastly, and most importantly, I wish to thank my family for their unconditional love and support during all my endeavors. Anything and everything I have accomplished so far, is due to their support.

July 28, 2011

ABSTRACT

NOVEL ^{1}H MR PROBES TO INTERROGATE THE TUMOR MICROENVIRONMENT

Praveen K. Gulaka, PhD

The University of Texas at Arlington, 2011

Supervising Professor: Vikram D. Kodibagkar

The term “tumor microenvironment” usually refers to the description of the physiological and metabolic conditions within solid tumors (primary or metastatic), and is significantly different from that of normal tissues. Assessment of factors like pH, tissue oxygen tension (pO_2) and gene expression in the tumor microenvironment and the ability to image them *in vivo* can provide useful prognostic information. For example, hypoxia (low pO_2), typically distributed heterogeneously in solid tumors, is known to affect both radiation sensitivity and the development of metastases thereby influencing the response to treatment. This dissertation research focuses on the evaluation of novel probes to interrogate the tumor microenvironment using proton (^{1}H) magnetic resonance imaging (MRI), specifically hypoxia and gene expression.

For the assessment of hypoxia, hexamethyldisiloxane (HMDSO) has been reported as a ^{1}H MR based pO_2 reporter molecule by *in vivo* spectroscopy and imaging using Proton Imaging of Siloxanes to Map Tissue Oxygenation Levels (PISTOL) technique. In further improvement of the technique, I evaluated HMDSO based nanoemulsions and various other siloxanes as quantitative ^{1}H MR pO_2 reporter molecules (Chapter 2). These reporter molecules

exhibited a linear dependence of the spin lattice relaxation rate (R_1) on pO_2. HMDSO based nanoemulsions were further used in an *in vivo* feasibility study showing dynamic changes in rat thigh tissue oxygenation following an intramuscular injection in response to hyperoxic gas (normobaric and hyperbaric oxygen) breathing, thus showing the feasibility for use of these nanoemulsions as pO_2 nanoprobes for systemic delivery.

Another strategy for hypoxia imaging has been the use of 2-nitroimidazole based agents which selectively accumulated in hypoxic regions. In this dissertation, I report the *in vitro* and *in vivo* evaluation of GdDOTA monoamide conjugate of 2-nitroimidazole, GdDO3NI, as a novel hypoxia targeting MRI T_1 contrast agent (Chapter 3). A higher uptake of GdDO3NI was observed in cells incubated under hypoxic conditions as well as hypoxic regions of Dunning R3327 AT1 prostate tumors. The MR observations were validated through inductively coupled plasma mass spectroscopic analysis. Further, I demonstrated the ability of GdDO3NI in monitoring the effect of hyperoxic (100% oxygen) gas breathing on modifying hypoxia in AT1 and HI tumors. Thus, GdDO3NI shows promise as a hypoxia targeting small molecular contrast agent, enabling the assessment of hypoxia at very high spatial resolution.

For the assessment of gene expression, development of noninvasive imaging based reporter molecules has been an active area of study. In this dissertation, I evaluated a novel platform with enhanced T_1 and T_2 relaxation properties, for detecting β-gal activity in *lacZ* transfected cells using novel analogs of the product of cleavage of commercially available substrate S-Gal® (Chapter 4). The synthesized mono and di- galactopyranosides (MGD and GD respectively) showed differential relaxation enhancements *in vitro* and the molecule C3-GD was identified as the optimal candidate for *in vivo* studies. Following intra-tumoral injection of C3-GD and ferric ammonium citrate solution in the *lacZ* transfected tumors, a pronounced shortening of T_1 & T_2 values was observed when compared to baseline, and persisted over 2 hours. This is attributed to the formation of an iron complex following chelation of aglycones produced by β-gal activity. Thus C3-GD shows great promise as a ^{1}H MR gene reporter molecule.

TABLE OF CONTENTS

LIST OF ILLUSTRATIONS

Figure Page

LIST OF TABLES

CHAPTER 1

INTRODUCTION

1.1 Tumor microenvironment

Cancer is a disease characterized by uncontrolled proliferation of abnormal cells with reduced apoptosis and potential to metastasize. In most cases, this uncontrolled cell growth causes the formation of tumors, either solid or dispersed (1). In solid tumors, cancer cells proliferate in one place forming a mass which might further metastasize to other organs (e.g. cancers of lung, breast, prostate, brain etc). In dispersed or non – solid tumors the abnormal cells are dispersed throughout the body (e.g. leukemias, lymphomas).

The term “tumor microenvironment” usually refers to the description of the physiological and metabolic conditions within solid tumors (primary or metastatic), and is significantly different from that of normal tissues (2). These differences arise due to the irregular vasculature of tumors causing significant perfusion heterogeneities resulting in hypoxic regions. Changes in acid – base homeostasis results in reduced buffering capacity of tumor interstitial fluid when compared to normal tissue and this, in combination with poor perfusion and increased lactic acid secretion (3) results in acidic extracellular pH (pH_e) in tumors . The low pH_e and low tissue oxygen tension (pO_2) in tumor microenvironment have been shown to up-regulate proteolytic enzyme expression and enhance their enzymatic activities (4). Collectively these factors, promote metastasis and invasion, inhibit DNA repair mechanisms and induce resistance to therapies (5).

As the tumor microenvironment has such a crucial role in carcinogenesis and metastasis, it represents a target not only for cancer therapy but also for preventive strategies. Therefore, accurate noninvasive imaging of pO_2, pH, perfusion, enzymatic and metabolic characteristics in the tumor microenvironment are critical. This dissertation research primarily

focuses on the *in vitro* and *in vivo* evaluation of novel probes to interrogate the tumor microenvironment using proton (^{1}H) magnetic resonance imaging (MRI), specifically hypoxia and gene expression.

1.1.1 Vasculature and oxygenation

Tumor vasculature is created through two processes: cooption of normal vasculature and angiogenesis. The first process, cooption of normal vasculature, occurs because the tumors are abnormal cells that gradually replace the normal tissue. The second means of forming tumor vasculature, angiogenesis, occurs due to the biochemical signals sent by the tumor cells to the nearby vessels when they outgrow the diffusion distance of oxygen (6). Additionally, due to the rapid growth of the tumors, the blood vessels tend to be poorly or abnormally developed.

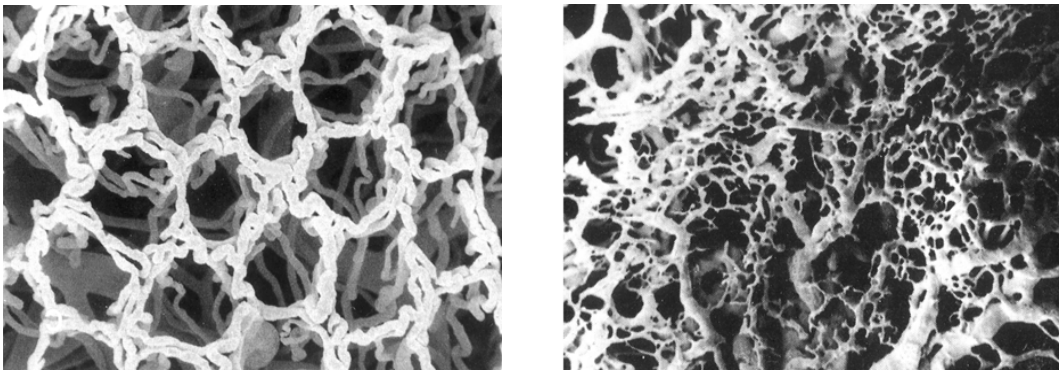

(a) (b)

Figure 1.1 Scanning electron microscopic images of vascular casts of a) Normal colon tissue and b) nearby colorectal cancer [Adapted from (7)].

This abnormal / immature vasculature typically has characteristics such as increased permeability, vessel diameter, vessel length, vessel density and tortuosity resulting from incomplete endothelium, lack of pericytes and other components of the vessel wall (8).

All these factors make tumor vasculature both structurally and functionally different from normal vessels and lead to an impaired oxygen supply to tumor cells. This reduction in supply compounded by the increase in consumption leads to creation of hypoxic (pO_2 < 10 mmHg) regions in tumors. Another important characteristic of tumor microenvironment is the dearth of lymphatic vessels. This leads to a decrease in the drainage of interstitial fluids and to an increase of interstitial pressure; causing some of the tumor blood vessels to collapse, further reducing the supply of oxygen and nutrients to tumor cells.

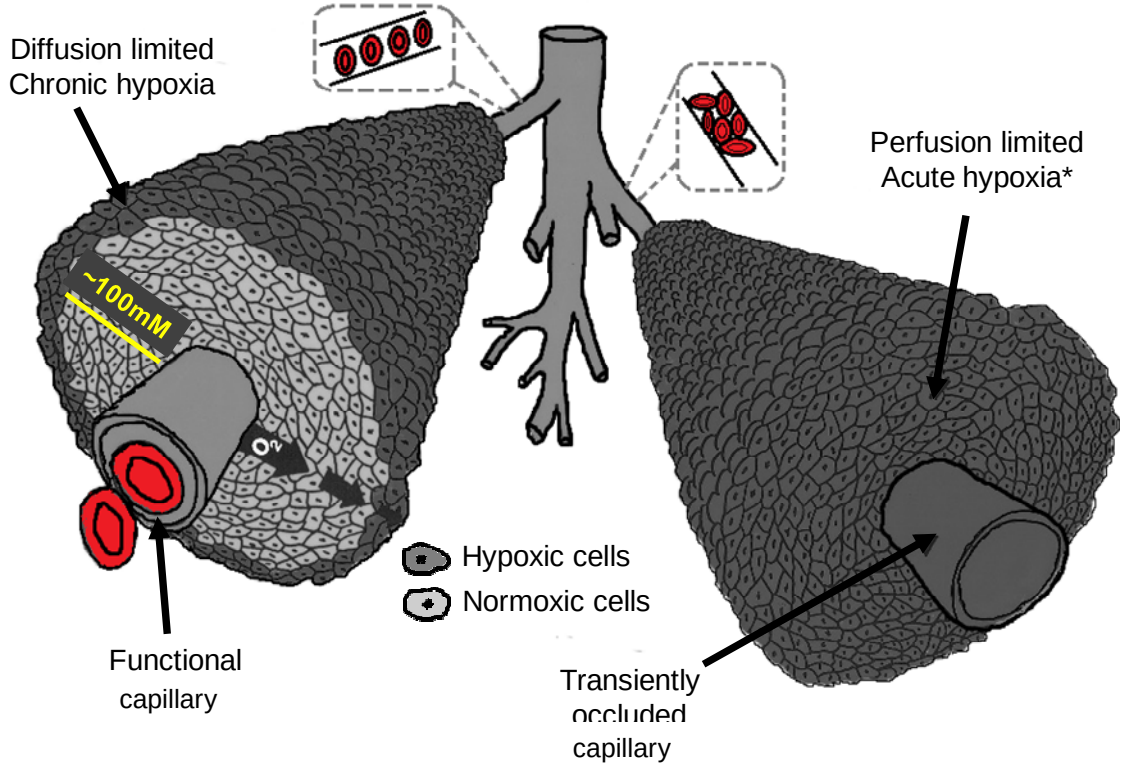

Figure 1.2 Schematic illustration of tumor cells growing around feeding capillaries from which the cells receive their oxygen and nutrient supply. The left side shows that as oxygen diffuses out from the vessel it is consumed thus creating an oxygen gradient, with the outermost viable cells becoming oxygen deprived or chronically hypoxic. On the right side, blood perfusion through the vessel has been temporarily stopped, thus making all the cells oxygen deprived or acutely hypoxic. Figure modified from (9).

Consequently, tumor tissues are characterized by the presence of two types of hypoxia. Limited diffusion of oxygen into tissues due to the particular characteristics of tumor vasculature generates chronic hypoxia also termed diffusion limited hypoxia. Alternatively, poor blood perfusion in the tumor blood vessels leads to acute hypoxia also known as perfusion limited or cyclic hypoxia (Fig 1.2).

1.1.2 Significance of measuring pO_2 and enzyme activity.

Oxygen delivery is crucial for the efficient functioning of most tissues. Hypoxia or low tissue oxygen tension (pO_2 < 10 mmHg) has been shown to promote the malignant progression of cancer, induce genes promoting angiogenesis, and reduce the efficacy of various therapies (10-12). There is increasing evidence for tumor hypoxia as a powerful physiological stimulus that can be exploited as a tumor-specific condition, allowing for the design of hypoxia-activated anticancer drugs (13) or novel hypoxia-regulated gene therapy strategies (14). A strong argument therefore exists for assessing the hypoxic fraction of tumors prior to patient treatment, and to tailor this treatment accordingly. It has been hoped that modulation of tumor oxygenation could be applied to enhance therapeutic efficacy, but till now effective oximetry methods have been lacking in the clinic. Thus, the opportunity to measure pO_2 noninvasively may be significant in understanding mechanisms of tissue function and in clinical prognosis.

The acidic pH_e and hypoxia in the tumor microenvironment have been implicated in activating several transcription factors (e.g; HIF-1) leading to the up-regulation of various genes encoding matrix degrading enzymes (e.g; matrix metalloproteinases –MMPs, cathepsins etc) (15). These enzymes are known to promote invasive growth and metastasis of tumors (4). Therefore there exists a strong need for the development of noninvasive imaging methods based on appropriate reporter molecules, to assess gene expression through enzymatic activity thereby enabling gene therapy.

1.1.3 Existing methods for measuring pO_2

Many MR and non-MR based techniques have been developed to assess tumor oxygenation as reviewed recently (16,17). Non-MR-based methods include: polarographic oxygen electrodes (18), fluorescence imaging (19), phosphorescence quenching (20), near-infrared spectroscopy (21), SPECT (22) and PET (23,24) imaging. MR-based methods include: blood oxygen level dependent (BOLD) imaging (25), electron paramagnetic resonance (EPR/ESR) (26), fluorocarbon relaxometry (27) using echo planar imaging for dynamic oxygen mapping (FREDOM) (28). MRI based approaches are particularly suitable for noninvasive, multiple, repeat measurements to observe dynamic changes in tissue oxygenation in response to intervention. Another popular way of assessing hypoxia exploits the principle of selective enzyme mediated reduction of nitro group of 2-nitroimidazole containing compounds under hypoxic conditions (16). Currently, [^{18}F]Fluoromisonidazole (^{18}F-MISO) (29,30) and Cu-labelled diacetyl-bis (*N*(4)- methyl thiosemicarbazone (Cu-ATSM) (23) are being used as hypoxia targeting PET imaging agents whereas [^{19}F] Tri-Fluoromisonidazole (TF- MISO) (31) has been used an MRI technique to qualitatively image hypoxia.

1.2 Magnetic resonance relaxometry

Introduction of a sample into a magnetic field, B_0, causes the nuclear spins to precess about B_0 along the field direction. Excitation by an RF pulse forces the magnetic moments (consequently, the magnetization vector) into phase unity, while increasing the angle between the magnetization vector and the B_0 field. Relaxation is the process by which the magnetization returns to its equilibrium configuration. Recovery of the magnetization along the longitudinal axis of the B_0 field is called T_1 relaxation and the loss of phase coherence in the transverse plane is described by T_2 relaxation. Relaxometry is the study of measuring characteristic relaxation parameters with NMR or MRI.

1.2.1 Spin-lattice (Longitudinal) relaxation

The term spin-lattice or longitudinal (T_1) relaxation refers to the recovery of the magnetization component parallel to the external field following an RF excitation (Fig 1.3). During the longitudinal relaxation process, spins dissipate extra energy (absorbed from the excitation RF pulse) to their environment through spin-lattice interaction. This relaxation process as represented in Eqn [1.1] is governed by an exponential time constant T_1, which can be measured by saturation recovery (90° RF pulse, a=1) or inversion recovery (180° RF pulse, a=2) based sequences.

$$M_z(t) = M_0\left(1-ae^{-t/T_1}\right) \qquad [1.1]$$

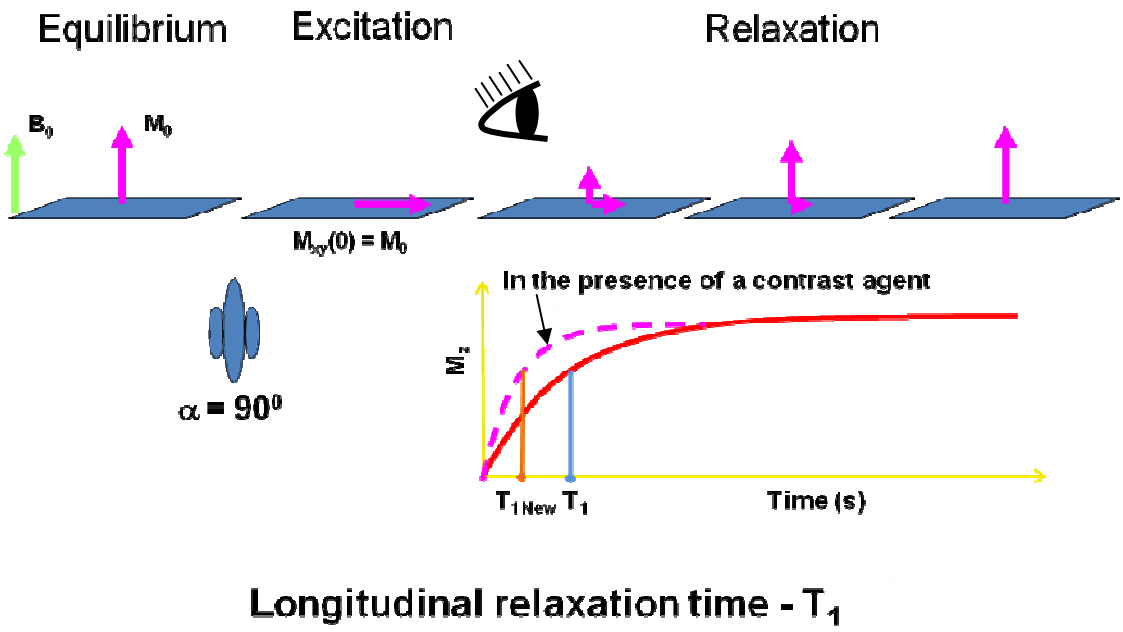

Figure 1.3 Schematic of the T_1 relaxation process following excitation by a 90° R F pulse.

1.2.2 Spin-spin (Transverse) relaxation

Spin-spin or transverse relaxation is the process by which the magnetization in the transverse plane loses its phase coherence. Excitation of the net magnetization by a 90° RF pulse, flips the magnetization, M_0, into the transverse plane with phase coherence. Following this, spins experience fluctuating dipole fields generated by the random motions of neighboring nuclei. During this stochastic process, spins gradually collect different phases (dephasing) and lose coherence manifesting into the attenuation of MR signal. This process follows an exponential decay characterized by the transverse relaxation time constant T_2 as in Eqn [1.2].

$$M_{xy}(t) = M_0\, e^{-t/T_2} \qquad [1.2]$$

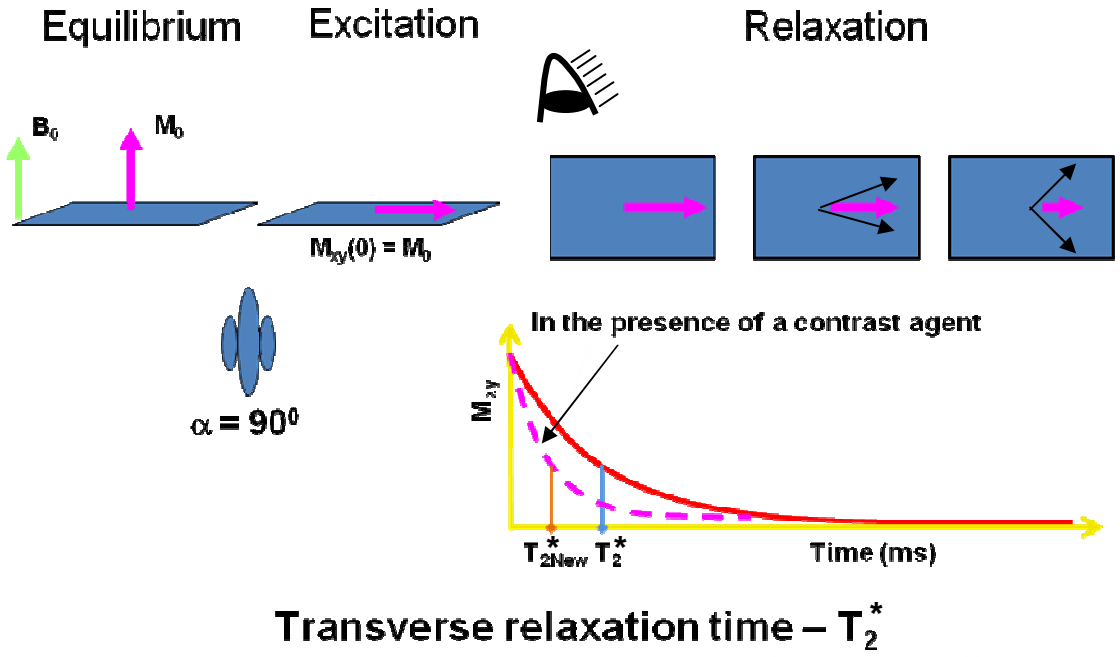

Figure 1.4 Schematic of the T_2* relaxation process following excitation by a 90° RF pulse.

While T_2 relaxation is inherently a stochastic process arising from the random Brownian motion of molecules, additional dephasing could happen as a result of molecular diffusion, field

inhomogeneities and susceptibility gradients. This results in a shortened relaxation time called apparent transverse relaxation time (Fig 1.4) and denoted as T_2*. Dephasing due to magnetic field inhomogeneities is determinative and its effect can be removed by applying a 180° RF pulse. Therefore, the 'true' transverse relaxation time T_2 is measured using a spin echo (SE) sequence with a 180° refocusing pulse, while the ap parent transverse relaxation time T_2* is measured using a gradient echo (GRE) sequence without a 180° refocusing pulse.

1.2.3 Paramagnetic relaxation enhancement

Paramagnetic species are substances which have unpaired electrons giving rise to a permanent magnetic moment. In the absence of an applied magnetic field, these magnetic moments align randomly but in the presence of an externally applied magnetic field, they align in the field direction. The local magnetic field fluctuations produced by paramagnetic substances enhances relaxation thereby shortens the spin-lattice (T_1) and spin-spin relaxation times (T_2) of neighboring nuclei. This process is termed as paramagnetic relaxation enhancement (PRE) (32). The paramagnetic contrast agents used to date are molecular oxygen, stable free radicals (ex. nitroxide radical) and metal ions (ex. many transition metal ions and lanthanides).

The paramagnetic relaxation of the solvent nuclei originates from the dipole-dipole interactions between the solvent nuclear spins and the fluctuating local magnetic field caused by the unpaired electron spins of the paramagnetic contrast agent. Therefore relaxation rates ($R_1 = 1/T_1$ and $R_2 = 1/T_2$) observed for solvent nuclei in the presence of paramagnetic solute substances can be attributed to the diamagnetic (intrinsic) and paramagnetic (additional) relaxations as given by Eqn [1.3].

$$R_{i,\,obsd} = R_{i,\,d} + R_{i,\,p} \qquad i = 1, 2 \qquad [1.3]$$

where $R_{i,\ obsd}$ is the observed relaxation solvent relaxation rate in the presence of paramagnetic species, $R_{i,\ d}$ is the diamagnetic solvent relaxation rate in the absence of a paramagnetic species and $R_{i,\ p}$ is the relaxation due to paramagnetic contributions.

In the absence of solute-solute interactions, the solvent relaxation rates are linearly proportional to the concentration of the paramagnetic species [M] given by Eqn [1.4]

$$R_{i,\ obsd} = R_{i,\ d} + r_i[M] \qquad i = 1,\ 2 \qquad [1.4]$$

where 'r_i' is the relaxivity which is defined as slope of the relaxation rate and concentration curve.

Further, solvent interaction with the metal ion is classified into three types (Fig 1.5): (1) primary coordination sphere (inner-sphere relaxation), (2) hydrogen-bonded molecules in the secondary coordination sphere, and (3) bulk solvent that translationally diffuses past the metal ion (outer-sphere relaxation).

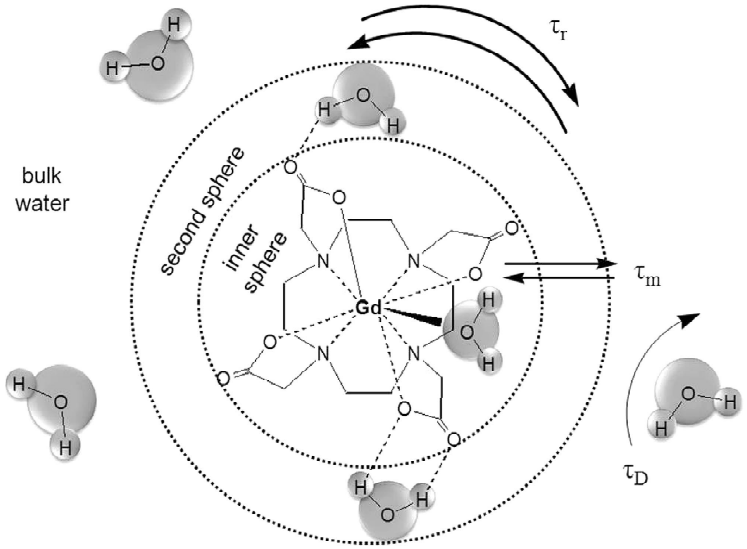

Figure 1.5 Schematic showing the relaxation coordination spheres of water: inner-sphere, secondary-sphere, and bulk water in the presence of a paramagnetic Gadolinium chelate [Adapted from (33)].

The inner sphere contribution is due to the interactions between paramagnetic electron spins and the solvent nuclei in the first coordination sphere of the metal ion that are in constant exchange with the bulk solvent. Second coordination sphere contribution to relaxation is not well understood. It is often combined with the relaxation due to translational diffusion of solvent molecules past the metal ion and termed as outer-sphere relaxation. Therefore the total paramagnetic relaxation enhancement can be given by Eqn [1.5]

$$R_{i,\,p} = R_{i,\,\text{inner-sphere}} + R_{i,\,\text{outer-sphere}} \qquad i = 1, 2 \qquad [1.5]$$

According to the Solomon, Bloembergen and Morgan theory, the inner-sphere contributions to longitudinal and transverse relaxation can be expressed as functions of the mole fraction of metal ion per solvent molecule (P_m), the number of solvent nuclei per metal ion (q), and the average residence time of the solvent molecule in the complex (τ_m, the reciprocal of the solvent exchange rate) given by Eqns [1.6] and [1.7].

$$\frac{1}{T_{1,\,\text{inner-sphere}}} = \frac{P_m q}{T_{1m} + \tau_m} \qquad [1.6]$$

$$\frac{1}{T_{2,\,\text{inner-sphere}}} = qP_m \frac{1}{\tau_m}\left[\frac{T_{2m}^{-1}\left(\tau_m^{-1} + T_{2m}^{-1}\right) + \Delta\omega_m^2}{\left(\tau_m^{-1} + T_{2m}^{-1}\right)^2 + \Delta\omega_m^2}\right] \qquad [1.7]$$

The “m” subscript in Eqn [1.7] refers to the solvent molecule in the inner-sphere, and $\Delta\omega_m$ is the difference in Larmor frequencies between the inner coordination sphere and the bulk solvent reference.

Outer-sphere relaxation is often described by translational diffusion of the solvent molecules past the metal complex. This contribution to relaxation is approached based upon a

rigid-sphere model where the solvent molecules and metal complex are treated as hard spheres (33).

T_1 relaxation observed by using Gd^{3+} -based MR contrast agents is predominantly due to the inner- sphere relaxation mechanism. T_2 / T_2* relaxation observed when using super paramagnetic iron oxide particles is due to outer-sphere relaxation (34). These particles exhibit very high magnetic moments due to cooperative alignment of electron spins of individual ions causing fluctuating dipole interactions with surrounding nuclear spins (altering water relaxation).

1.2.4 Quantitative MR oximetry using PISTOL

Quantitative MR oximetry based on exogenous pO_2 reporter molecules (35) has been shown to be an extremely useful, minimally invasive technique for tumor stratification based on response to hyperoxic gas breathing (35). Molecular oxygen is paramagnetic and therefore tends to shorten nuclear spin-lattice relaxation times, T_1, in solution or *in vivo*. Most of the NMR oximetry applications utilize the linear dependence of the longitudinal (spin-lattice) relaxation rate ($R_1=1/T_1$) of reporter molecules on the partial pressure of oxygen (35). Two essential characteristics of the reporter molecules that are critical for *in vivo* oximetry are high oxygen solubility and hydrophobicity. Hydrophobicity ensures the exchange of gases between the reporter molecule and surrounding tissue, while preventing the exchange of aqueous ions, which could affect R_1. Most perfluorocarbons (PFCs) and siloxanes (linear and cyclic polymers of HMDSO) satisfy these criteria.

Our research group has previously measured tumor oxygen dynamics with respect to growth and respiratory challenge by ^{19}F spectroscopy and imaging (28,36-41). The technology using the reporter molecule, hexaflurobenzene, exploits the exceptional response of the ^{19}F NMR spin-lattice relaxation rate to changes in oxygen tension (38). The technique has many virtues for investigating solid tumors in animals. Unfortunately, most centers do not currently have a clinical MR system with ^{19}F MR capabilities and this has impeded the use of ^{19}F -

based tissue oximetry in the clinical setting. Hence, ^{1}H pO_2 reporter molecules could be valuable clinical tools to routinely measure tissue oxygenation.

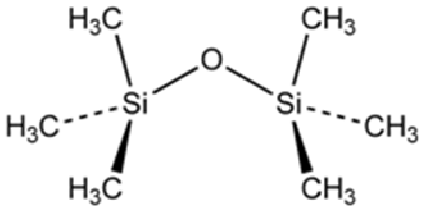

(a)

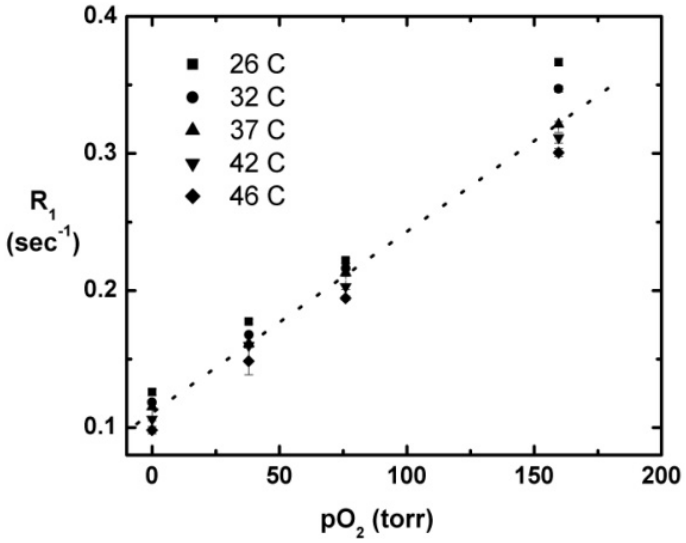

(b)

Figure 1.6 a) Structure of hexamethyldisiloxane (HMDSO). b) Effect of temperature on the relationship between R_1 and pO_2 of HMDSO. Linear fit to data at 37 ℃ (dotted line) from 0-160 torr yields R_1 [s^{-1}] = 0.1126 + 0.0013* pO_2 [torr] (R^2>0.999).

Dr. Kodibagkar and our group has previously identified the potential of hexamethyldisiloxane (HMDSO) as a ^{1}H based pO_2 reporter molecule by *in vivo* spectroscopy (42) and imaging (43) using Proton Imaging of Siloxanes to Map Tissue Oxygenation Levels (PISTOL) technique. HMDSO (Fig 1.6a) has a single ^{1}H resonance and shows exceptional

sensitivity to changes in pO_2 with relatively little response to temperature (Fig 1.6b). The linear dependence of HMDSO R_1 on pO_2 can be explained by considering two pools of protons, those with and without oxygen in their vicinity. The protons free of oxygen have a diamagnetic longitudinal relaxation rate of R_{1d}, the ones in the vicinity of have a longitudinal relaxation rate of $R_{1d} + R_{1p}$, where R_{1p} is the paramagnetic contribution of oxygen. Since the oxygen molecules rapidly diffuse in the solvent, the observed relaxation rate for each type of proton is a molar weighted average. If x is the molar fraction of dissolved oxygen, the net relaxation rate can be defined as

$$R_1 = (1 - x) * R_{1d} + x * (R_{1d} + R_{1p}) = R_{1d} + x * R_{1p} \quad [1.8]$$

where R_1 = net relaxation rate of the probe.

R_{1d} = anoxic component of the relaxation rate.

R_{1p} = Paramagnetic component of the relaxation rate due to contribution of oxygen.

As per Henry's law, the dissolved mole fraction is directly related to the partial pressure of oxygen.

$$pO_2 = k * x \quad [1.9]$$

where k is a constant that determines the solubility of oxygen. Thus the net relaxation rate becomes a linear dependence of R_1 on pO_2

$$R_1 = A' + B' * pO_2 \quad [1.10]$$

with the intercept of A' = R_{1d} and a slope of B' (= R_{1p} / k).

Since longitudinal relaxation rate is a function of temperature we assume a linear dependence of constants A' and B' on temperature (for relevant physiological range) which empirically can be defined as in Eqn [1.11]

$$A' = A + C * T \quad [1.11]$$

$$B' = B + D * T$$

Substituting value of A' and B' in Eqn [1.10] results in a temperature dependent model (Eqn [1.12]) for net relaxation rate R_1

$$R_1 = A + B * pO_2 + C * T + D * T * pO_2 \qquad [1.12]$$

Using this equation oxygenation levels and errors in pO_2/°C at a particular oxygenation level or temperature can be determined quantitatively, leading to accurate and reliable quantification.

For imaging of tissue oxygenation, our group developed the PISTOL pulse sequence (43) (Fig 1.7). It consists of a) 20 non-selective saturation pulses followed by a delay *tau (τ)* for magnetization recovery, b) 3 CHESS pulses for optional frequency selective saturation of water and fat immediately followed by c) a spin-echo EPI acquisition, consisting of a frequency selective $\pi/2$ pulse (on-resonance for HMDSO), a slice selective π pulse, and an EPI readout.

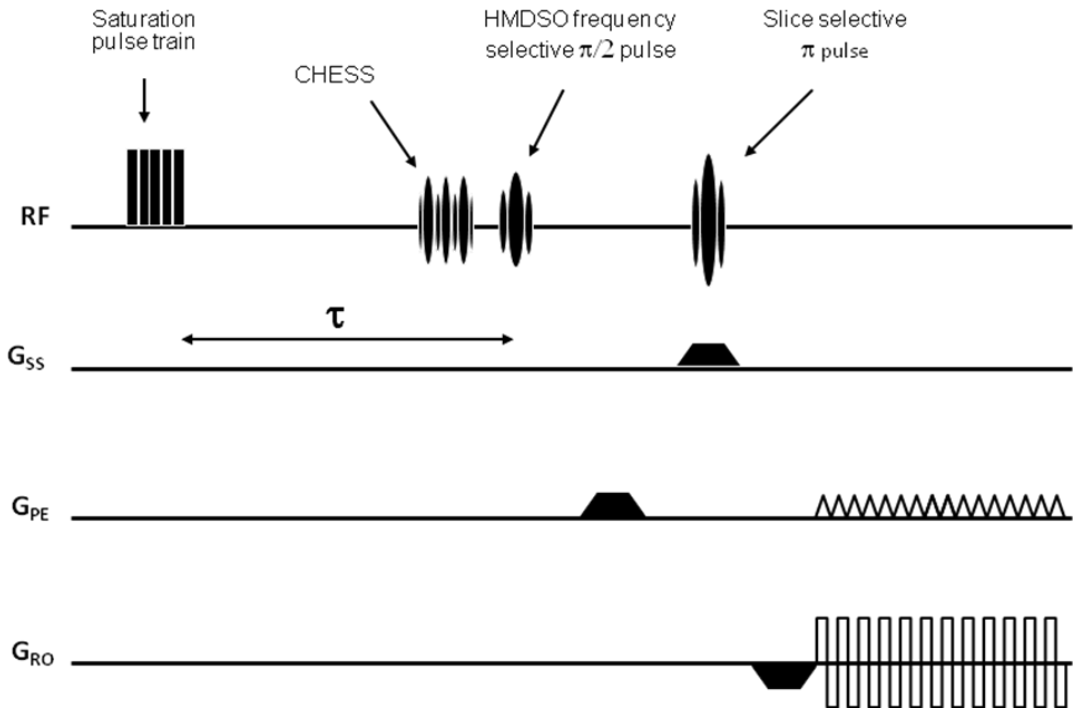

Figure 1.7 Pulse sequence for PISTOL

CHAPTER 2

INVESTIGATING THE POTENTIAL OF NOVEL SILOXANE BASED ^{1}H MR PO_2 REPORTER PROBES

2.1 Abstract

Quantitative *in vivo* oximetry has been reported using ^{19}F MRI in conjunction with reporter molecules for tissue oxygenation (pO_2) such as perfluorocarbons. Recently, hexamethyldisiloxane (HMDSO) was proposed as a promising alternative reporter molecule for ^{1}H MRI-based measurement of pO_2. In this study, I investigated various linear and cyclic siloxanes of different chain lengths as pO_2 sensing reporter molecules. To aid biocompatibility for potential systemic administration, various nanoemulsion formulations were prepared using a wide range of HMDSO volume-fractions and HMDSO/surfactant ratios. Calibration curves (R_1 vs pO_2) for all the siloxanes and emulsion formulations were found to be linear. The calibration curves of emulsions were similar to neat HMDSO for low surfactant concentrations (<10% v/v). Small temperature dependence in the calibration curves was observed, similar to previous report on neat HMDSO. These were characterized to be ~1 torr/^{o}C for HMDSO emulsion and ~1.4 torr/^{o}C for octamethyltrisiloxane (OMTSO) under hypoxic conditions. To demonstrate application *in vivo*, 100 µl of nanoemulsion formulation consisting of 40% v/v HMDSO and 5% v/v HS-15, was administered into healthy rat thigh muscle. Dynamic changes in mean thigh tissue pO_2 were measured using the Proton Imaging of Siloxanes to map Tissue Oxygenation Levels (PISTOL) technique in response to hyperoxic gas breathing challenge. Changing the inhaled gas from air to normobaric oxygen (NBO) increased the mean thigh muscle pO_2 from 49.7 ± 10 torr to 178.5 ± 55 torr which then returned back to baseline pO_2 value of 55.8 ± 14 torr on air breathing. During hyperbaric oxygen (HBO) challenge the mean thigh muscle pO_2 increased to 437± 97 torr. 1-way ANOVA followed by Dunnett's multiple comparison test found

significant increase in pO_2 values during NBO and HBO interventions when compared to initial baseline pO_2 and no significant differences while animal breathed air in between interventions. These results demonstrate the feasibility of using various siloxanes and HMDSO nanoemulsions as probes of pO_2 and their utility to assess oxygen dynamics *in vivo*, further developing quantitative ^{1}H MRI oximetry.

2.2 Introduction

Oxygen delivery is crucial for the efficient functioning of most tissues. Hypoxia or low tissue oxygen tension (pO_2) has been shown to promote the malignant progression of cancer, induce genes promoting angiogenesis, and reduce the efficacy of various therapies (10,12). There is increasing evidence for tumor hypoxia as a powerful physiological stimulus that can be exploited as a tumor-specific condition, allowing for the design of hypoxia-activated anticancer drugs (13) or novel hypoxia-regulated gene therapy strategies (14). Therefore, accurate and repetitive evaluation of tissue oxygen content (pO_2) noninvasively in response to interventions at various stages of growth should provide a better understanding of tumor response to therapy, potentially allowing therapy to be tailored to individual characteristics. Many MR and non-MR based techniques have been developed to assess tumor oxygenation as reviewed recently (16,17). In particular, quantitative NMR oximetry based on exogenous pO_2 reporter molecules (35) has been shown to be an extremely useful, minimally invasive technique for tumor stratification based on response to hyperoxic gas breathing (17).

Our research group has previously shown that tumor pO_2 measurements using ^{19}F MRI of the reporter molecule hexafluorobenzene correlated well with response to radiotherapy in two Dunning prostate R3327 rat tumor types (37,44). However ^{19}F MRI remains somewhat esoteric for clinical applications and we have recently identified hexamethyldisiloxane (HMDSO) as a analogous ^{1}H MR probe of pO_2 and shown the feasibility of tissue oximetry using ^{1}H MR spectroscopic relaxometry (42). We also implemented an imaging based method: Proton

Imaging of Siloxanes to map Tissue Oxygenation Levels (PISTOL) for spatial mapping of pO_2 (43). PISTOL uses an echo planar imaging sequence, which provides pO_2 measurements with a temporal resolution of 3.5 min and spatial resolution of ~1.5-4 mm^3. The technique has many virtues for investigating solid tumors in animals: 1) high sensitivity to changes in pO_2 and minimal sensitivity to temperature, 2) ability to provide pO_2 maps enabling the assessment of pO_2 at multiple locations simultaneously, thereby revealing both baseline heterogeneity and differential response to intervention and 3) potential for translation, since it is a ^1H MR technique.

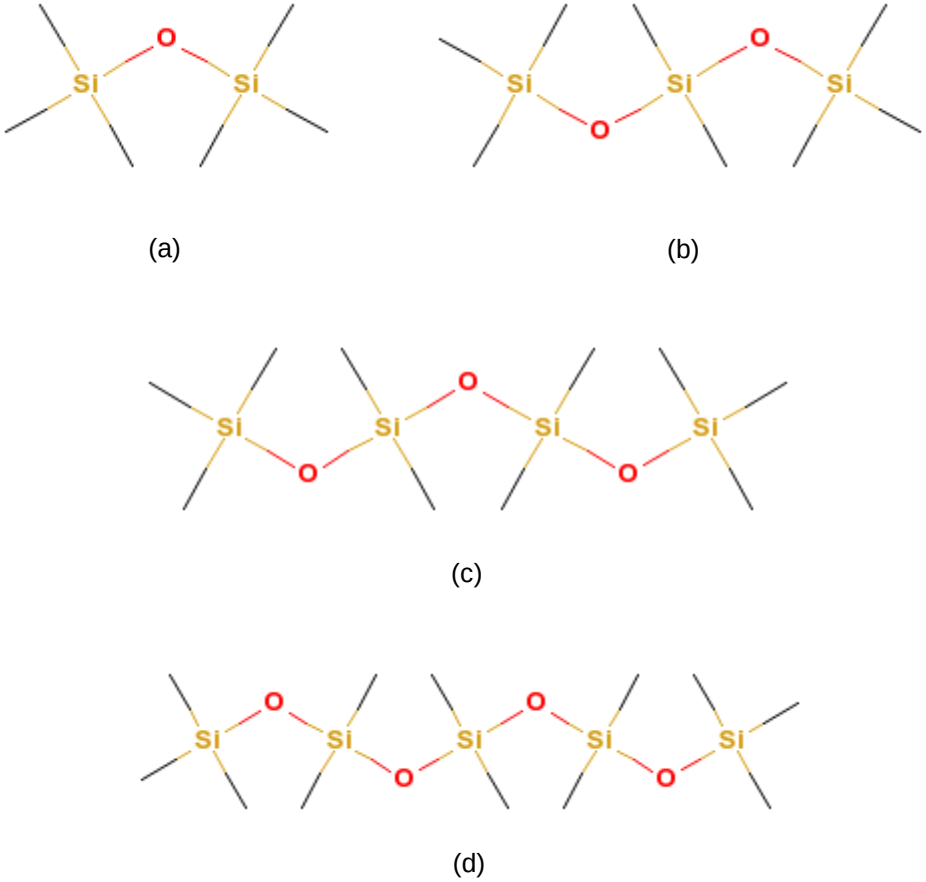

Figure 2.1 Structures of the various linear siloxanes characterized in this study.
a) Hexamethyldisiloxane (HMDSO), b) Octamethyltrisiloxane (OMTSO),
c) Decamethyltetrasiloxane (DMTSO), d) Dodecamethylpentasiloxane (DDMPSO),

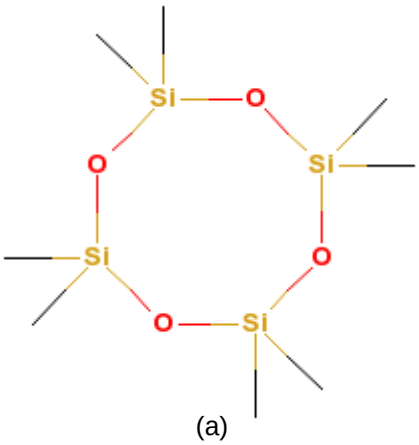

(a)

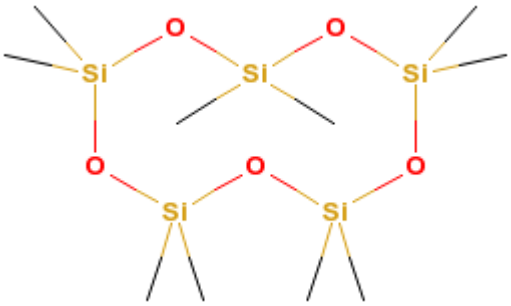

(b)

Figure 2.2 Structures of the cyclic siloxanes characterized in this study.
a) Octamethylcyclotetrasiloxane (OMCTSO) and b) Decamethylcyclopentasiloxane (DMCPSO).

Sub-micron and nanoemulsions have long been established as drug delivery systems for either lipophilic or hydrophobic substances. The main reasons for using emulsions include solubilization of poorly water-soluble drugs and imaging probes, reduction of toxicity and possibly targeted delivery to various organs (45). HMDSO is lipophilic and immiscible in aqueous solutions which could preclude systemic delivery and/or functional modifications for targeting unless emulsified. The main aim of this study is the preparation and characterization of HMDSO nanoemulsions for use *in vivo*. Vitamin E d-alpha tocopheryl polyethylene glycol 1000

succinate (VE-TPGS) is a biocompatible, water-soluble derivative of natural vitamin E which has been used for reversing vitamin E deficiency (46) as well as a drug solubilizer (47), absorption enhancer (48) and as a vehicle for lipid-based drug delivery formulations (49). VE-TPGS was also reported to enhance the cytotoxicity of anticancer drugs doxorubicin, vinblastine, and paclitaxel (50). Solutol® HS 15 (henceforth, referred to as HS-15) consists primarily of polyglycol mono-ester of 12-hydroxystearic acid and free polyethylene glycol (PEG) and has also been used as a drug solubilizer (47,51), as well as for delivery of lipophilic drugs (52). In the past, perfluorocarbon based emulsions have been developed as artificial blood substitutes, ultrasound contrast agents, cellular and molecular imaging agents and have also been used for ^{19}F MR oximetry (27,53,54). I now demonstrate the synthesis and characterization of HMDSO based nanoemulsions for ^{1}H oximetry based on VE-TPGS and HS-15. I also present an *in vivo* feasibility study showing dynamic changes in rat thigh tissue oxygenation in response to hyperoxic gas breathing following an intramuscular injection of nanoemulsion. Further I also demonstrate the utility of various linear (Fig 2.1) and cyclic siloxanes (Fig 2.2) as ^{1}H MR pO_2 reporter probes.

2.3 Materials and Methods

2.3.1 Materials

The linear and cyclic siloxanes: HMDSO, OMTSO, DMTSO, DDMPSO, OMCTSO and DMCPSO were purchased from Sigma Aldrich (St Louis, MO). HMDSO was used as oil phase in the preparation of nanoemulsions. HS-15 was a gift from BASF Corporation (Ludwigshafen, Germany) and consists of polyglycol esters of 12-hydroxystearic acid and free polyethylene glycols. VE-TPGS was purchased from Eastman Chemical Company (Kingsport, TN). HS-15 or VE-TPGS were used as non-ionic surfactants to solubilize HMDSO. All the materials were used as received.

2.3.2 Preparation of nanoemulsions

Nanoemulsions were prepared by addition of de-ionized water to the mixture of HMDSO and surfactant (Solutol HS 15 or VE-TPGS) and sonication for 15 min, at 150 W output power and 50% duty cycle, using an Omniruptor 4000 Ultrasonic Homogenizer (Omni International, Kennesaw, GA). Emulsions were prepared using various volume fractions of surfactant (HS-15 or VE-TPGS) and HMDSO in order to determine the optimal combination to achieve the required particle size and sensitivity to oxygen, while maintaining high HMDSO payload. Nine different nanoemulsion formulations were prepared and evaluated: a) 40% v/v HMDSO: 20% v/v HS-15, b) 40% v/v HMDSO: 10% v/v HS-15, c) 40% v/v HMDSO: 5% v/v HS-15, d) 30% v/v HMDSO: 30% v/v HS-15, e) 20% v/v HMDSO: 30% v/v HS-15, f) 40% v/v HMDSO: 10% v/v VE-TPGS, g) 40% v/v HMDSO: 7% v/v VE-TPGS, h) 40% v/v HMDSO: 5%v/v VE-TPGS, i) 30% v/v HMDSO: 5% v/v VE-TPGS.

Nanoemulsions were prepared by addition of de-ionized water to the mixture of HMDSO and surfactant (Solutol HS-15 or VE-TPGS) and sonication for 15 min (Fig 2.3), at 150 W output power and 50% duty cycle, using an Omniruptor 4000 Ultrasonic Homogenizer (Omni International, Kennesaw, GA). Emulsions were prepared using various volume fractions of surfactant (HS-15 or VE-TPGS) and HMDSO in order to determine the optimal combination to achieve the required particle size and sensitivity to oxygen, while maintaining high HMDSO payload.

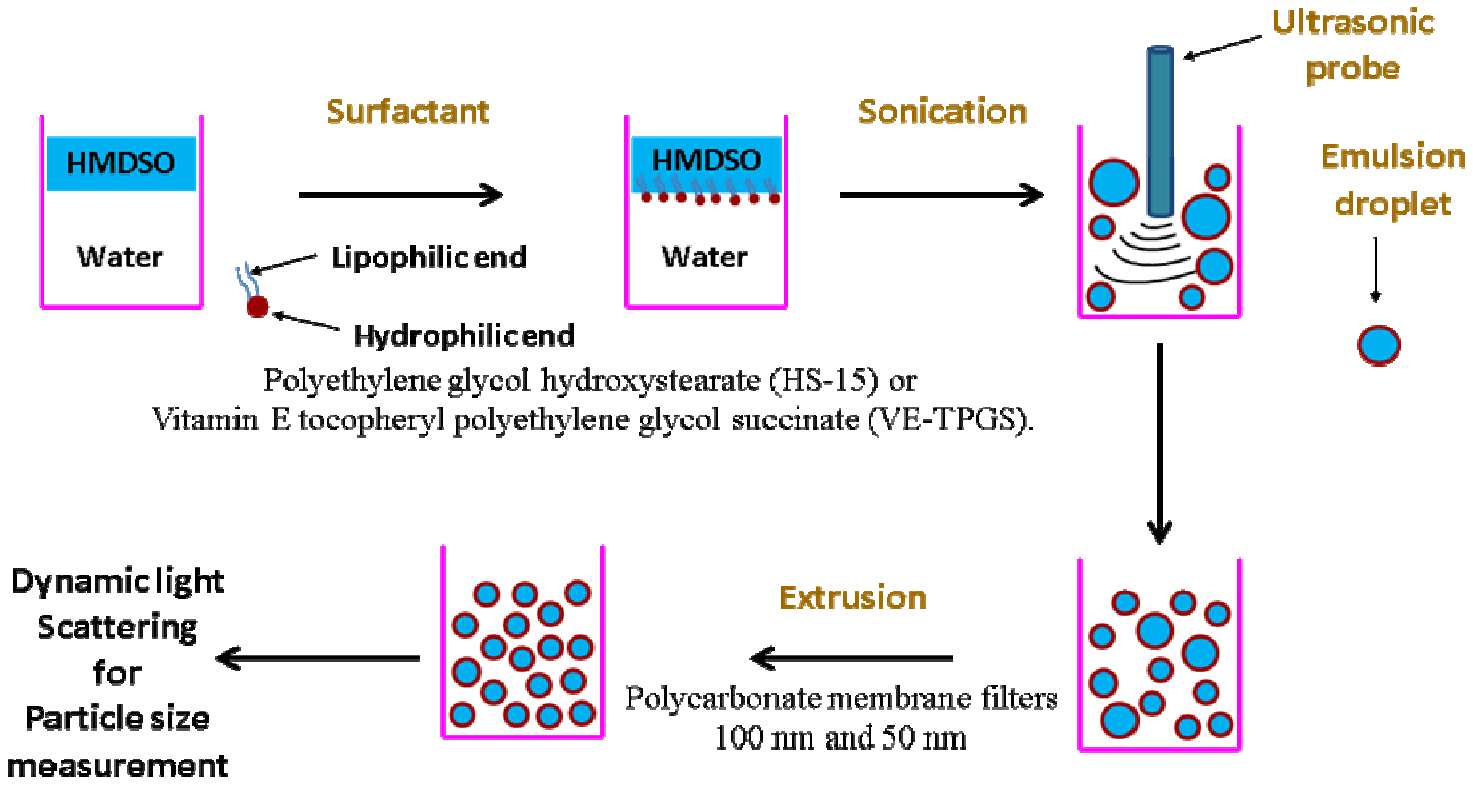

Figure 2.3 Schematic of the nanoemulsion preparation procedure. The nanoemulsions were prepared by ultrasonication followed by extrusion through polycarbonate filters.

Nine different nanoemulsion formulations were prepared and evaluated: a) 40% v/v HMDSO: 20% v/v HS-15, b) 40% v/v HMDSO: 10% v/v HS-15, c) 40% v/v HMDSO: 5% v/v HS-15, d) 30% v/v HMDSO: 30% v/v HS-15, e) 20% v/v HMDSO: 30% v/v HS-15, f) 40% v/v HMDSO: 10% v/v VE-TPGS, g) 40% v/v HMDSO: 7% v/v VE-TPGS, h) 40% v/v HMDSO: 5% v/v VE-TPGS, i) 30% v/v HMDSO: 5% v/v VE-TPGS. To achieve further reduction in particle size, the emulsions were passed through a LiposoFast® extrusion filter (Avestin Inc., Ottawa, Canada) with a polycarbonate membrane filter of 100 and 50 nm pore size, sequentially. For each pore size, the extrusion was repeated 11 times (55). For studying the effect of extrusion filtering, samples were drawn at each stage: before filtration, after extrusion through 100 nm filter and after extrusion through 50 nm filter. Particle size measurements were performed immediately following the extrusion step using a Wyatt Technologies DynaPro Titan (Wyatt Technology Corporation, Santa Barbara, CA) dynamic light-scattering instrument.

2.3.3 In vitro calibration of R_1 dependence of pO_2

MRI studies were performed on a Varian 4.7T MRI scanner. Each of the siloxanes and nanoemulsion formulations were put into four gas-tight NMR glass tubes (Wilmad-Labglass, Buena, NJ) and saturated by bubbling for 15 min with varying standard gases including 0%, 5%, 10% and 21%O_2 (balance N_2), respectively. Each sealed tube was wrapped in a D_2O filled circulating water pad maintained at a desired temperature and fit under a 1 cm surface coil. A spin-echo-based pulse sequence, consisting of initial pulse-burst saturation recovery preparation pulses combined with frequency-selective excitation of HMDSO and suppression of water signal, was used to measure T_1 values, as described previously (42). For measurement of temperature dependence of T_1, the temperature of the water pad was varied between 22 to 52 ^{o}C. The temperature was measured using a fiber optic probe (FISO Technologies Inc., Quebec, Canada). T_1 measurements were performed after the tube temperature was allowed to equilibrate at the desired value for 10 min. The data at each temperature were then fit to a

model: $R_1[s^{-1}]$ (=$1/T_1$) = A'+ B'* pO_2, where A' and B' are temperature dependent constants. A' and B' were then fit to the model A' =A+C*T and B'=B+D*T to determine the constants A, B, C, D that characterize the pO_2 and temperature dependence of R_1, as reported previously for neat HMDSO (42). Fully relaxed (TR= 30 s) ^{1}H NMR spectra were acquired for a 1:1 mixture of HMDSO and deionized H_2O as well as for unfiltered and filtered nanoemulsion samples (40% v/v HMDSO: 5% v/v HS-15, rest deionized H_2O).

2.3.4 Cytotoxicity assay

2.3.4.1 Cells

NIH 3T3 fibroblast cells were cultured in Dulbecco's Modified Eagle's Medium containing 10% fetal bovine serum (Atlanta Biologicals, Lawrenceville, GA) and 1% antibiotic solution (100U/ mL penicillin, 100mg/mL streptomycin, Atlanta Biologicals) at 37 ℃ under 5% CO_2 in a humidified incubator.

2.3.4.2 Determination of the standard curve

Cells were seeded in a 24-well plate with seeding densities of 1k, 10k, 50k, 100k and 500k cells in 1 mL medium (Fig 2.4 a). Cell seeding was done in triplicate and incubated for 24 hours to promote cell attachment. For quantifying the cell numbers, published crystal violet staining protocols was used (56).

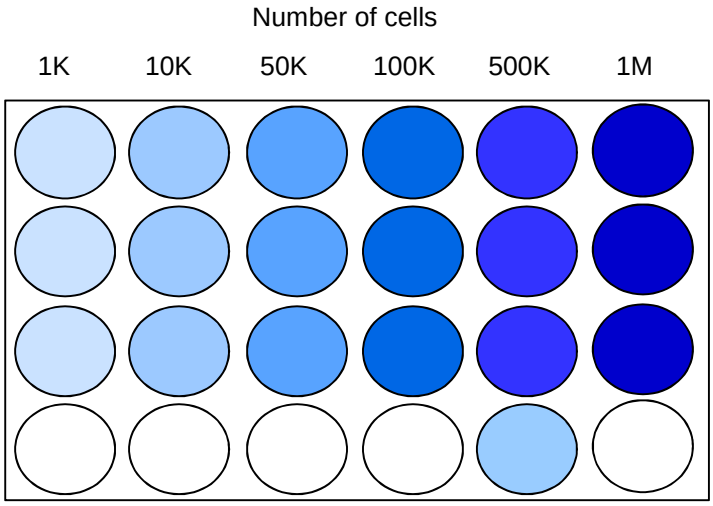

(a)

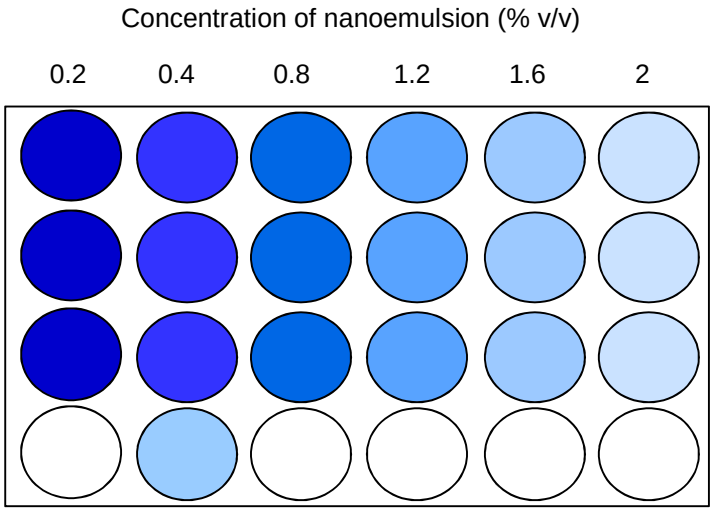

(b)

Figure 2.4 Schematic diagrams of 24 well plates for determination of the (a) standard curve and (b) cytotoxicity. (a) In the standard curve experiment, each well contained 1 mL of medium with varying numbers of cells. No nanoemulsions were added. (b) For the cytotoxicity experiment. Each well contained 0.25 million cells in 1 mL media, but with varying concentrations of nanoemulsions.

2.3.4.3 Cytotoxicity Assay

Cells were seeded in 24- well plates at a seeding density of $2.5X10^5$ cells in 1mL medium and all the experiments were done in triplicate (Fig 2.3 b). Cells were allowed to attach for 24 h following which cytotoxicity experiments were performed by adding varying concentrations of either nanoemulsion (40% v/v HMDSO-5% v/v HS-15) or HS-15 surfactant alone (5% v/v) to the medium. The concentrations used were 0, 0.2, 0.4, 0.8, 1.2, 1.6, and 2 %v/v of medium. The plates were incubated for 4 hours and a standard crystal violet staining protocol (56) was used to determine the viable fraction of cells in each well.

2.3.4.4 Crystal violet staining protocol

Culture medium was discarded and plates were rinsed with PBS. Cells were then fixed by adding 500 µL of 10% formalin to each well and were kept at 4 ºC for 10 minutes. The fixative solution was then discarded, rinsed with PBS and the plates were allowed to air dry for 5 minutes. Cells were then stained by adding 500 µL/well of 0.1% crystal violet (CV) solution for 30 minutes at room temperature under gentle shaking. Excess stain was removed by rinsing with PBS followed by DI-H_2O and then the plates were allowed to air dry for 5 minutes. The bound stain was dissolved in 200 µL of 10% acetic acid per well. 10 µL of the CV solution from each well was then diluted 100 times and three samples of each solution were loaded in a 96-well plate. The optical density (OD) of each well at 560 nm was measured using a plate reader.

2.3.5 In vivo MR Imaging

2.3.5.1 Normobaric oxygen (NBO) breathing protocol

MR oximetry studies were performed on six Fisher 344 rats (Charles River Laboratories, Wilmington, MA). Three more Fisher rats were used to measure clearance by imaging. All the animal experiments were approved by the Institutional Animal Care and Use Committee. The rats were sedated using gaseous anesthesia (1 L/min air & 1.5 % isoflurane).

For the pO_2 measurements, 100 µL of freshly prepared nanoemulsion (40% v/v HMDSO-5% v/v HS-15) was injected into the thigh, using a syringe with 32-gauge needle and distributed in a fan pattern across a plane as described in (17). This was done to ensure sampling of different regions of the thigh that might have different response to oxygenation. The thigh of the rat was then placed in a single turn 2 cm solenoid volume coil. A warm circulating water blanket was used to maintain the body temperature at 37 ℃. Quantitative MR oximetry was then performed using the protocol described previously (43).

Briefly, following anatomical scout scans using a spin echo sequence, the distribution of nanoemulsion in the thigh was visualized using a chemical shift selective spin echo sequence (on-resonance for HMDSO). To modulate oxygenation, the rats were subjected to breathing gas challenge. The protocol used 20 min air inhalation (baseline) followed by 30 min oxygen breathing and return to air inhalation for 30 min. Using the previously developed PISTOL technique (43), T_1 datasets were recorded (recovery time τ = 55, 0.1, 40, 0.2, 20, 0.4, 12.5, 0.8, 8, 1, 6, 1.5, 5, 2, 4, 3 s with number of averages = 1, 8, 1, 8, 1, 8, 1, 4, 1, 4, 1, 2, 1, 1, 1, 1, respectively, T_{acq} = 3 ½ mins) every 5 minutes during these 80 min and T_1 maps were generated from these data. Using the calibration equation for nanoemulsion formulation determined *in vitro*, pO_2 maps were computed on a voxel-by-voxel basis from the T_1 maps. Only the common voxels from the 16 pO_2 maps were considered for further analysis and voxels were rejected if T_1 error (ΔT_1) >1 s, or ratio $\Delta T_1/T_1$ > 10%. These stringent error criteria were used to retain only the data of high quality and precision and to exclude artifacts. The pO_2 data are presented as mean pO_2 ± standard deviation.

2.3.5.2. Hyperbaric oxygen (HBO) breathing protocol

MR oximetry studies were performed on six Athymic nude rats (Charles River Laboratories, Wilmington, MA). The rats were sedated using gaseous anesthesia (1 L/min air & 1.5 % isoflurane). For the pO_2 measurements, 100 µL of freshly prepared nanoemulsion (40% v/v HMDSO-5% v/v HS-15) was injected into the thigh, using a syringe with 32-gauge needle and distributed in a fan pattern across a plane as described in (17). This was done to ensure sampling of different regions of the thigh that might have different response to oxygenation. The thigh of the rat was then placed in a single turn 3 cm solenoid volume coil built into the MR compatible hyperbaric chamber (Fig 2.5). Warm circulating water passing through the animal bed helped maintain the body temperature at 37 ℃. Quantitative MR oximetry was then performed using PISTOL technique described previously (43). T_1 datasets (subsequently pO_2 maps) were obtained using this sequence at 5 min intervals. In order to modulate tissue oxygenation, the rats were subjected to respiratory challenge in the sequence: air (20 min) – normobaric oxygen (60 min) – air (30 min) – hyperbaric oxygen (60 min)-air (30min).

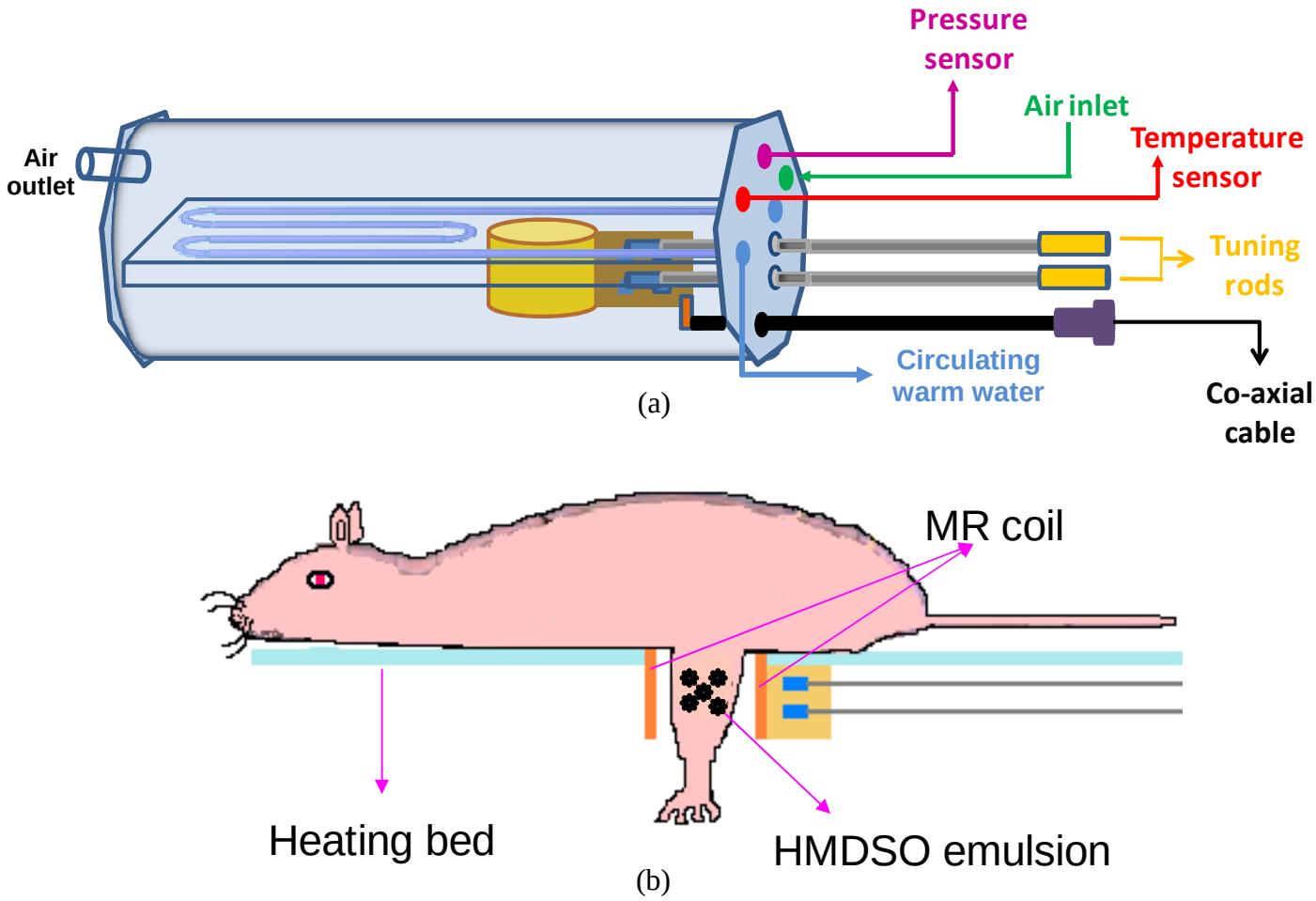

Figure 2.5 a) Schematic of the MR compatible hyperbaric chamber. The end plate was designed with ports for temperature and pressure sensors, air inlet etc. b) Schematic of an animal positioned on the animal bed with the leg going through the RF coil.

2.4 Results

2.4.1. In vitro NMR calibration

2.4.1.1 HMDSO based nanoemulsions

Nanoemulsions were prepared using a range of HMDSO volume fractions and HMDSO/surfactant ratios. The particle sizes for 7 out of 9 emulsion formulations were less than 150 nm as determined by dynamic light scattering (Table 2.1). In general, lower surfactant concentrations yielded smaller particle sizes for a 40% HMDSO payload. While long-term shelf stability was not studied, no creaming or separation was observed for up to two hours. In the case of 40% v/v HMDSO & 5% v/v VE-TPGS nanoemulsion filtering through the 100 nm polycarbonate filter followed by the 50 nm filter significantly reduced the median particle radius from 359 nm to 84 nm (Fig. 2.6a), while for the 40% v/v HMDSO & 5% v/v HS-15 the change was from to 172 nm to 113 nm (Fig. 2.6b).

Table 2.1 Physical characterization of HMDSO nanoemulsions. Values of calibration constants A', B' and particle sizes of various nanoemulsion formulations are compared with neat HMDSO. The calibration constants were similar to that of neat HMDSO when the volume fraction of surfactant (either HS-15 or VE-TPGS) is less than 10%.

	HMDSO % vol	Emulsifier % vol	A' s^{-1}	B' $(torr\ s)^{-1}$	η ($X10^{-3}$) =B'/A'	Mean R nm
HS-15 NE	20	30	0.1808	0.00131	7.2	136
	30	30	0.1508	0.00127	8.4	129
	40	20	0.1227	0.00135	11.0	266
	40	10	0.1143	0.00134	11.7	96
	40	5	0.1103	0.00143	13.0	79
VE-TPGS NE	30	5	0.1232	0.00134	10.9	131
	40	7	0.1112	0.00143	12.9	230
	40	5	0.1137	0.00139	12.2	182
	40	2	0.1103	0.00145	13.2	92
HMDSO	100	0	0.1126	0.00130	11.6	NA

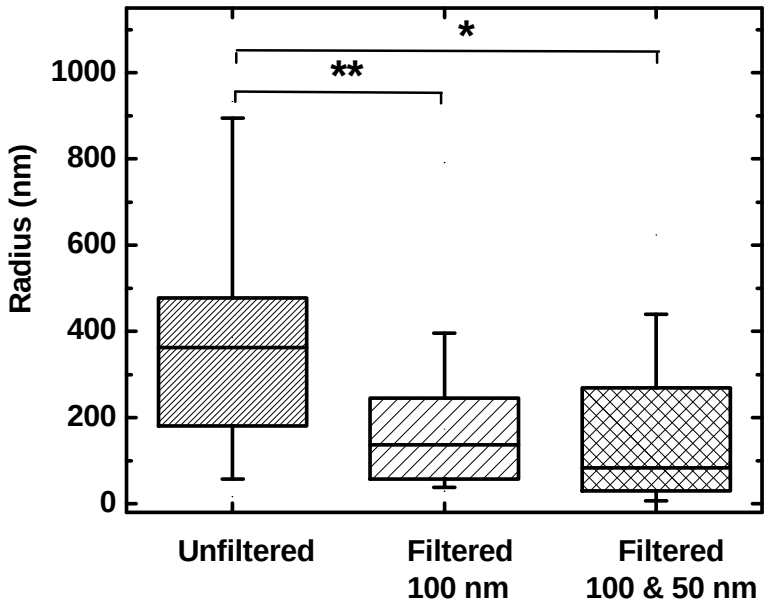

(a)

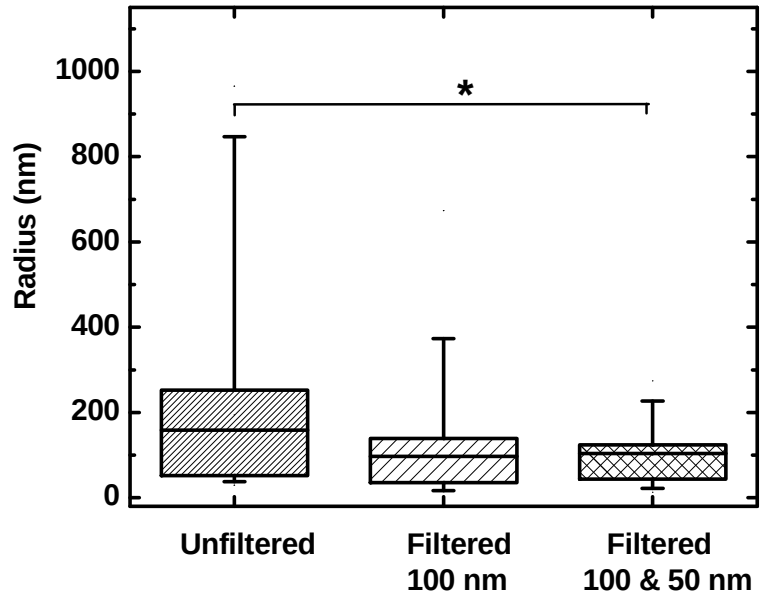

(b)

Figure 2.6 Effect of filtration on nanoemulsion size. Box plot of the particle sizes measured from unfiltered nanoemulsion samples, samples filtered using a 100 nm polycarbonate filter and samples filtered using both 100 nm and 50 nm polycarbonate filters for (a) 40% v/v HMDSO- 5% v/v VE-TPGS and (b) 40% v/v HMDSO- 5% v/v HS-15 nanoemulsions. Median is shown as solid line, with box representing 25^{th} to 75^{th} percentile and the whiskers end at 5^{th} and 95^{th} percentiles. Data are compared between the groups using Student's t-test. $p < 0.05$.

The ratios of the water proton to HMDSO proton signals (area under peak from fully relaxed spectra) for unfiltered and filtered nanoemulsions (40% v/v HMDSO: 5% v/v HS-15, rest deionized H_2O) were 1:0.525 and 1:0.533, respectively, compared to the theoretically expected ratio 1:0.555. The linewidths for the water and HMDSO peaks were both 0.2 ppm for a 1:1 mixture of water and HMDSO while those for the nanoemulsion were 0.5 and and 0.8 ppm, respectively. At a fixed temperature (37 ℃), the R_1 of all the nanoemulsion formulations showed a linear dependence on pO_2 (R^2>0.99). The values of the intercept A' and slope B' for all the nanoemulsion formulations are tabulated in Table 2.1.

The calibration curves for all nanoemulsion formulations are shown in Figure 2.6. Also shown for comparison, is the published calibration curve (42) for neat HMDSO (Fig 2.6 a&b, dotted line). In the nanoemulsion sample containing 20% v/v HMDSO & 30% v/v HS-15 as surfactant, the T_1 at 37 ℃ ranged from 5.46 s (pO_2 = 0 torr) to 2.55 s (pO_2 = 160 torr). But for the nanoemulsion sample containing 40% v/v HMDSO & 5% v/v HS-15, the T_1 at 37 ℃ ranged from 8.68 s (pO_2 = 0 torr) to 2.94 s (pO_2 = 160 torr). In the nanoemulsions with HS-15 as surfactant, increasing HMDSO volume fraction caused the T_1 of the nanoemulsions to become longer (at the same pO_2), but the slopes of the linear fits remained similar (Fig 2.7a, Table 2.1). The nanoemulsion containing VE-TPGS as surfactant, showed a smaller increase (8.13 s to 8.54 s) in T_1 with increasing HMDSO volume fraction (Fig 2.7b). Calibration curves were found to be similar to that of neat HMDSO when the volume fraction of surfactant (either HS-15 or VE-TPGS) was less than 10% (Table 2.1). Based on the calibration curve and particle size, the 40% v/v HMDSO & 5% v/v HS-15 nanoemulsion was chosen for further work and the temperature sensitivity of its calibration curve was determined. Both constants A' (Fig. 2.8a) and B' (Fig. 2.8b) showed a linear dependence on temperature T (R^2= 0.996 and 0.965, respectively). Fitting the R_1 data to the four parameter model described earlier yielded A = 0.1636 ± 0.0022 s^{-1}, B = (1.53 ± 0.02) X 10^{-3} (s torr)$^{-1}$, C = (-12.10 ± 0.62) X 10^{-4} (s ℃)$^{-1}$, and D = (-0.72 ± 0.07) X10^{-5} (s torr ℃)$^{-1}$.

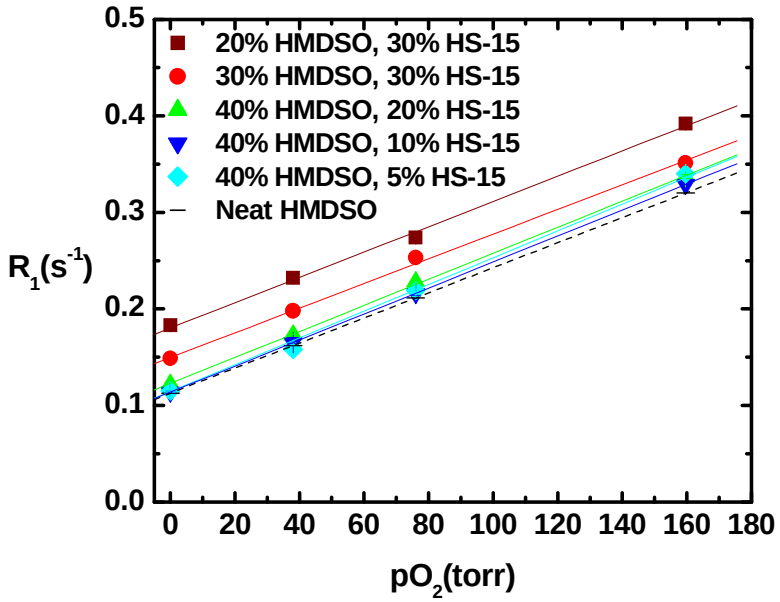

(a)

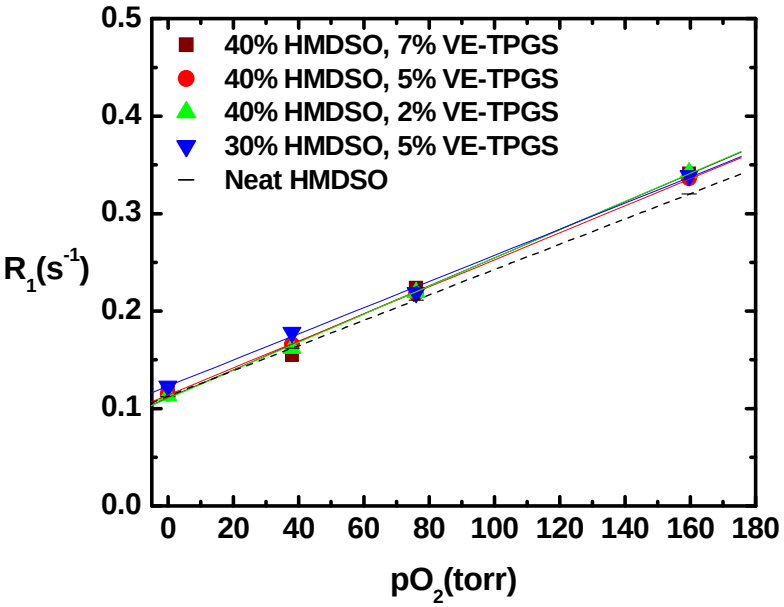

(b)

Figure 2.7 R_1 dependence of HMDSO based nanoemulsions on pO_2. (a) Calibration curves for emulsions with different HMDSO/ HS-15 volume fractions. (b) Calibration curves for emulsions with different HMDSO/ VETPGS volume fractions.

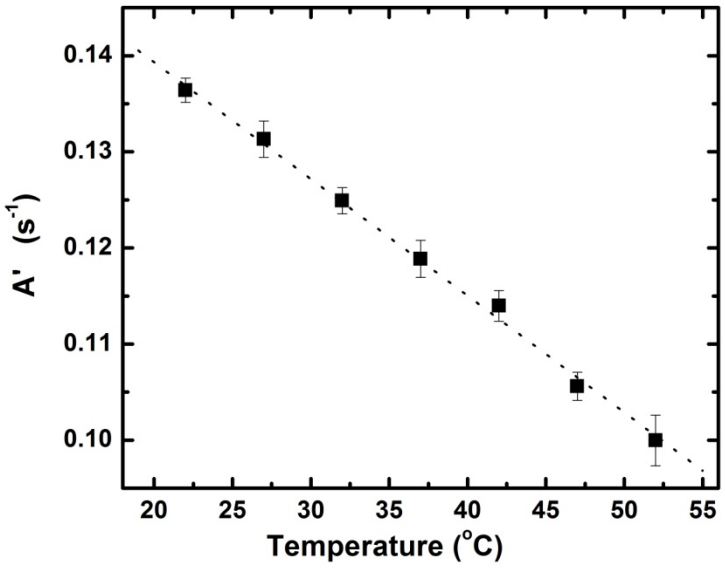

(a)

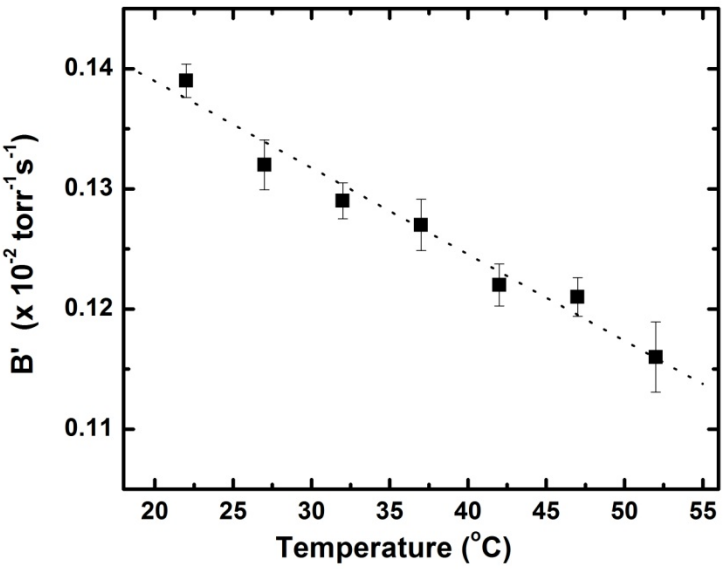

(b)

Figure 2.8 Temperature dependence of the pO_2 calibration curve for HMDSO nanoemulsion. Plotting graphs of (a) A' (intercept of R_1 vs pO_2 at fixed temperature T) and (b) B' (slope of R_1 vs pO_2 at fixed T) as a function of T, shows linear dependence in the range 22-52 ^{o}C. Linear fits to these data enable estimation of constants A, B, C and D in the equation

$R_1 = A + B*pO_2 + C*T + D*pO_2*T$

The IC_{50} (concentration at which half of the initial number of cells die) of 40% v/v HMDSO & 5% v/v HS-15 nanoemulsion towards 3T3 fibroblast cells was found to be 1% and that of 5% v/v HS-15 surfactant solution was 2% by volume demonstrating that these compounds were well tolerated (Fig 2.9). The plot shows the average number of viable cells with respect to concentration of added nanoemulsion or surfactant and the error bars represent the standard deviation of 9 multiplicates.

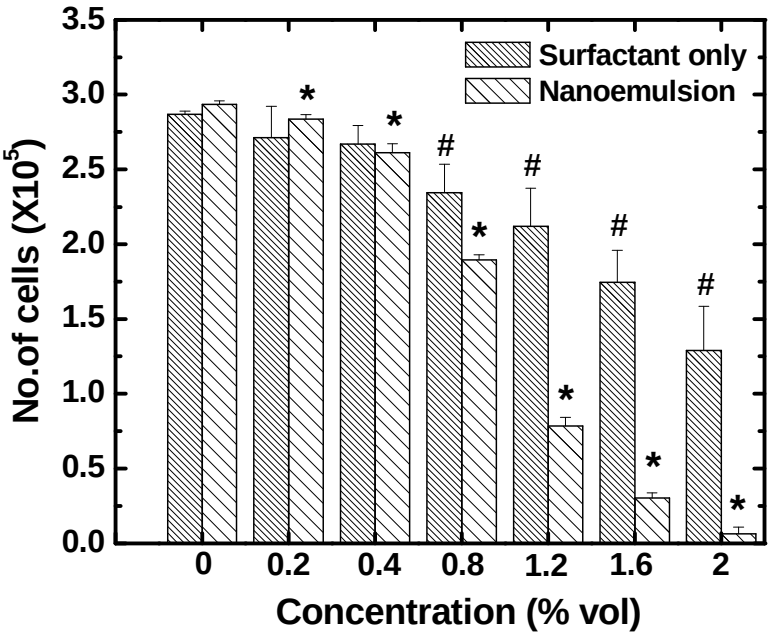

Figure 2.9 Cytotoxicity studies of HMDSO nanoemulsion. Cytotoxicty of 40% v/v HMDSO- 5% v/v HS-15 nanoemulsions and 5% v/v HS-15 solution towards 3T3 fibroblasts was determined by crystal violet assay. # and * represent statistically significant difference ($p<0.05$) for surfactant only and nanoemulsion data compared with the zero concentration column in each case.

2.4.1.2 Calibration curves of other linear and cyclic siloxanes

The linear siloxanes used in the study were hexamethyldisiloxane (HMDSO), octamethyltrisiloxane (OMTSO), decamethyltetrasiloxane (DMTSO) and dodecamethyl-pentasiloxane (DDMPSO) whereas the cyclic siloxanes used were octamethyl-

cyclotetrasiloxane (OMCTSO) and decamethylcyclopentasiloxane (DMCPSO). R_1 vs pO_2 calibration curves were measured by using the same experimental procedure used for HMDSO nanoemulsion calibration. Since molecular oxygen is paramagnetic, it shortens the T_1 of the samples. At a fixed temperature (37℃), the R_1 of all the siloxanes showed a linear dependence on pO_2 (R^2>0.99) given by the equation: R_1 [s^{-1}] = A'+ B'* pO_2 (torr) where A' and B' are calibration constants (Table 2.2), which represent anoxic R_1 and sensitivity of R_1 to pO_2 respectively. In the linear siloxanes it is observed that with increasing chain length, the R_1 of the samples became longer, but the slopes of the linear fits were almost similar (Fig. 2.10). The cyclic compounds had higher longitudinal relaxation rates than the linear compounds at all oxygen concentrations.

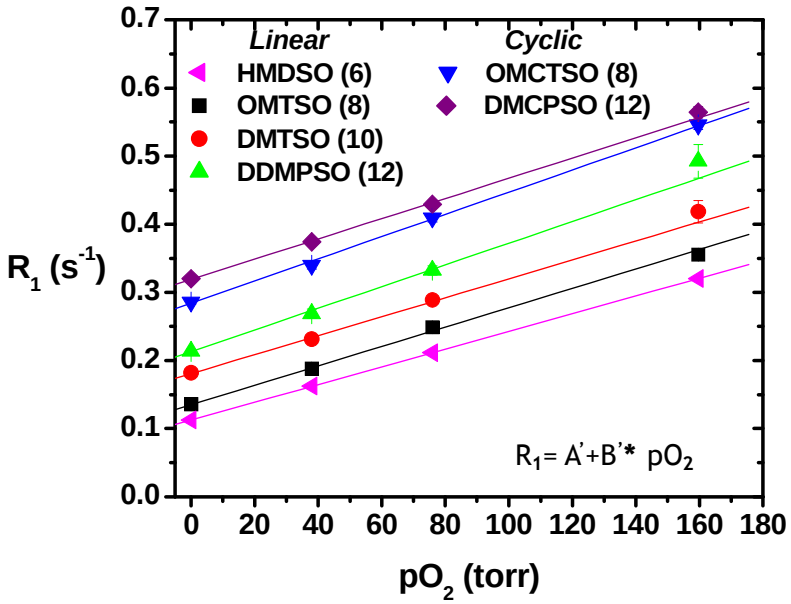

Figure 2.10 R_1 vs pO_2 calibration curves of linear and cyclic siloxanes of different chain lengths at 37 ℃. The cyclic compounds had higher longitudi nal relaxation rates than the linear compounds at all oxygen concentrations.

Table 2.2 Summary of calibration constants and boiling points of the various linear and cyclic siloxanes used along with fluorine MR oximetry probes

Compound	Intercept A' (s^{-1})	Slope B' ($s*torr^{)-1}$	η ($X10^{-3}$) =B'/A'	BP (°C)	Relative Signal
HMDSO	0.1126	0.0013	11.5	101	1.00
OMTSO	0.1352	0.0014	10.4	153	0.98
DMTSO	0.1808	0.0014	7.7	194	0.97
DDMPSO	0.2129	0.0016	7.5	230	0.97
OMCTSO	0.2842	0.0016	5.6	176	0.91
DMCPSO	0.3192	0.0015	4.7	90	0.91
HFB (17)	0.0835	0.0019	22.8	81	1.00
Perfluoro-15-Crown-5-ether (17)	0.375	0.0020	5.3	143	NA

Further I characterized the relaxation behavior of the evaluated linear and cyclic siloxanes by observing the magnetization recovery curves after bubbling with 0% O_2 and 21% O_2. Bi-exponential T_1 behavior was not observed in any of the agents suggesting that the availability of oxygen to all the protons (end chain vs backbone) of the long chains was unhindered (Fig 2.11 a & b, Fig 2.12 a & b).

OMTSO was further evaluated to determine the temperature dependence of its calibration curve at 4.7T (Fig 2.13b). The fit to the empirical model yielded the calibration constants A= 0.2295 ± 0.0021 s^{-1}, B=0.002 ± $4.1x10^{-5}$ $(s*Torr)^{-1}$, C=-0.002 ± $6.32x10^{-6}$ $(s*℃)^{-1}$, and D= $-2.09x10^{-5}$ ± $1.2x10^{-6}$ $(s*Torr*℃)^{-1}$ error in pO_2 determination for 1℃ change in temperature was therefore calculated to be ~ 1.41 Torr/℃ for a pO_2 of 5 Torr.

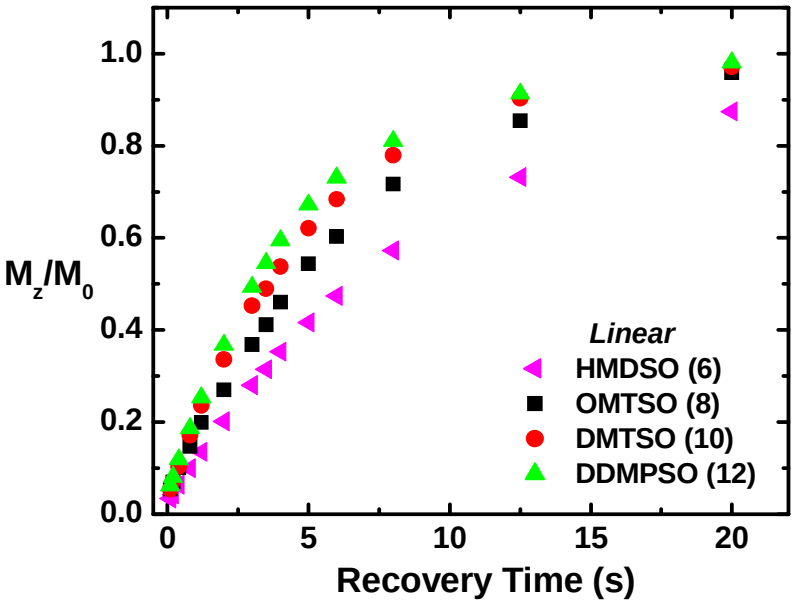

(a)

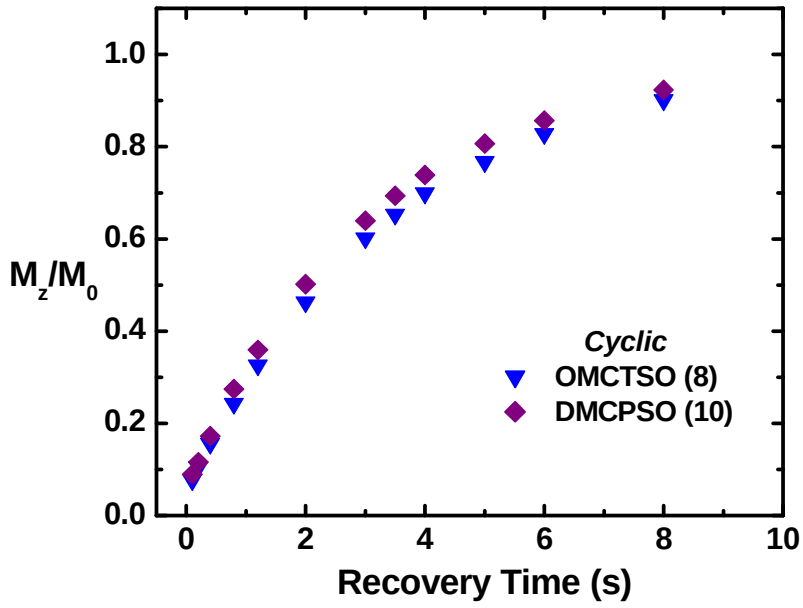

(b)

Figure 2.11 Magnetization recovery curves of the (a) linear and (b) cyclic siloxanes after bubbling with 0% O_2. These recovery curves didn't show a bi-exponential behavior even for linear long chain siloxanes.

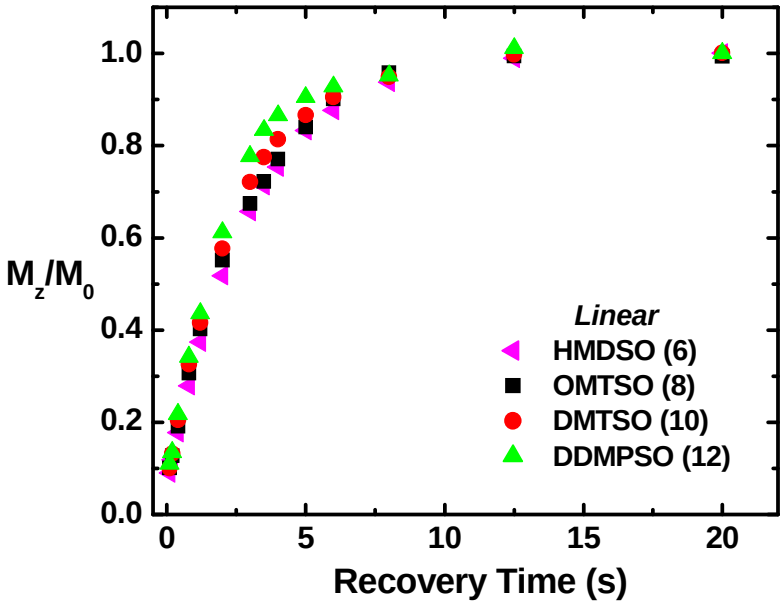

(a)

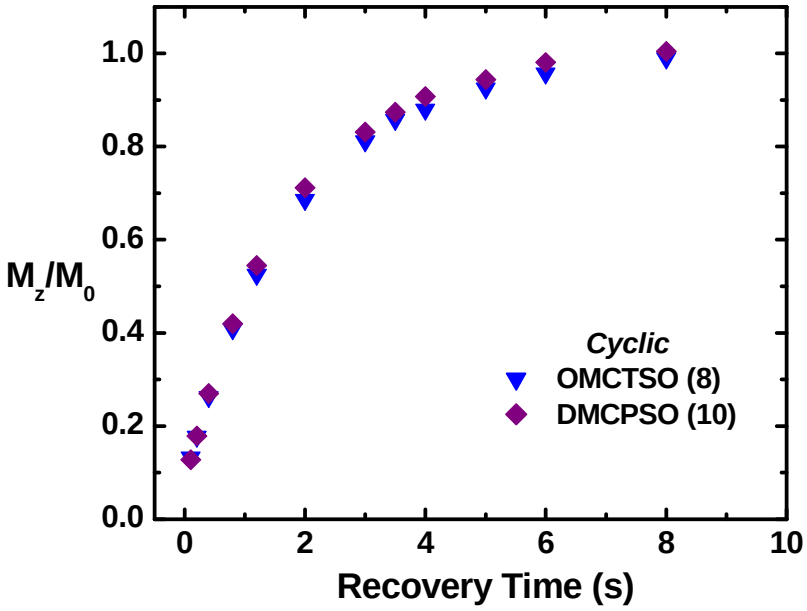

(b)

Figure 2.12 Magnetization recovery curves of the (a) linear and (b) cyclic siloxanes after bubbling with 21% O_2. These recovery curves didn't show a bi-exponential behavior even for linear long chain siloxanes.

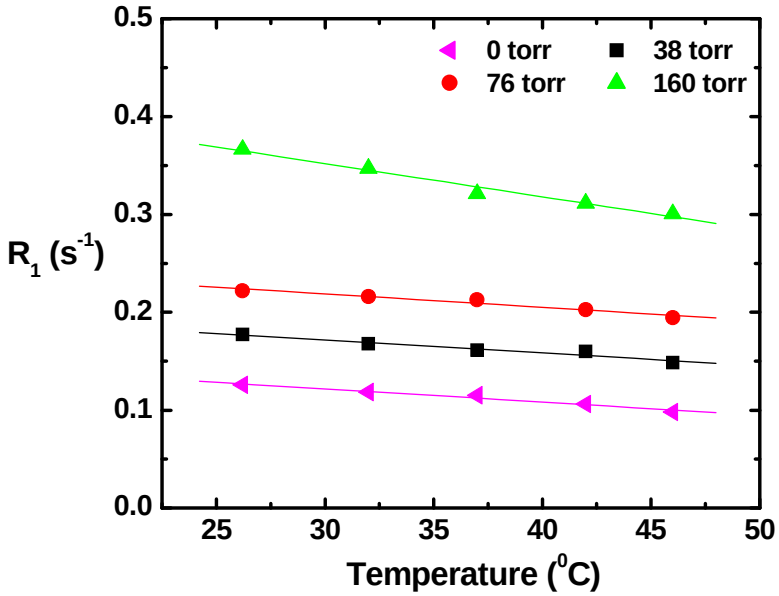

(a)

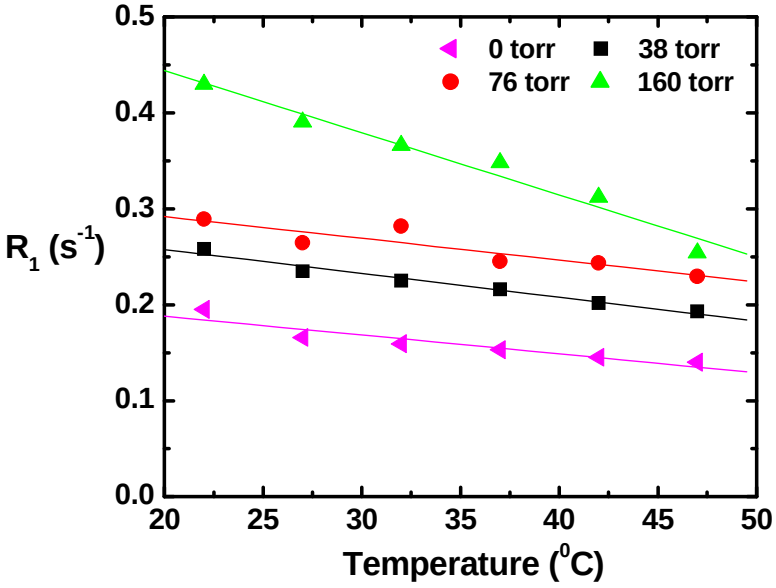

(b)

Figure 2.13 Comparison of the temperature dependence of R_1 of a) HMDSO and b) OMTSO at different pO_2 values.

2.4.2 In vivo tissue oximetry

2.4.2.1 Normobaric oxygen breathing intervention

Baseline pO_2 values were obtained by averaging four baseline pO_2 measurements while the rats breathed air. Figure 2.14 shows the pO_2 time course in rat thigh muscle in a representative animal overlaid on the scout image. In the cohort (n=6), mean baseline pO_2 measurements ranged from 24-53 torr (mean pO_2= 39 ± 7 torr), but remained stable in any given muscle with a mean fluctuation of ±5 torr over a period of 20 minutes (Fig. 2.15a). When the inhaled gas was switched to oxygen, pO_2 increased significantly ($p<0.01$) compared to baseline and continued to increase monotonically over the next 30 mins in 5 of the six animals. For the sixth animal, the maximum pO_2 value was observed at 25 min. The pO_2 measurements at the end of 30 minutes breathing oxygen ranged from 254 to 330 torr (mean pO_2 = 275 ± 27 torr). Some locations are seen to respond faster in response to oxygen breathing than others, but after 30 min, all voxels have reached pO_2 >200 torr. When the breathing gas was switched back to air, the tissue pO_2 values decreased and returned to a value (45 ± 6 torr) that was not significantly different from the baseline by the fifth measurement (25 min post switching). The average pO_2 of the last two measurements, while breathing air, was 44 ± 8 torr. Applying an exponential fit to the pO_2 data after switching back to air breathing (last 30 min of Fig. 2.15a) yielded kinetic rate constants k in the range 0.16 – 0.27 min^{-1} (Fig. 2.15b, R^2>0.99 for all datasets) with a mean value of k = 0.21± 0.04 min^{-1} (n=6). Measurements of HMDSO image intensities made on 3 rats (6 thighs) show a 10% reduction in intensity over 120 min (Fig 2.16). An exponential fit (solid line, R^2 = 0.90) to the data yields a half-life ($T_{1/2}$) of 15 ± 1 hr.

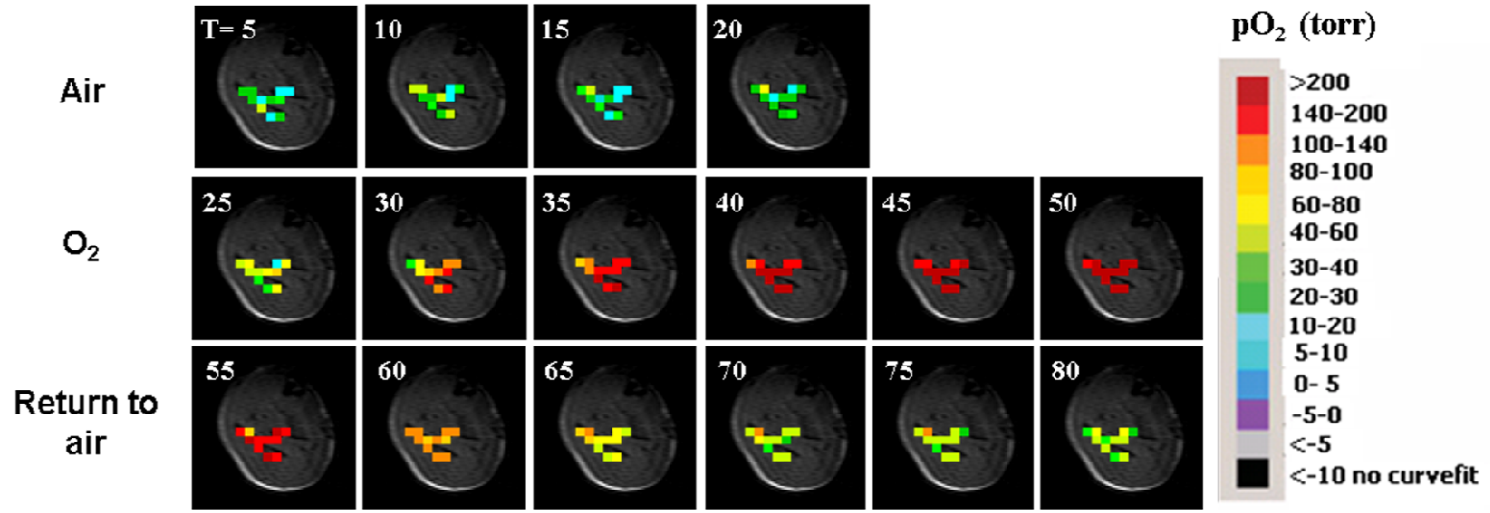

Figure 2.14: Mapping changes in oxygenation *in vivo* with respect to oxygen challenge using HMDSO nanoprobes. Spin-echo image of a representative Fisher 344 rat thigh muscle overlaid with time course PISTOL pO_2 maps (upper: baseline air breathing for 20 min, middle: 30 min of oxygen breathing and lower: 30 min of return to air breathing) show the response to hyperoxic gas intervention. The time scale (in minutes) is displayed on the images.

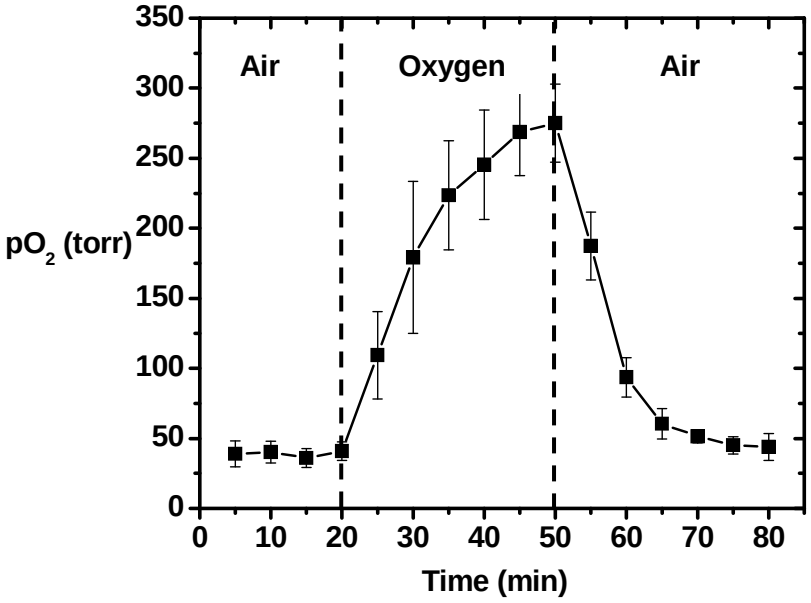

(a)

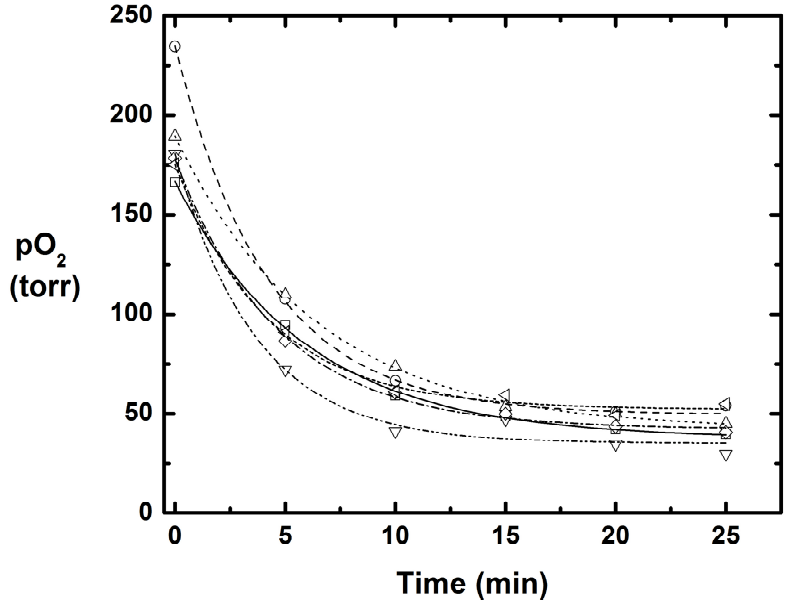

(b)

Figure 2.15 *In vivo* oxygen dynamics and consumption kinetics. (a) Dynamic changes in mean pO_2 measured *in vivo* using HMDSO nanoprobes in response to oxygen challenge (n=6). The time to equilibrate (95% of end pO_2 value) following breathing gas interventions (both O_2 and return to air) was determined to be 25 mins. (b) Data obtained after switching back to air breathing post oxygen challenge were fit to the equation $pO_2(t) = pO_2^{air} + A\,e^{-kt}$ for each animal and yielded values of kinetic parameter k (which reflects oxygen consumption and washout) in the range 0.16 – 0.27 min^{-1} (R^2>0.99 for all datasets) with a mean value of 0.21± 0.04 min^{-1}.

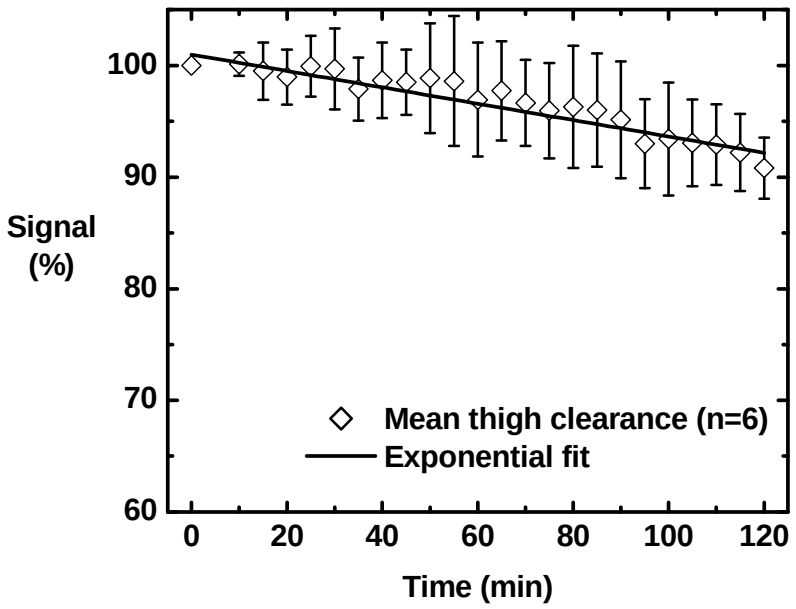

Figure 2.16 *In vivo* nanoprobe clearance. Clearance of HMDSO nanoprobes from rat thigh muscles was measured by MRI. Measurements made on 3 rats (6 thighs) show a 10% reduction in mean image intensity over 120 min. An exponential fit (solid line, $R^2 > 0.90$) to the data yields a half-life ($T_{1/2}$) time of 15 ± 1 hr for the nanoprobes.

2.4.2.2 Hyperbaric oxygen breathing intervention

Baseline pO_2 values were obtained by averaging four baseline pO_2 measurements while the rats breathed air. Figure 2.17 shows the pO_2 time course in rat thigh muscle in a representative animal overlaid on the scout image. In the cohort (n=6), mean baseline pO_2 measurements ranged from 32-66 torr (mean pO_2= 47.6 ± 10 torr), but remained stable in any given muscle with a mean fluctuation of ±5 torr over a period of 20 minutes (Fig. 2.18a). Changing the inhaled gas from air to NBO increased the mean thigh muscle pO_2 monotonically for 30 mins. The mean pO_2 value at the end of 60 minutes was 178.5 ± 55 torr. Switching the inhaled gas to air returned the mean thigh oxygenation back to a baseline pO_2 value of 55.8 ± 14 torr by 30 mins. During HBO challenge the mean thigh muscle pO_2 increased to 437± 97 torr (Fig 2.18a). 1-way ANOVA followed by Dunnett's multiple comparison test found significant increase in pO_2 values during NBO and HBO interventions when compared to initial baseline pO_2 and no significant differences while animal breathed air in between interventions. Applying a first order exponential fit to the pO_2 data after switching back to air breathing following NBO intervention yielded a kinetic rate constant (Fig 2.18b) k_{NBO} = 0.149 ± 0.03 min^{-1} (n=6). This is not significantly different statistically ($p>>0.05$, paired t-Test) to the value determined for the return kinetics after HBO intervention (k_{HBO} = 0.122 ± 0.03 min^{-1}).

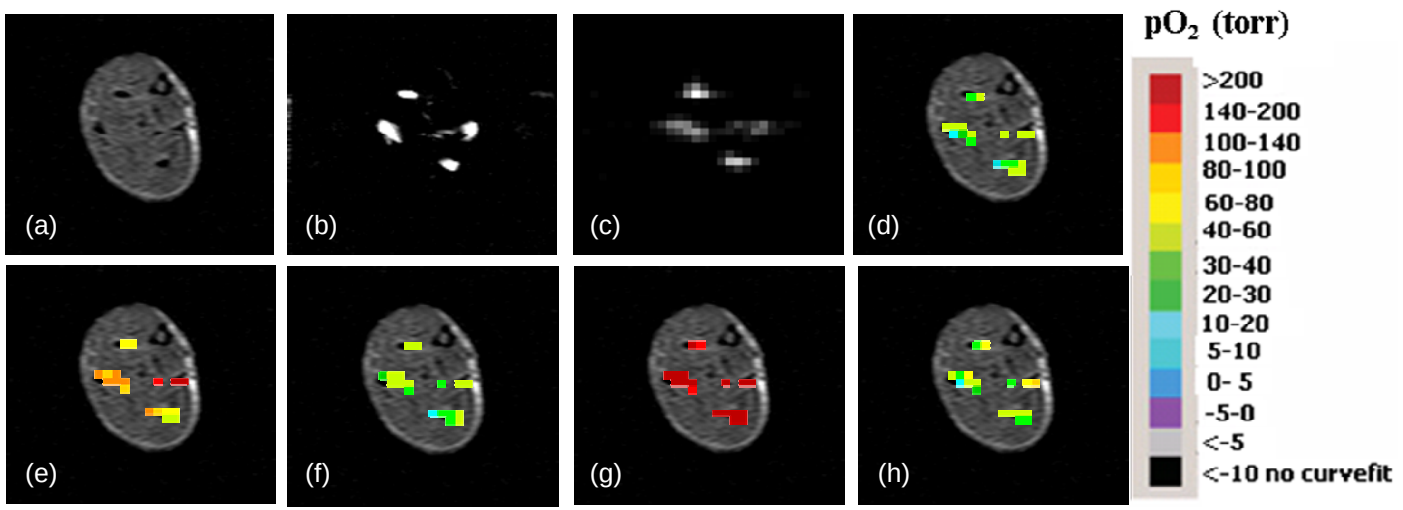

Figure 2.17 Tissue oximetry in rat thigh muscle using PISTOL technique following the administration of HMDSO nanoemulsion. a) T_1-wt scout image b) shift selective spin-echo and c) PISTOL image of the HMDSO nanoemulsion distribution. PISTOL pO_2 maps while the rat breathes d) air (baseline), e) normobaric O_2 (1 atm), f) return to air, g) hyperbaric O_2 (2 atm) and h) return to air overlaid on T1-wt images.

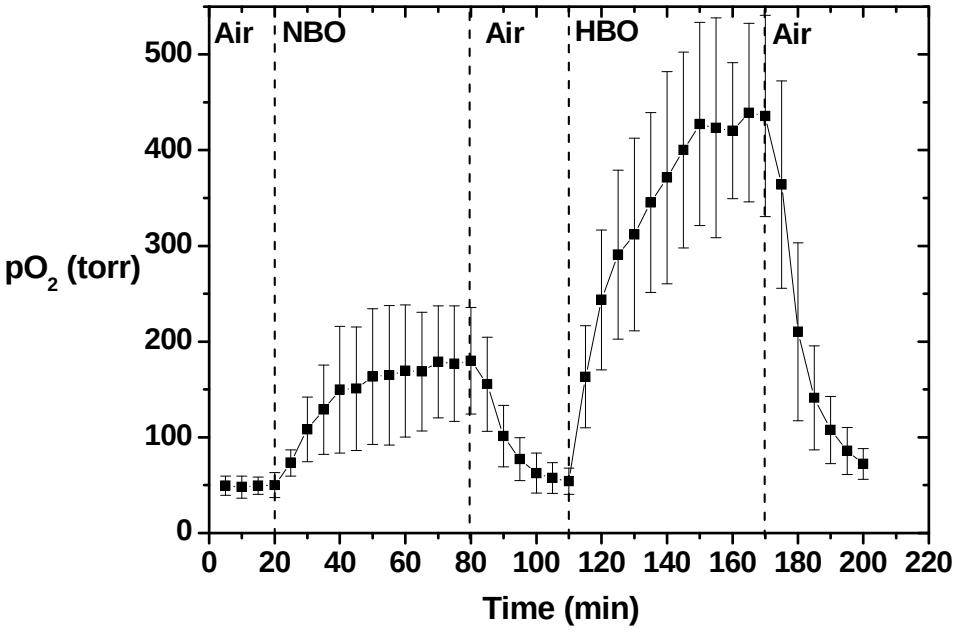

(a)

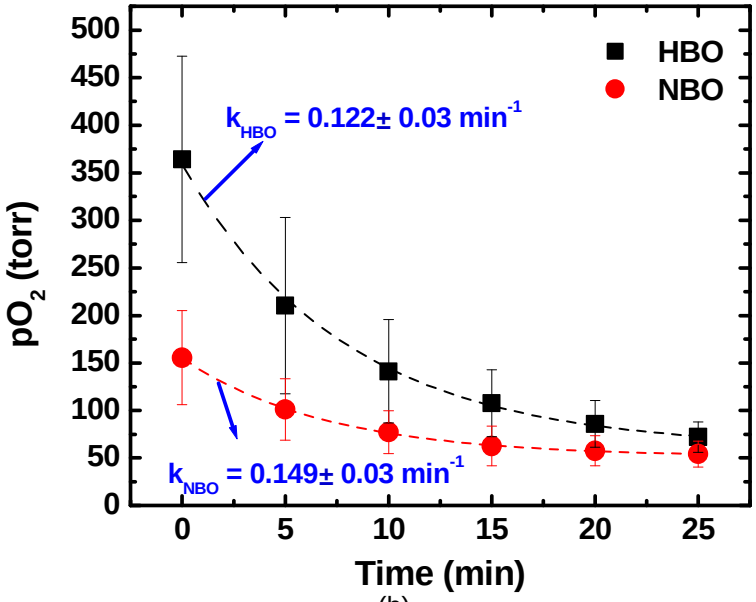

(b)

Figure 2.18 a) Dynamic changes in mean tissue oxygenation (pO_2) measured *in vivo* using HMDSO nanoemulsions in response to normobaric oxygen (NBO) and hyperbaric oxygen (HBO) oxygen challenge (n=6). b) Data obtained after switching back to air breathing post oxygen challenge were fit to the equation: $pO_2(t) = pO_2^{air} + A\,e^{-kt}$ to yield a kinetic parameter k (which reflects oxygen consumption and washout).

2.5 Discussion

In this study, I have demonstrated the feasibility of preparing HMDSO loaded nanoemulsions using two different PEGylated non-ionic surfactants and various HMDSO payloads and characterized their sensitivity to changes in pO_2. An optimal emulsion formulation was identified and further characterized with respect to temperature dependence and cytotoxicity. I also measured dynamic changes in tissue oxygenation using this emulsion formulation, following direct injection into tissue.

Nanoemulsions have been used for deposition, transportation and encapsulation of therapeutic or reporter molecules, which are either immiscible or toxic (45). A number of factors must be controlled to make stable emulsions within a desired particle size range. These include selecting an appropriate composition, controlling the order of addition of the components, and applying the energy in a manner that effectively ruptures droplets. An additional requirement is that the dispersed phase molecules must be essentially insoluble in the continuous phase so that Ostwald ripening (a molecular diffusion phenomenon characterized by the migration of dispersed phase molecules in smaller particles to larger particles) does not occur rapidly (57). The reporter molecule HMDSO is lipophilic and immiscible in aqueous solutions. I used a probe based ultrasonic agitation of the mixture of HMDSO, surfactant and de-ionized water to produce nanoemulsions. In the ultrasonication method, a vibrating solid surface agitates the premixed emulsion at ultrasonic frequencies, typically 20 kHz or larger, and high power, causing extreme shear and cavitation that breaks up droplets (58). An important consequence of this process is the large polydispersity in particle size. This necessitates further steps such as extrusion filtering in order to reduce polydispersity. I have seen reduction in both particle size and polydispersity using a two-step extrusion filtering through a 100 nm polycarbonate filter followed by a 50 nm filter (Fig. 2.6). Given the non-rigid nature of the nanoemulsion droplets, the filtration does not appear to exclude particle sizes less than the filter pore size, but is effective in rupturing the droplets into smaller ones. While ~5% change was observed using ^{1}H NMR in

water proton to HMDSO proton ratio (relative to ideal composition) only a ~1.5 % difference was observed in the ratios on comparing the filtered sample to the unfiltered sample. This indicates that some HMDSO is probably lost during the ultrasonication process but the material losses during the filtration process are minimal or at least even between the two phases. The increase in the line width for both water and HMDSO in the nanoemulsion is consistent with the higher viscosity of the nanoemulsion compared to the phase separated mixture of the two.

I have successfully modulated the pO_2 of HMDSO inside the emulsion droplet, as seen by both *in vitro* and *in vivo* studies, showing the potential for use of these emulsions as pO_2 nanoprobes for systemic delivery. The similarity of the calibration curves of the nanoemulsion to that of neat HMDSO at low surfactant concentration indicates that the surfactant layer does not prevent the exchange of O_2 between the pO_2 nanosensor and surrounding tissue (or solution). This is similar to the case of perfluorotributylamine where similar calibration curves were observed for the neat compound as for a 10% v/v emulsion with Pluronic F-68 (4% by weight) as surfactant (59). A parameter often used to compare different MRI pO_2 reporter molecules is η = slope/intercept of the R_1 vs pO_2 calibration curve. Neat HMDSO has an $\eta = 11.5 \times 10^{-3}$ $torr^{-1}$, which is intermediate to the fluorinated pO_2 reporter molecules HFB ($\eta = 22.8 \times 10^{-3}$ $torr^{-1}$) and 15-crown-5-ether ($\eta = 5.3 \times 10^{-3}$ $torr^{-1}$). HMDSO nanoprobes display a range of η (~7-13 $\times 10^{-3}$ $torr^{-1}$), but formulations with 5% surfactant or less have an η close to that of neat HMDSO, indicating the retention of pO_2 sensitivity of HMDSO in nanoprobes. The temperature dependence of the calibration constants A' and B' for the 5% HS-15-based nanoprobes was seen to be similar to neat HMDSO (42). Based on the temperature-dependent calibration curve, the calculated error in pO_2 at 37 ^oC was 1.0 torr/^oC, compared to 0.8 torr/^oC for neat HMDSO, when actual pO_2 value was 5 torr. The small differences seen are more likely due to the effect of differences in viscosities and oxygen solubilities of the sample which were calibrated as synthesized, without dilution.

Bi-exponential T_1 behavior was not observed in any of the magnetization recovery curves of the evaluated linear and cyclic siloxanes suggesting that the availability of oxygen to all the protons (end chain vs backbone) of the long chains was unhindered. I observed a decrease in η with respect to an increase in chain length of the linear siloxanes and the η values ranged from 7.5 – 11.5 $X10^{-3}$ $torr^{-1}$. Based on the temperature-dependent calibration curve of OMTSO, the calculated error in pO_2 at 37 ^oC was 1.4 torr/^oC, compared to 0.8 torr/^oC for neat HMDSO, when actual pO_2 value was 5 torr. Also the agents had a wide range of boiling points, enabling them to be used for different applications. For example, one can envision the preparation of OMTSO loaded nanoemulsions. Since the boiling point of OMTSO is much higher than HMDSO it would be less volatile during the emulsification process. For applications requiring faster time resolution, one can use cyclic or long chain linear siloxanes as the reporter molecules because of their shorter and smaller dynamic range of T_1's.

The mean baseline pO_2 and response to 30 min hyperoxic gas was similar to previous reports in rat thigh muscle using oximetry of neat HMDSO (42) and also to measurements reported using other techniques (60-63) in rat muscle. Baseline values were very similar across rats, but response to oxygen breathing varied with injection location. This is reflected in the higher standard deviation in pO_2 observed during hyperoxic intervention. Recently, oxygen consumption has been qualitatively measured in tissue based on EPR-based (64) and ^{19}F MR-based oximetry (65) using an exponential fit to the pO_2 vs time data post hyperoxic challenge. This yields a kinetic parameter that reflects the local tissue consumption and washout of oxygen. Using this approach I extracted the kinetic parameters for healthy rat thigh muscle and found a mean value of 0.21 ± 0.04 min^{-1}, which differs from the value of 0.09 min^{-1} reported by Diepart et al (64) mouse thigh muscle. Apart from the differences in species, the differences in the value for the kinetic parameter reported for muscle are more likely to be a consequence of different fitting methods. I have included a constant additive term to account for the baseline pO_2 along with the exponential term to account for consumption. This was observed to fit the

data very well and hence is a good empirical model. While the reported kinetic parameter k does not provide an absolute rate of oxygen consumption, it gives a measure of the local oxygen consumption and washout and has been used by Diepart and co-workers using EPR (64) and ^{19}F MR (65) oximetry to measure differences between normal and hyperthyroid mice thigh muscle and subcutaneously implanted liver tumors. This parameter k could be a promising prognostic marker for assessment of therapy in tumors. Applying a first order exponential fit to the pO_2 data obtained from athymic nude rats after switching back to air breathing following NBO intervention yielded a kinetic rate constant $k_{NBO} = 0.149 \pm 0.03\ min^{-1}$ (n=6). This is not significantly different statistically ($p>>0.05$, paired t-Test) to the value determined from the return kinetics after HBO intervention ($k_{HBO} = 0.122 \pm 0.03\ min^{-1}$).

The clearance of HMDSO nanoprobes was seen to be much faster than neat HMDSO ($T_{1/2}$ = 15 hr vs 35 hr) reported earlier by us in a separate cohort of animals (42). This is possibly due to the different modes of clearance post intra-muscular injection in the two cases: macrophage clearance and slow oxidative metabolism for neat compounds or microemulsion (66) as opposed to convective transport and lymphatic clearance for nanoemulsions (67). For the current study I have used direct intra-tissue injection, as our goal was to test the utility of pO_2 nanoprobes for ^{1}H MR oximetry and not to investigate pharmacokinetics of these nanoprobes. In any case systemic delivery of nanoprobes may not permit investigation of muscle interstitial pO_2 due to low permeability of normal vasculature to macromolecules and low interstitial volume fraction in muscle tissue. Nanoemulsion formulations may be preferable to neat compounds for intra-tissue injections of pO_2 reporter molecules where clearance is desired. However, one should bear in mind the additional volume required in case of emulsions due to the lower volume fraction of the reporter molecule (here 40% v/v) compared to neat compounds (100% v/v). A more rigorous study could involve comparing clearance of neat HMDSO and naemulsions in the same animals after direct intra-tissue injection.

In summary, I have demonstrated for the first time the feasibility of various siloxanes and HMDSO loaded nanoemulsions for use as pO_2-sensing probes for ^1H MR oximetry. I characterized the nanoemulsions by their size and sensitivity to changes in pO_2, and identified an optimal formulation to measure dynamic changes in tissue oxygenation using these nanoprobes, following direct injection into tissue as proof of principle. With systemic delivery for tumor oximetry in mind, our research group further plans to optimize the synthesis procedure to obtain smaller nanoprobes, which could improve tumor uptake and reduce the bias in delivery to well vascularized regions as has been seen with use of microemulsions (27).

CHAPTER 3

EVALUATION OF Gd-DOTA MONOAMIDE CONJUGATE OF 2-NITROIMIDAZOLE (GdDO3NI) AS A HYPOXIA TARGETING T_1 CONTRAST AGENT

3.1 Abstract

Heterogeneously distributed hypoxic regions in tumors are known to affect radiation sensitivity and promote development of metastases. 2-nitroimidazole has been previously reported to accumulate in hypoxic tissues due to an enzyme mediated reduction of the nitro group under hypoxic conditions. Radiolabeled nitroimidazoles like [^{18}F]Fluoromisonidazole (^{18}F-MISO) are being currently used as hypoxia targeting PET agents. I report here the *in vitro* and *in vivo* evaluation of a gadolinium [Gd] - DOTA monoamide conjugate of 2-nitroimidazole, GdDO3NI, as a potential magnetic resonance imaging (MRI) probe to detect hypoxia. For comparison, Gd-DOTA-(n-butyl)monoamide, GdDO3ABA, was used as the control agent. The relaxivities of GdDO3NI in solution and tissue simulating agarose gel phantom were determined to be 5.21 ± 0.04 mM^{-1} s^{-1} and 5.45 ± 0.29 mM^{-1} s^{-1} respectively, at 200 MHz and 37℃. The *in vitro* cell uptake experiment showed a significantly higher retention of GdDO3NI by 9L rat glioma cells incubated under hypoxic conditions compared to normoxia. Contrast agent kinetics were compared following intravenous injections of GdDO3NI and GdDO3ABA in rat prostate tumor bearing animals. The time course signal intensities (qualitative) and the calculated Gd concentrations (semi-quantitative) showed a clear difference in the enhancement patterns for the two agents (GdDO3ABA and GdDO3NI) and between well perfused (periphery) and poorly perfused (center) regions of R3327 Dunning rat prostate AT1 tumors. A statistically significant difference in contrast enhancement/concentration was observed in poorly perfused (center/potentially hypoxic) regions at late time points (85-150 min) between GdDO3ABA and GdDO3NI injected animals. Gd concentrations obtained from ICP-MS analysis of tumor

samples correlated well with the concentration profiles observed. In AT1 tumors, no statistically significant differences in GdDO3NI contrast kinetics between air and oxygen breathing were observed. But I observed a significant decrease in the uptake of GdDO3NI in the central regions of HI tumors when the animals breathed oxygen when compared to air. These observations are in accordance with the earlier reported behavior of hypoxia retention in AT1 and elimination in HI tumors in response to oxygen breathing, by other oximetry techniques. Therefore, GdDO3NI shows promise as a hypoxia targeting small molecular weight contrast agent.

3.2 Introduction

Oxygen is essential for tissue health and survival. It is also an important variable in the treatment of many medical conditions including tumors, peripheral vascular disease and stroke. Hypoxic regions, typically distributed heterogeneously in solid tumors are known to affect radiation sensitivity and promote development of metastases (10). Further, the extent of hypoxia can vary greatly in radiographically similar tumors in many cases (68). Therefore the ability to image hypoxia *in vivo* on an individual basis not only will provide useful prognostic information but also is necessary for developing hypoxia targeted therapeutic approaches (10).

Currently there exist a number of ways by which tissue oxygenation status can be assessed *in vitro* (tissue samples) or *in vivo* (both invasive and noninvasive). *In vitro* methods of assessing hypoxia in tissues include immunohistochemical staining for a) intrinsic markers of hypoxia (e.g., carbonic anhydrase IX (CA-IX) and hypoxia inducible factor-1 (HIF-1)) (69) and b) for the adducts of externally administered nitroimidazoles (70). The invasive technique uses a polarographic needle electrode (18) to obtain quantitative pO_2 measurements but its utility is limited only to tumor sites that are readily accessible.

As reviewed recently (16,17), noninvasive hypoxia imaging approaches can be broadly classified into MR and non-MR based techniques. Non-MR-based methods include: fluorescence imaging (19), phosphorescence quenching (20), near-infrared spectroscopy (21),

SPECT (22) and PET (23,24) imaging. MR-based methods include: blood oxygen level dependent (BOLD) imaging (25), electron paramagnetic resonance (EPR/ESR) (26), fluorocarbon relaxometry (27) using echo planar imaging for dynamic oxygen mapping (FREDOM) (28).

Another popular way of assessing hypoxia exploits the principle of selective enzyme mediated reduction of nitro group of 2-nitroimidazole containing compounds under hypoxic conditions (71). Though initial studies concentrated on using 2-nitroimidazole analogs to sensitize hypoxic tumors to ionizing radiation (72-74), soon the prospect of these compounds as potential noninvasive hypoxia-homing probes was realized and several radiolabeled nitroimidazole derivatives have been developed to image hypoxic tissues *in vivo* (75,76). Currently, [^{18}F]Fluoromisonidazole (^{18}F-MISO) (29,30), [^{18}F]Fluoroazomycin arabinoside (^{18}F-AZA) (77), [^{18}F] EF5 (78) are being used as a hypoxia targeting PET imaging agents whereas [^{19}F] Tri-Fluoromisonidazole (TF- MISO) (31) has been used a fluorine MRI probe to qualitatively image hypoxia.

Since MRI based noninvasive imaging is particularly suitable for longitudinal measurements and generation of three-dimensional (3D) spatial maps of tumor, in this study, we investigated the potential of GdDOTA monoamide conjugate of 2-nitroimidazole, GdDO3NI (Fig 3.1 a), for use as a novel hypoxia targeting MRI T_1 contrast agent. For comparison, Gd-DOTA-(n-butyl)monoamide, GdDO3ABA (Fig 3.1 b), was used as the control agent.

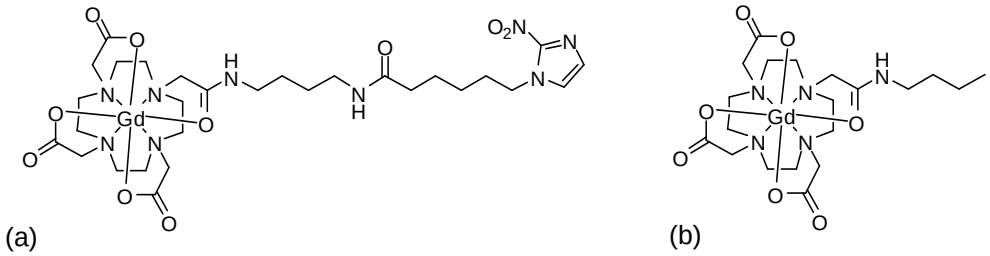

Figure 3.1 Structures of a) GdDO3NI and b) GdDO3ABA

I examined contrast agent kinetics of GdDO3NI and GdDO3ABA following intravenous injections in Dunning R3327 rat prostate AT1 tumor bearing animals. Further I demonstrate the potential of GdDO3NI in monitoring changes in hypoxia fraction of solid tumors with known levels of hypoxia (Dunning R3327 rat prostate tumors- AT1 and HI) following 100% oxygen breathing.

3.3 Materials and Methods

The evaluated contrast agents, GdDO3NI and GdDO3ABA, were synthesized by my collaborators Drs. Rojas-Quijano, Trokowski, Kovacs and Sherry, in the Advanced Imaging Research Center - UT Southwestern Medical Center and a detailed description of the synthesis can be found elsewhere (79). All MR studies were performed on a Varian INOVA 4.7T horizontal-bore MR system equipped with actively shielded gradients.

3.3.1 Spin- lattice relaxivity (r_1) measurements

In vitro measurement of T_1 relaxivity (r_1) of these agents was performed at 37 ℃ using two serial dilution phantoms (Fig 3.2), one in phosphate buffered saline (PBS) solution and the other a tissue simulating 1% agarose phantom. The concentrations used for the measurements were in the range 0- 4 mM. For the r_1 measurements, a spin-echo sequence was employed with several TR values (0.1-6 s) and TE of 12 ms. Relaxivity was extracted as slope of linear fit to relaxation rates (R_1) vs. concentration.

4 mM	3.5	3
2.5	2	1.5
1	0.5	0

Figure 3.2 Schematic showing the concentration of compounds in mM in each vial of the phantom. 0 mM refers to PBS.

3.3.2 In vitro MRI imaging of cell uptake

Rat 9L-glioma cells were grown to confluency in culture dishes using Dulbecco's Modified Eagle's Medium (DMEM) supplemented with 10% fetal bovine serum, 1% L-glutamine and 1% penicillin/streptomycin; this medium was replaced with 8 mL of un-supplemented DMEM prior to the uptake experiment. One plate of cells was made hypoxic by exposing it to nitrogen gas (1 L/min) in a small chamber for two hours at room temperature while two other plates were exposed to room air; 1 mL of phosphate buffer saline (PBS) was then added to one of the latter two samples (negative control), and 1 mL of 45 mM GdDO3NI to the remaining two samples (for a final concentration of 5 mM). All samples were then incubated for a period of two hours at room temperature (negative control and reference samples in air, hypoxic sample in nitrogen at 1L/min). After incubation, cells were rinsed three times with PBS, trypsinized, and centrifuged in 15 mL tubes at 2500 rpm for 5 min. Excess buffer was removed from the pellets, and the samples were transferred to 0.2 mL tubes for a final centrifugation at 14500 rpm for 5 min.

The three sample tubes were positioned in a home-built 2 cm volume coil and imaged at 4.7 T. Images were obtained for 10 values of TR in the range of 0.1s – 6s and a TE of 12 ms following which, a T_1 map was generated from this data set. Using home-built software written in MATLAB, a region of interest (ROI) analysis was performed to extract voxel T_1 values for each pellet. For statistical comparisons, pair wise student t-tests were performed on the voxel data.

3.3.3 In vivo MRI imaging

3.3.3.1 Kinetics of GdDO3NI vs GdDO3ABA

For *in vivo* studies, 10 Copenhagen rats were implanted subcutaneously on the thigh with syngeneic Dunning R3327 AT1 prostate tumors. All the animal experiments were approved by the Institutional Animal Care and Use Committee. Imaging studies were performed when the

tumor sizes reached ~3 cc. The anesthetized animals (1.5% isoflurane in 1 L/min inhaling gas) were passively restrained and the body temperature was maintained at 37 ℃ by a warm circulating water pad. Subcutaneous tumor along with the leg of the rat was placed in a 3.5 cm diameter home-built volume coil and multislice T_1-weighted images (TR/TE = 200/10 ms, FOV= 5 cm X 5 cm, matrix=128 X128, slice thk= 1 mm) were obtained pre and post injection of 0.1 mmole/kg body wt contrast agent (GdDO3ABA or GdDO3NI, n= 5 each). Images were acquired every 30 seconds during baseline and upto 3 minutes post injection followed by acquisition every minute up to 15 minutes and then once every 10 minutes up to 150 min post injection.

3.3.3.2 Kinetics in AT1 and HI tumors while breathing air or 100%O_2

To investigate the effect of 100% oxygen breathing on decreasing the hypoxia in solid tumors with known levels of hypoxia, we implanted Dunning R3327 rat prostate - AT1 and HI tumors into 2 groups with 4 animals each. Imaging studies were performed when the tumor sizes reached ~3 cc. On day 1 of imaging, a similar protocol to that described in 3.3.3.1 was followed while the animals breathed air and the experiment was repeated 24 hrs later while the animals breathed 100% O_2 during the entire duration of the experiment.

All the data analysis was performed using in-house MATLAB routines and segmenting of the voxels into well perfused and poorly perfused regions in the tumor was performed by a criterion of 50% enhancement at 90 s post injection.

3.3.4 Ex vivo tumor sample analysis

3.3.4.1 Histology and Immunohistochemistry

To confirm the existence of hypoxia, AT1 tumor samples were collected for histological evaluation. The hypoxia marker, pimonidazole hydrochloride (60 mg/kg, Hypoxyprobe-1; NPI, Inc., Belmont, MA) dissolved in saline was injected into the tail vein to assess tumor hypoxia. Ninety minutes later, rats were euthanized. Tumors were excised and sections were cut through

the center of the tumor. These tumor sections were then fixed in 10% formalin and embedded in paraffin. Before H&E staining and immunohistochemistry of hypoxia, 5 μm thick cut sections were deparaffinized in xylene and ethanol and rehydrated in water. Hypoxic regions were detected using mouse monoclonal antibody Mab1 (1:50; NPI, Inc.) and FITC-conjugated goat antimouse secondary antibody (1:100 dilution; Jackson Immunoresearch Laboratories,WestGrove, PA). After mounting with Vectorshield medium (Vector Laboratories, Burlingame, CA), the slides were observed under a Fluorescent microscope with green fluorescence excitation (450–490 nm).

3.3.4.2 Inductively Coupled Plasma - Mass Spectroscopy (ICP-MS)

To determine the elemental concentration of retained gadolinium, ICP-MS analysis was performed. The sample size required to be reasonably likely (α = 5% and β = 5%) to detect an effect of magnitude similar to the Gd concentration profiles (MR based) of the centers, was determined to be n=3. 5 mm thick tumor sections were cut and further segmented in periphery and center regions using a scalpel. These samples were then frozen immediately in liquid nitrogen and sent for ICP-MS analysis (Galbraith laboratories, Inc., Knoxville, TN).

3.4 Results

3.4.1 In vitro relaxivity study

For PBS phantom, a linear fit to the longitudinal relaxation rates (R_1) vs. concentration data yielded the relaxivity value of 4.74 ± 0.03 mM^{-1} s^{-1} and 5.21 ± 0.04 mM^{-1} s^{-1} for GdDO3ABA and GdDO3NI, respectively (Fig 3.3 a). Similarly, the relaxivities of GdDO3ABA and GdDO3NI in the tissue simulating 1% agarose phantom were determined to be 4.76 ± 0.27 mM^{-1} s^{-1} and 5.45 ± 0.29 mM^{-1} s^{-1} respectively (Fig 3.3 b). The increase in the relaxivity of GdDO3NI when compared to GdDO3ABA can be attributed to the elongation of the rotational correlation time (τ_R) due to the presence of the long pendant arm.

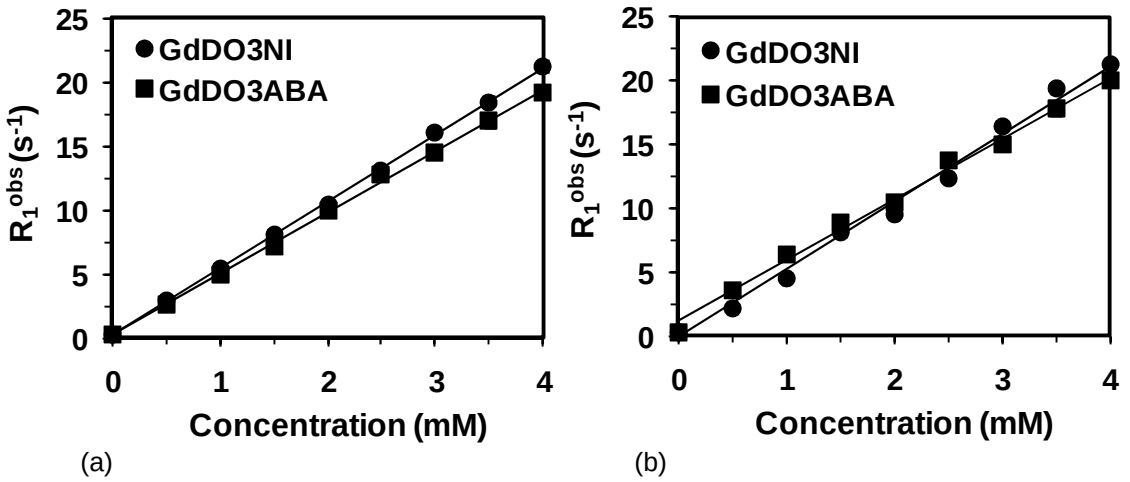

Figure 3.3 Graphs of R_1 vs. concentration for the agents GdDO3NI and GdDO3ABA in a) PBS solution and b) tissue simulating 1% agarose phantom.

3.4.2 In vitro cell uptake study

To determine the uptake of GdDO3NI under hypoxic conditions, 9L rat glioma cells were used as an *in vitro* model for this study. Hypoxia was induced in one sample of 9L cells by exposing them to nitrogen (N_2) gas for 2 hours before the addition of the GdDO3NI. Following this, the sample was prepared to contain 5 mM of GdDO3NI and was incubated for two more hours in N_2. A reference sample was incubated at the same final concentration but in the presence of air.

T_1-weighed images, T_1 maps and T_1 voxel analysis for three of these samples are shown in Figures 3.4 a, b and c, respectively. ROI analysis on the T_1 maps of the negative control, reference and hypoxic samples resulted in relaxation times of 1.5 ± 0.2 s, 1.3 ± 0.1 s, and 0.7 ± 0.1 s, respectively. The hypoxic sample showed a significant decrease in T_1 when compare to both the negative control and reference samples. This data clearly indicates that the uptake of GdDO3NI is oxygen sensitive as seen by the higher uptake and retention in cells incubated under hypoxic conditions.

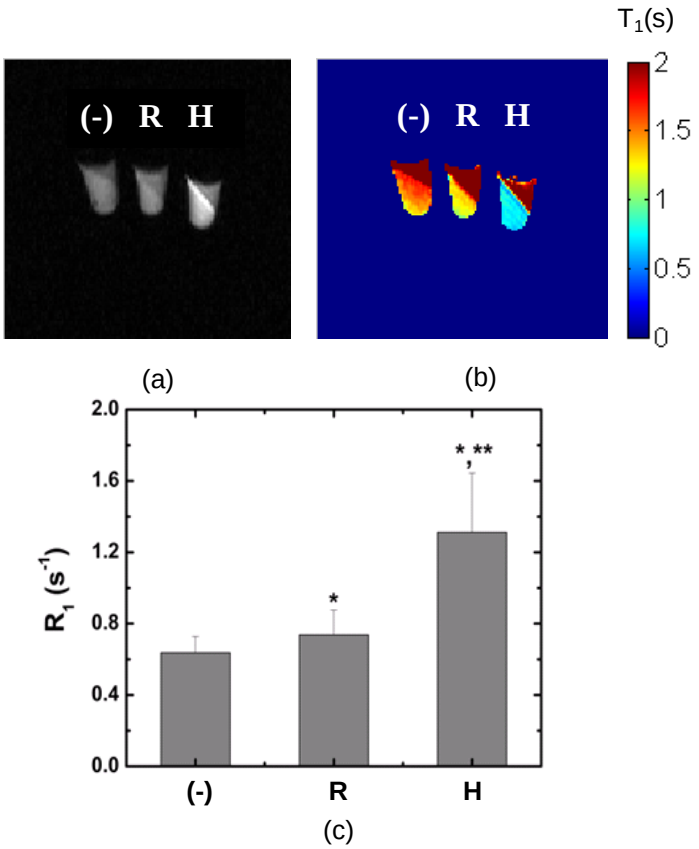

Figure 3.4 *In vitro* MRI imaging of 9L rat glioma cells. (a) T_1-weighed images of negative control (-), normoxic incubation reference (R) and hypoxic incubation (H) samples; (b) T_1 map; (c) T_1 ROI voxel analysis (* = p <0.05 compared to negative control (-); ** = p<0.05 compared to reference sample (R)).

3.4.3 In vivo contrast agent kinetics study

3.4.3.1 GdDO3ABA vs GdDO3NI in AT1 tumors

Contrast agent kinetics were compared following intravenous injections of GdDO3NI and GdDO3ABA in Dunning R3327 AT1 rat prostate tumor bearing animals. Following the acquisition of T_1- weighted time course data (Fig 3.5), segmentation for data analysis was performed as shown in Figure 3.6

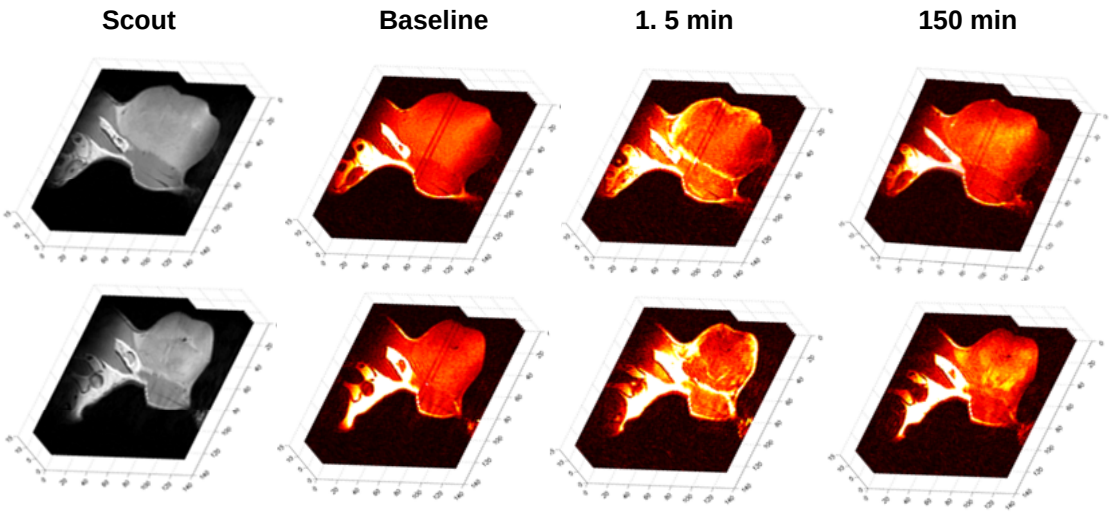

Figure 3.5 T_2 - wt 3D stacks and colormap T_1-wt 3D stacks (displayed on a common scale) following injection of 0.1mmole/kg body wt GdDO3ABA (top row-control) and GdDO3NI (bottom row) at pre injection, 1.5 min and 150 min.

First an ROI was drawn on the T_2 - wt scout image to delineate the tumor. The percentage signal enhancement map at 1.5 min post injection relative to pre injection (baseline) was used to segment the total tumor region into periphery or well perfused region (% enhancement ≥ 50%) and the remaining as center or poorly perfused region (% enhancement < 50%). Central voxels that showed <10% enhancement at 90 minutes post injection were also excluded, since they were more likely to represent necrotic regions. The mean signal intensities for the periphery and center regions were normalized to the thigh signal intensity to compensate for differences in agent injection between animals and compared over time with each other and between agents. The statistical significance of differences in normalized mean intensities at each time point was estimated by using 2-tailed unpaired student t-test.

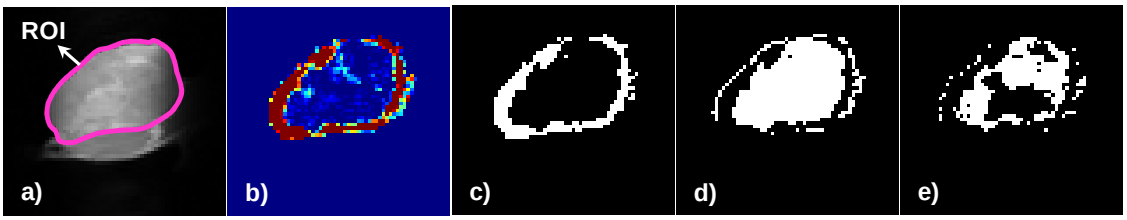

Figure 3.6 Image segmentation procedure for data analysis. (a) A representative T_2-wt scout image showing the tumor (ROI) and thigh of an animal. (b) The percent signal enhancement map at 1.5 min post injection relative to pre injection. (c) Periphery (or well perfused) region segmented by using % enhancement > 50%. (d) central region with necrotic regions and (e) Center (or poorly perfused) region excluding necrotic regions segmented by using % enhancement > 10% & < 50%.

Signal Intensity time course: Qualitatively, the time course signal intensities showed a clear difference in the enhancement patterns for the two agents (GdDO3ABA and GdDO3NI) and between well perfused and poorly perfused regions (Fig 3.7 a & b). In case of GdDO3NI, a statistically significant difference in the contrast enhancement was observed between peripheral (well perfused and consequently well oxygenated) regions and central (poorly perfused and potentially hypoxic) regions at late time points (80-150 min) where as for GdDO3ABA, no statistically significant difference between the regions was observed at late time points.

Gd concentration time course: We calculated the Gd concentration using the relation $[Gd] = (R_{1,post} - R_{1,pre})/r_1$, where $R_{1,pre}$ and $R_{1,post}$ are the relaxation rates and r_1 is the relaxivity of the contrast agent in agar phantom. Semi-quantitatively, the time course of Gd concentration showed no statistically significant differences in the clearance patterns for the two agents GdDO3ABA and GdDO3NI, in thigh regions (Fig 3.8 a) and periphery (Fig 3.8 c). In case of central region, a statistically significant difference in the Gd concentration was observed (Fig 3.8 b) between animals injected with GdDO3ABA and GdDO3NI, at late time points (80 -150 min).

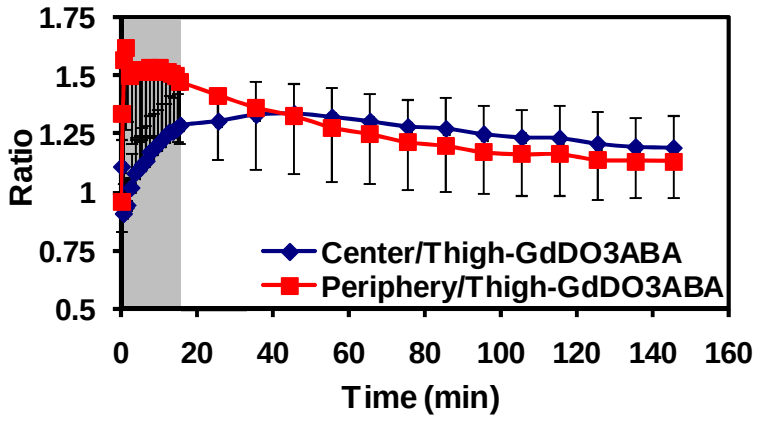

(a)

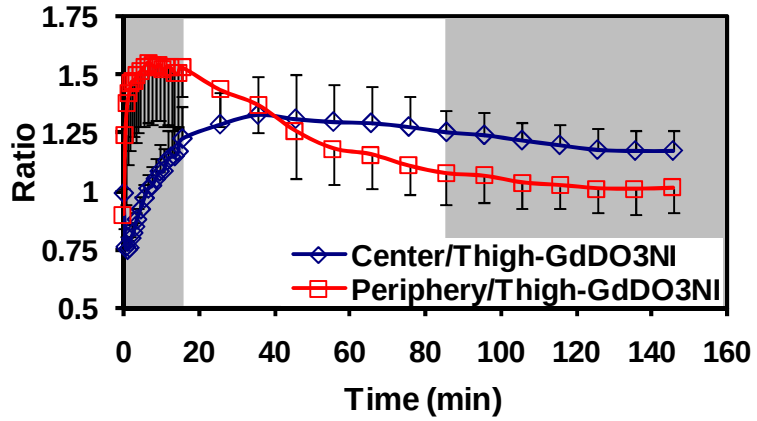

(b)

Figure 3.7 Comparing time course of normalized mean intensities (n = 5) for well perfused (periphery) and poorly perfused regions (center) for (a) GdDO3ABA and (b) GdDO3NI. Region shaded in gray represents $p<0.05$ following 2-tailed unpaired t-test.

As shown in Figure 3.9 and 3.10, Gd concentration maps created at 150 minutes post injection of contrast agents clearly reveal higher uptake of GdDO3NI in central regions of the tumor (Fig 3.10 c) when compared to GdDO3ABA (Fig 3.9 c).

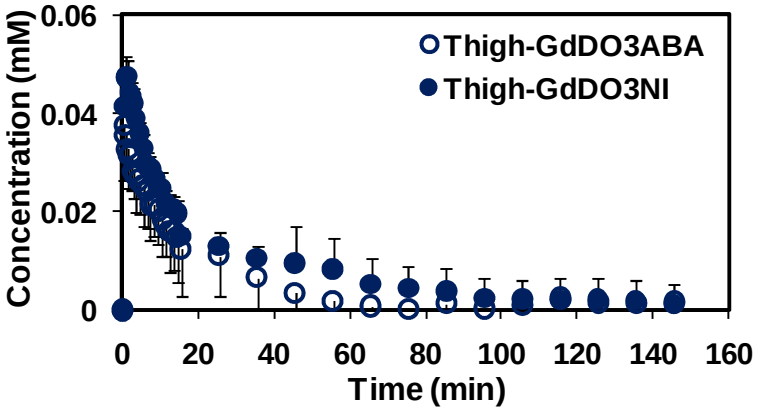

(a)

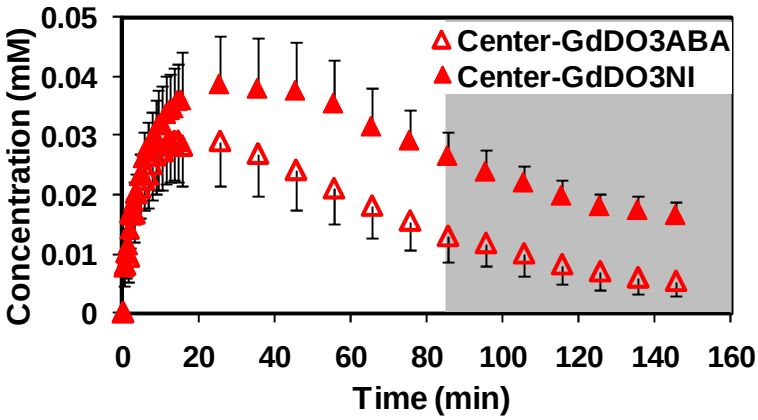

(b)

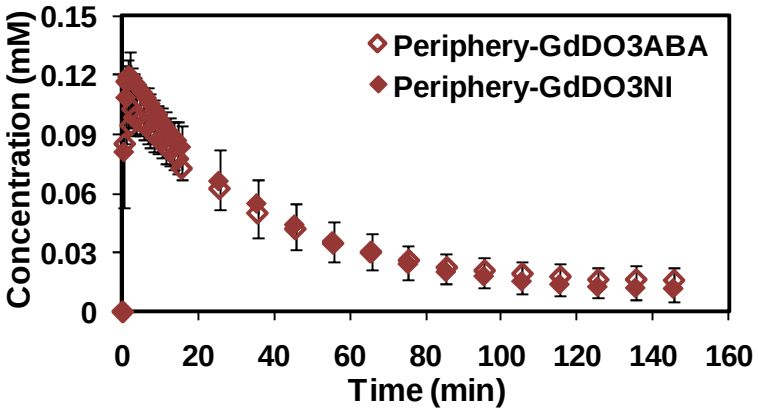

(c)

Figure 3.8 Kinetics of mean Gd concentration (n=5) for (a) thigh, (b) poorly perfused (central) regions and (c) well perfused (peripheral) region of tumors in animals injected with GdDO3ABA and GdDO3NI. Region shaded in gray represents $p<0.05$ following 2-tailed unpaired t-test.

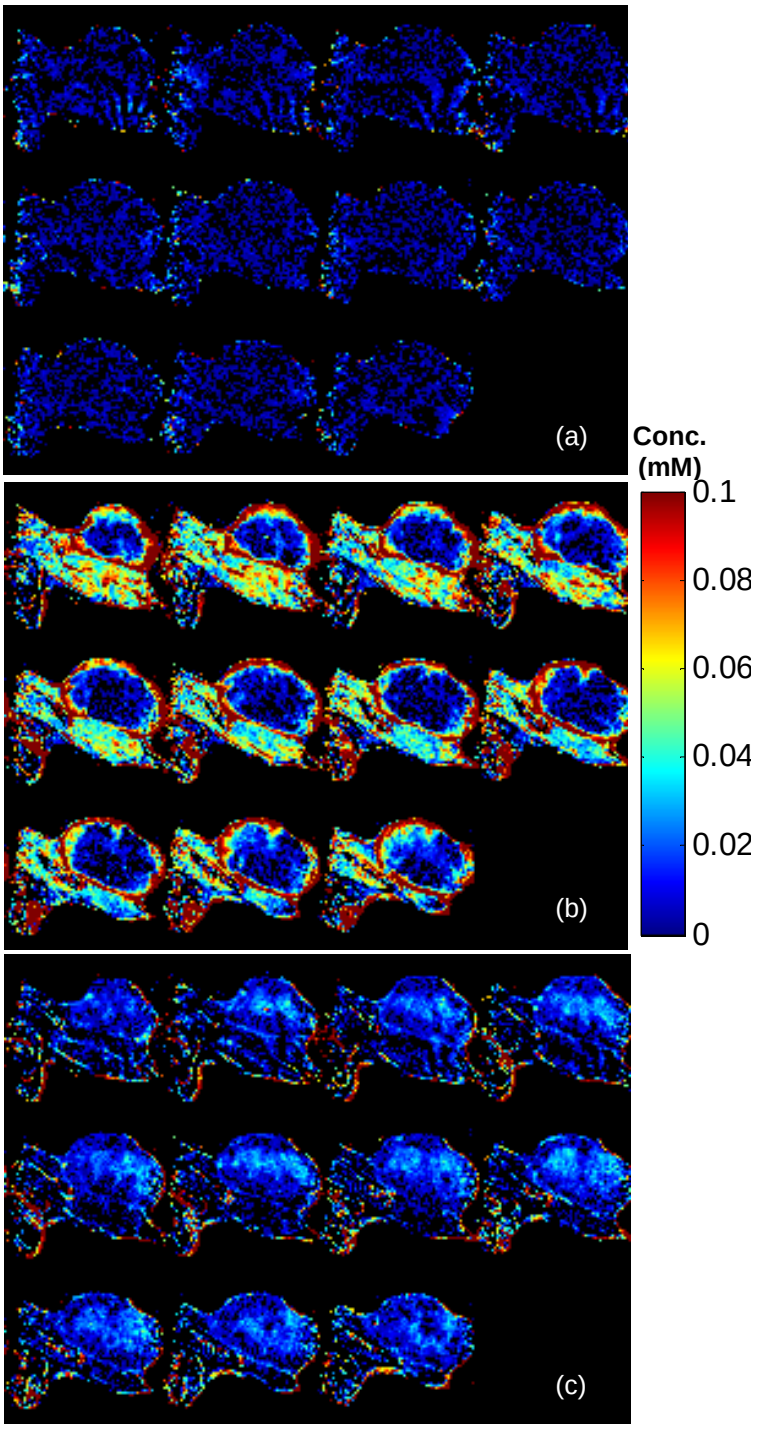

Figure 3.9 Gd concentration maps of multiple slices of representative AT1 tumors at 0 minutes (a), 3 minutes (b) and 150 minutes (c) following the injection of GdDO3ABA.

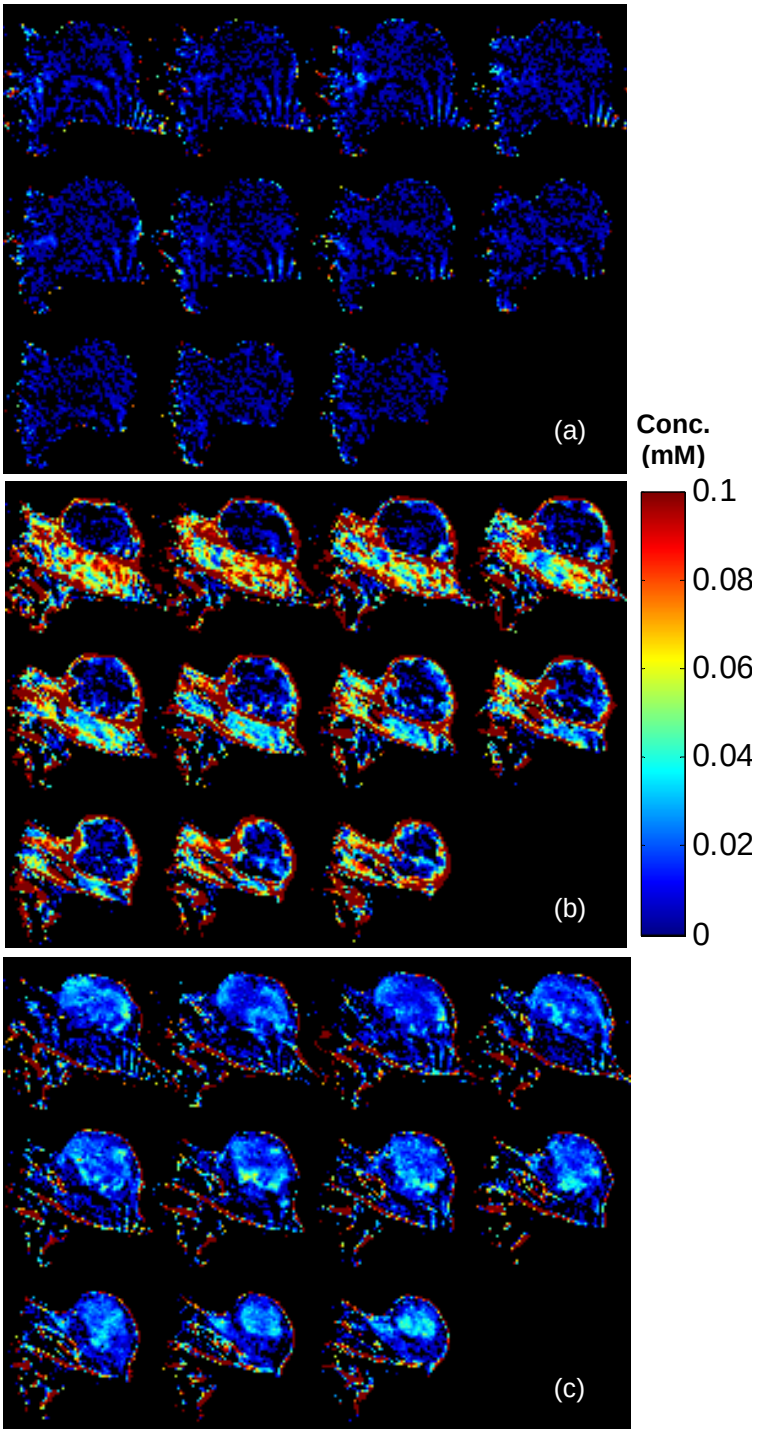

Figure 3.10 Gd concentration maps of multiple slices of representative AT1 tumors at 0 minutes (a), 3 minutes (b) and 150 minutes (c) following the injection of GdDO3NI. The images clearly show an enhanced retention of GdDO3NI in the central regions of the AT1 tumor at 150 minutes.

3.4.3.2 Kinetics of GdDO3NI in AT1 and HI tumors while breathing air and 100%O_2

To investigate the use of GdDO3NI to probe the ability of hyperoxic gas breathing in eliminating the hypoxic fraction in tumors, we chose two tumor sublines (AT1 and HI) with well - known responses of hypoxia to oxygen breathing. Time course image acquisition and data analysis were performed using the procedures described in 3.3.3.2 and 3.4.3.1, respectively.

As shown in Figure 3.11, Gd concentration maps of multiple slices of representative AT1 and HI tumors at 150 minutes after the injection of GdDO3NI following air and oxygen breathing. AT1 tumor showed an enhanced retention of GdDO3NI in similar central regions following air and oxygen breathing whereas central regions of HI tumor clearly showed a decrease in Gd concentrations while the animal breathed oxygen.

For the two tumor types, the statistical significance of differences in concentrations at each time point between air and oxygen breathing datasets was estimated by using repeated measures 2-way ANOVA followed by Bonferroni's multiple comparison test.

In the AT1 tumors (3.05 ± 0.19 cc and 281 ± 10 g), the time course of Gd concentration showed no statistically significant differences in the clearance patterns of periphery (Fig 3.12 a), central tumor regions (Fig 3.12 b) and in thigh regions (Fig 3.12 c) at late time points between air and oxygen breathing protocol. In the HI tumors (3.28 ± 0.49 cc and 286 ± 8 g), the time course of Gd concentration showed no statistically significant differences in the clearance patterns of peripheral regions (Fig 3.13 a) and in thigh regions (Fig 3.13 c) between air and oxygen breathing protocol. In the case of center region (Fig 3.13 b), a statistically significant decrease in Gd concentration was observed when the animals breathed oxygen as compared to air.

Histogram of Gd concentrations in central regions of HI tumors (Fig 3.14b) showed a clear left shift demonstrating the decrease in Gd concentrations after oxygen breathing where as AT1 tumors didn't show any change in the histogram pattern (Fig 3.14a).

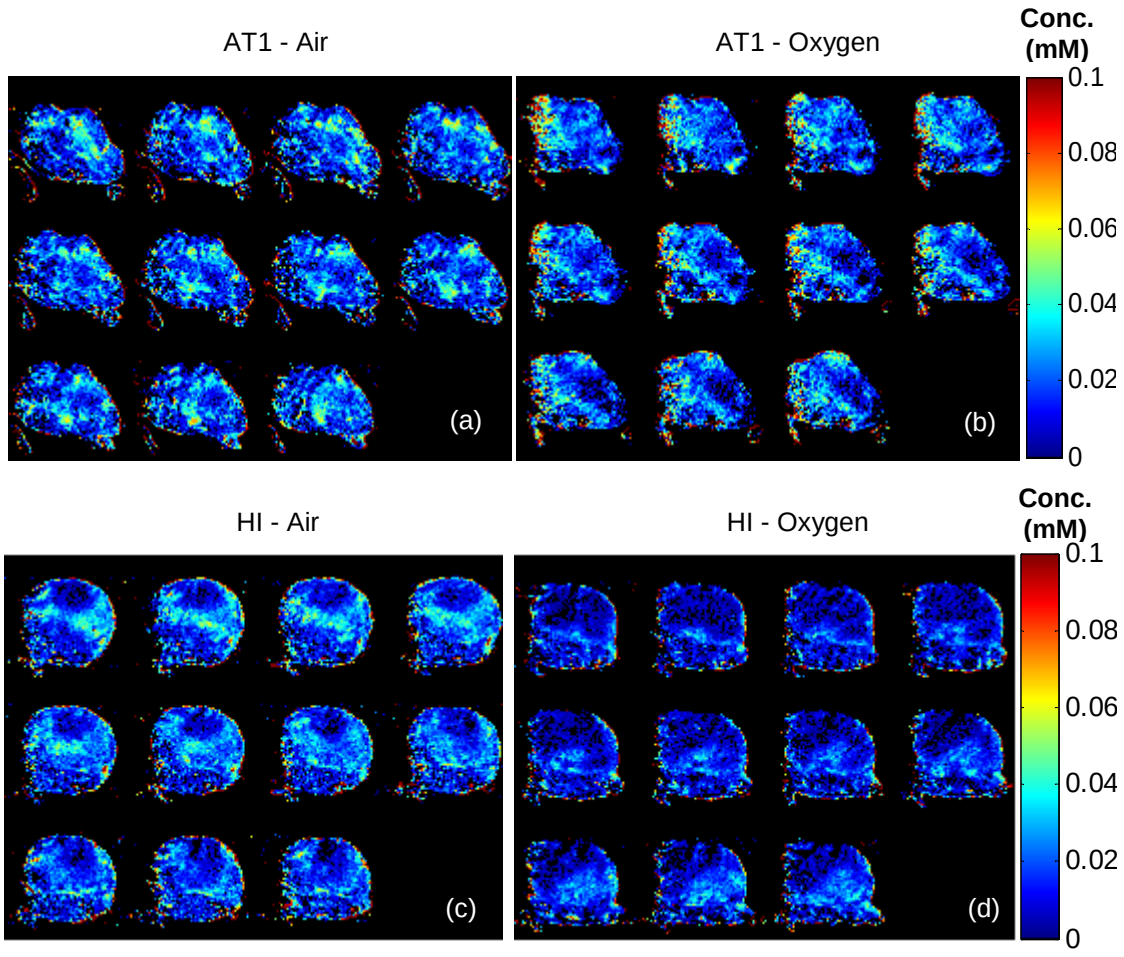

Figure 3.11 Gd concentration maps of multiple slices of representative AT1 (top row) and HI (bottom row) tumors at 150 minutes after the injection of GdDO3NI following air (a, c) and oxygen (b, d) breathing. AT1 tumor showed an enhanced retention of GdDO3NI in similar central regions following air and oxygen breathing whereas central regions of HI tumor clearly showed a decrease in Gd concentrations while the animal breathed oxygen.

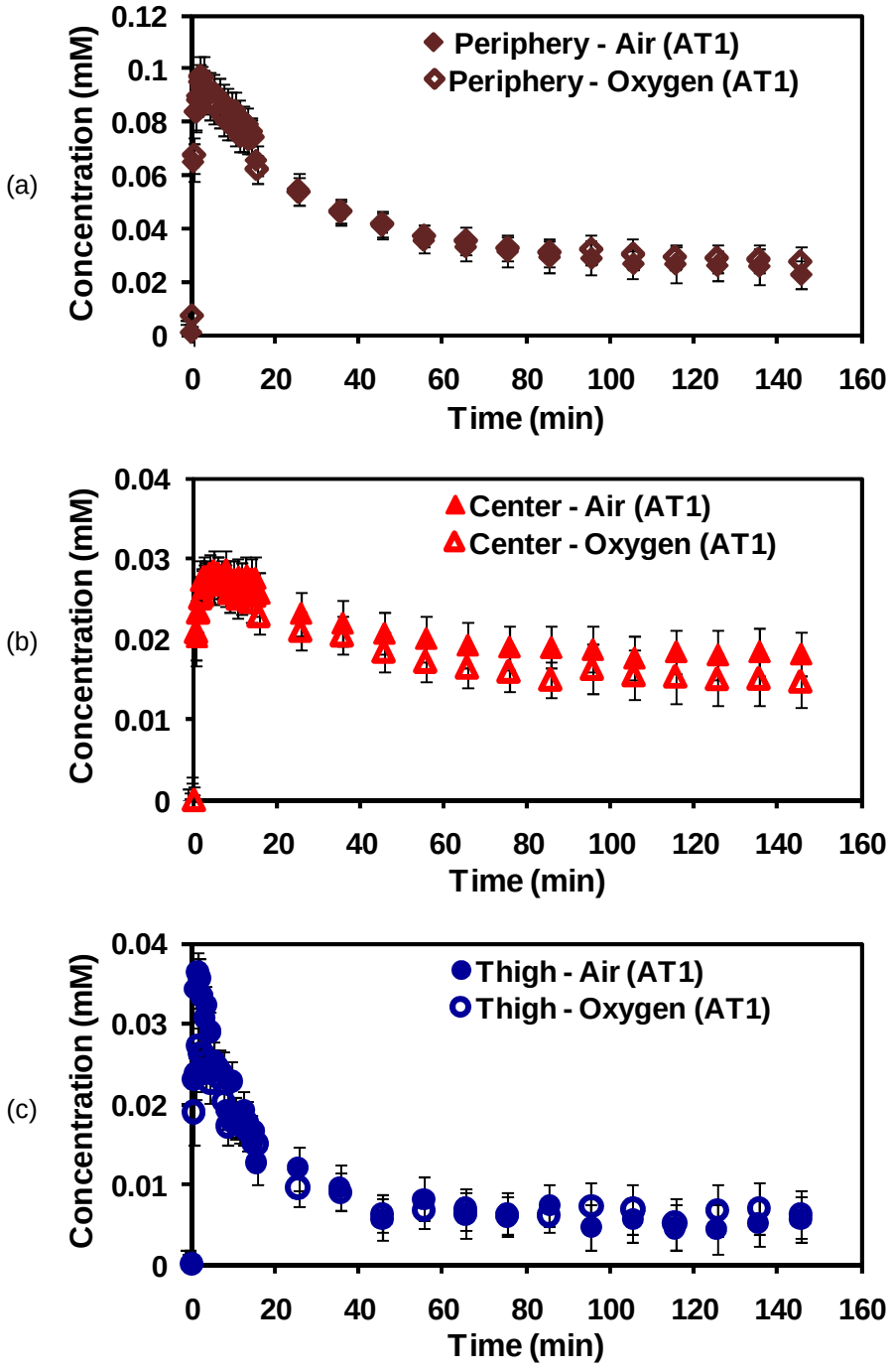

Figure 3.12 Kinetics of mean Gd concentration (n=4) for (a) peripheral and (b) central regions of ATI tumors along with (c) thighs in animals injected with GdDO3NI following air and oxygen breathing.

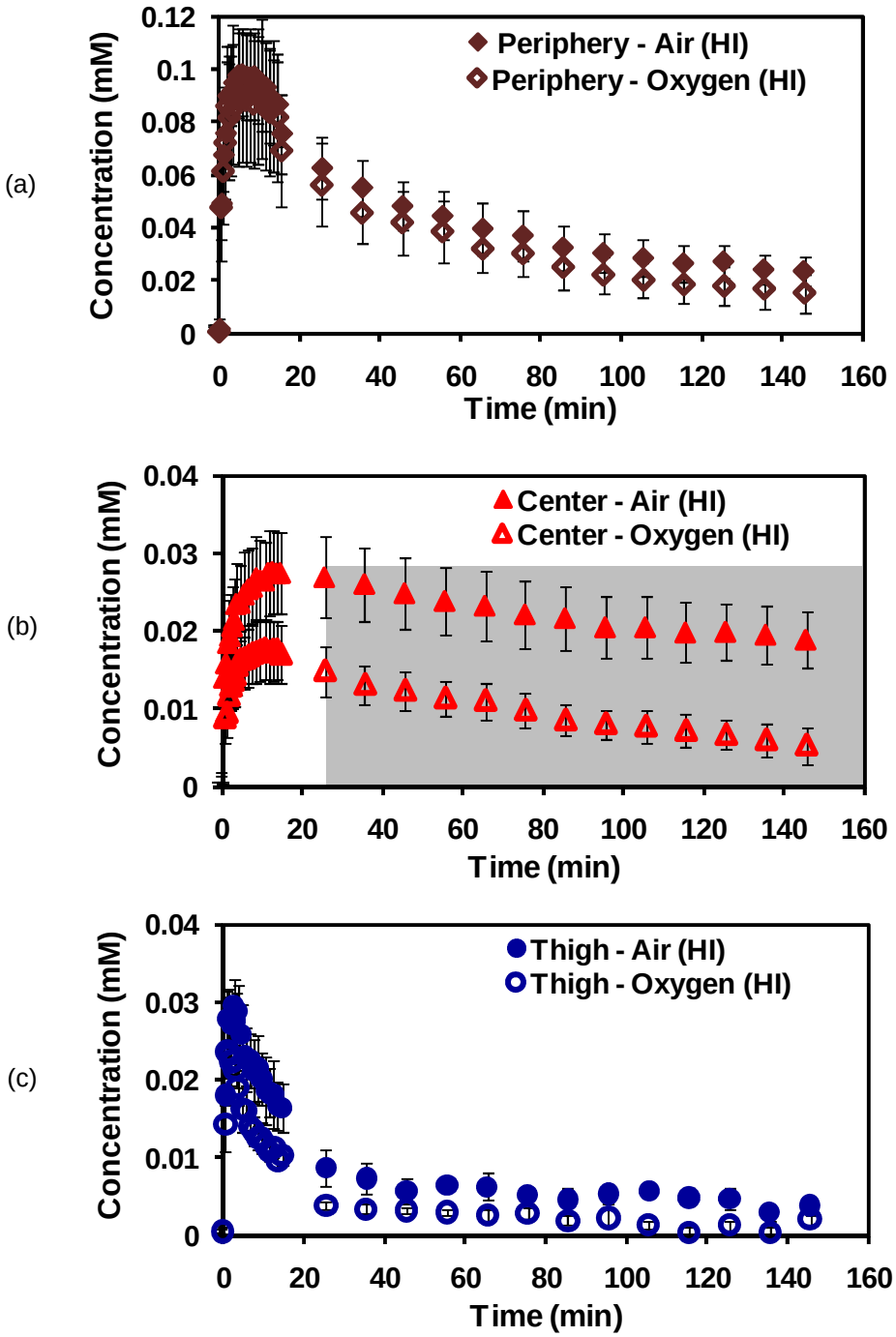

Figure 3.13 Kinetics of mean Gd concentration (n=4) for (a) peripheral and (b) central regions of HI tumors along with (c) thighs in animals injected with GdDO3NI following air and oxygen breathing. Region shaded in gray represents $p<0.0001$ after 2-way ANOVA with repeated measures followed by Bonferroni's multiple comparison test.

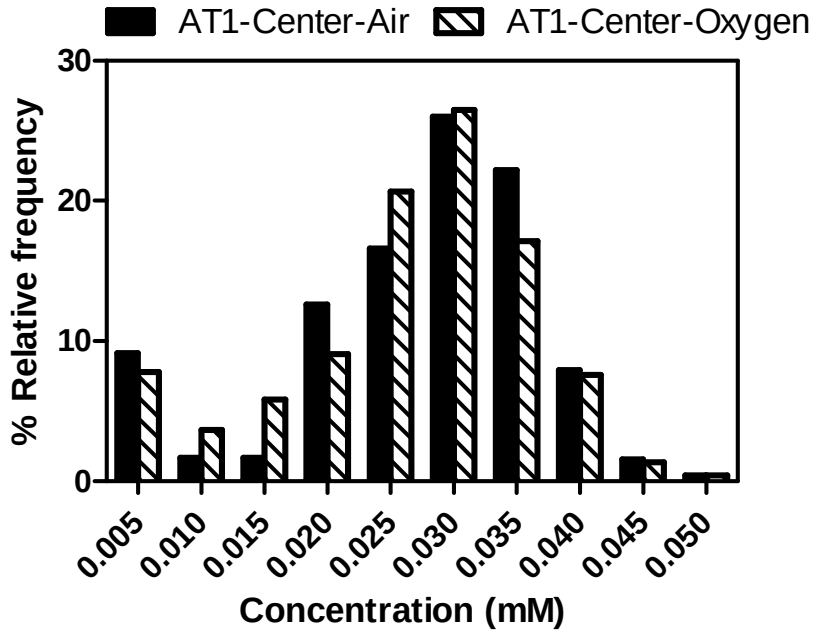

(a)

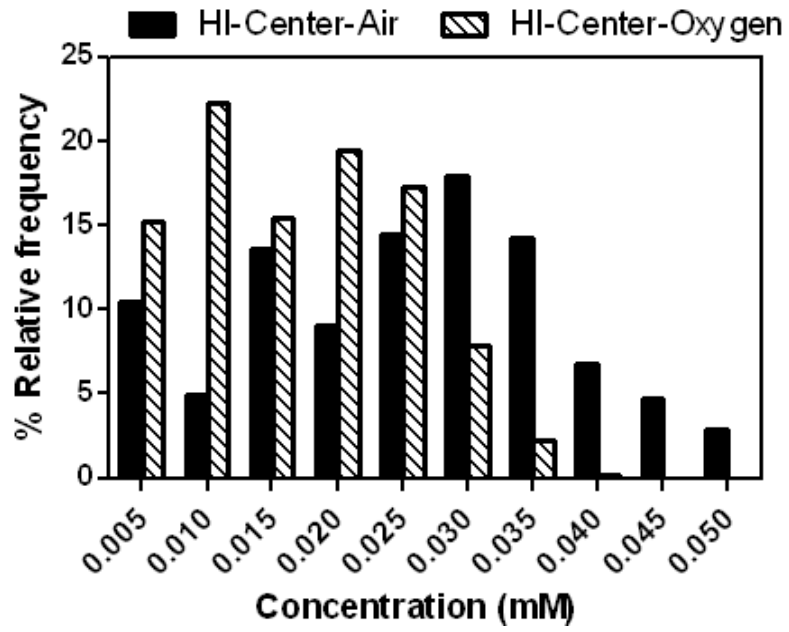

(b)

Figure 3.14 Histogram of the Gd concentration from central regions of (a) AT1 and (b) HI tumors in animals injected with GdDO3NI following air and oxygen breathing. HI tumors clearly showed a decrease in Gd concentration (left shift) following oxygen breathing where as AT1 tumors did not respond.

3.4.4 Ex vivo tumor sample analysis

3.4.4.1 Pimonidazole Staining for hypoxia

Following the visualization and quantification of hypoxia distribution in AT1 tumors by means of MR imaging, we further validated the existence of hypoxia by high-resolution microscopy using 'the gold standard' pimonidazole staining (Fig 3.15). After immunohistochemistry, the images were acquired at 10X magnification using a fluorescence microscope (DeltaVison RT, Applied Precision, Issaquah, WA) equipped with a CoolSNAP^{HQ} cooled charge-coupled device digital camera (Photometrics, Tuscon, AZ), a computer-controlled motorized stepping stage, and SoftWoRx 3.7 imaging software package (Applied Precision. Figure 3.15b shows the distribution of hypoxia after the individual microscopic images were stitched using SoftWoRx 3.7 software.

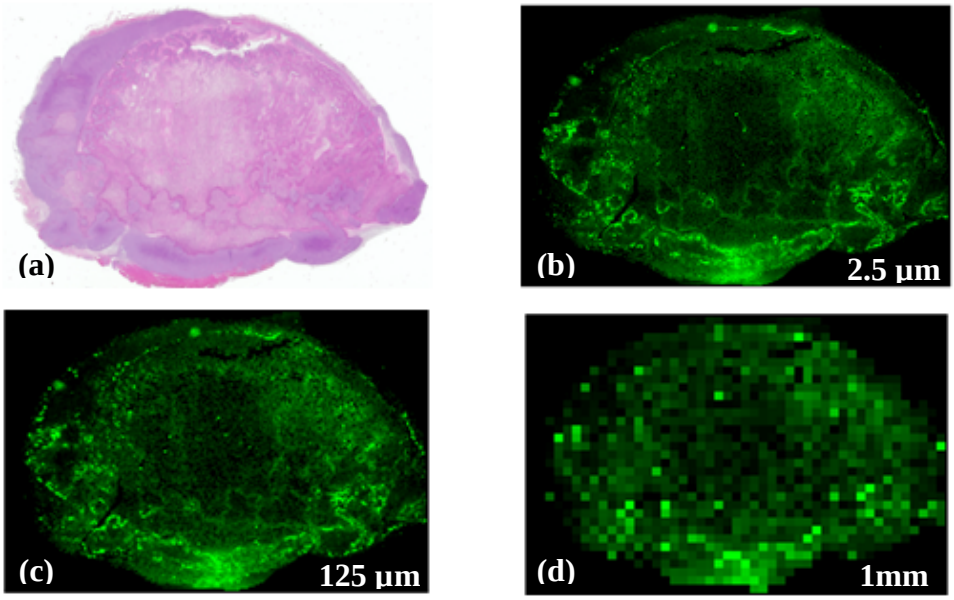

Figure 3.15 a) Shows the cellularity (H&E) and (b) hypoxia distribution by pimonidazole staining in an AT1 tumor section. The pimonidazole staining clearly showed extensive hypoxia in regions of the tumor. (c, d) show simulated lower resolution images of hypoxia distribution.

3.4.4.2 ICP-MS analysis for Gd quantification:

Inductively coupled plasma mass spectroscopy (ICP-MS) analysis of AT1 tumor sections (*ex vivo)* was performed to quantify the Gd^{3+} ion concentration. The tumor sections were cut to delineate the periphery and core following which the samples were sent for ICP-MS analysis. The concentration of gadolinium (Gd) (Fig 3.16) was significantly higher in the central tumor region of GdDO3NI injected animals (n=3) when compared to its periphery as well as tumor regions of GdDO3ABA injected animals (n=3). A ~ 50 fold higher retention of Gd was observed in central regions of tumors that were injected with GdDO3NI when compared to GdDO3ABA.

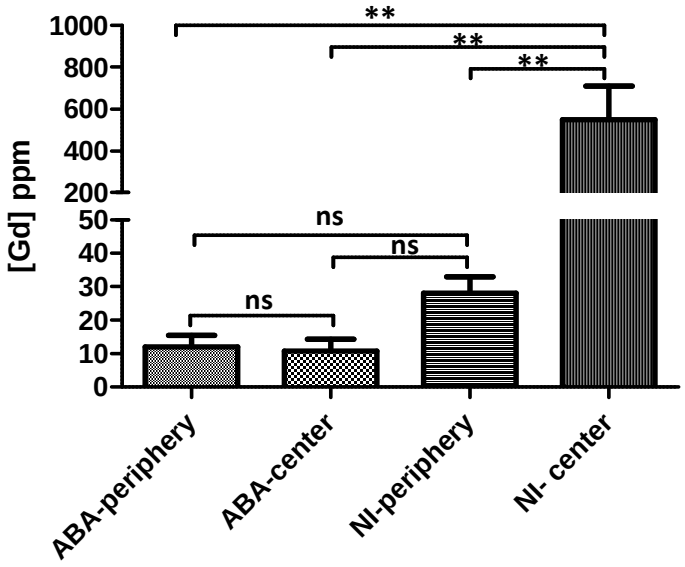

Figure 3.16 Inductively coupled plasma mass spectroscopy (ICP-MS) analysis of AT1 tumor sections *ex vivo*. The central or core regions of the AT1 tumors of animals injected with GdDO3NI agent showed enhanced retention of Gd^{3+} clearly validating GdDO3NI as hypoxia targeting agent. ** represents $p<0.05$ following 1-way ANOVA.

3.5 Discussion

The vital role of hypoxia in the development and malignant progression various cancers has been well studied. Hypoxia is also an important factor in determining the efficacy of radiotherapy, photodynamic therapy and some chemotherapies, and information related to hypoxic regions could be clinically important (11). Although it has been hoped that modulation of tumor oxygenation could be applied to enhance therapeutic efficacy, until now effective hypoxia imaging methods have been lacking in the clinic (10).

Our study tries to address this issue by evaluating a novel hypoxia targeting MR contrast agent GdDO3NI with respect to the following attributes, a) being a stable and effective reporter molecule of hypoxia, suitable for noninvasive *in vivo* studies and b) enable high-resolution ^{1}H MR imaging to show the heterogeneity of hypoxia distribution in solid tumors.

Gadolinium chelates of macrocyclic ligands such as 1,4,7,10-tetraazacyclododecane-1,4,7,10- tetraacetic acid (DOTA) are being widely used as contrast agents for clinical MRI (80) because of their high thermodynamic stability, kinetic inertness, and favorable relaxation properties. In addition, the coordination chemistry of these compounds has been well studied (81,82), allowing for the design of targeted probes for *in vivo* applications. Previously, radiolabeled lanthanide 2-nitroimidazole conjugates with DOTA derivatives were synthesized for imaging of hypoxia (83). Though these agents showed tumor localization, their ligands without the nitroimidazole moiety showed similar *in vivo* uptake. In further improvement of these approaches, here we report a novel gadolinium chelate (GdDOTA monoamide conjugate of 2-nitroimidazole, referred as GdDO3NI), as a magnetic resonance imaging (MRI) probe to detect hypoxia.

For both the agents, we characterized the longitudinal relaxivity (r_1) and observed a slightly higher relaxivity for GdDO3NI when compared to GdDO3ABA. Relaxivity refers to the relaxation enhancement of solvent protons by the given paramagnetic complex at 1 mM

concentration. This increase in observed relaxivity of GdDO3NI can be attributed to the elongation of the rotational correlation time (τ_R) due to the presence of the long pendant arm.

Since our main objective was to evaluate the hypoxia targeting capability of GdDO3NI, choice of *in vitro* (cells) and *in vivo* (tumor) models was of paramount importance. For *in vitro* Gd uptake studies, 9L rat glioma cells were used since have been extensively studied in the past as a hypoxia model for radiosensitivity studies under low oxygen conditions (84,85). From the ROI analysis of T_1 map (Fig 3.4b, c), we determined a ΔR_1 of 0.10 s^{-1} and 0.76 s^{-1} for samples incubated with GdDO3NI under normoxic and hypoxic conditions respectively, with respect to the negative control. Thus the hypoxic sample showed a ~8 fold higher Gd uptake compared to normoxic sample, clearly demonstrating the hypoxia-targeting ability of GdDO3NI.

Another main focus of this study was to determine the *in vivo* contrast agent kinetics as well as the ability to detect the spatial distribution of hypoxia in tumor models. In order to achieve this, we chose large (~3 c.c) Dunning R3327-AT1 prostate tumors which have been known to be extensively hypoxic (86), as our *in vivo* model. Also, Gd-DOTA-(n-butyl)monoamide, GdDO3ABA, was used as the 'control agent' without the nitroimidazole ring.

The observed signal intensities and consequently concentrations increased fastest in the well-perfused regions of tumors because of rapid contrast agent influx (Fig 3.8a). This was followed by fast wash-out, irrespective of the contrast agent (GdDO3NI or GdDO3ABA). In contrast, central regions, typically characterized by deficits in vascular supply, showed a delayed Gd uptake corresponding to a delay in signal build-up for both contrast agents (Fig 3.8b). But more interestingly, the wash-out kinetics were different for both contrast agents (Fig 3.9a, b). We attribute this statistically significant increase / retention of GdDO3NI concentration in the central regions of the tumor at late time points to the presence of hypoxia.

Pimonidazole staining of the excised AT1 tumor tissues confirmed the presence of extensive hypoxia throughout the central regions of the tumor (Fig 3.16b). Also, ICP-MS analysis of the AT1 tumor samples revalidated the presence of excess amounts of Gd only in

the central regions of GdDO3NI injected animals (Fig 3.16) as observed from the concentration maps. These cross validation studies prove that GdDO3NI was targeting hypoxic regions and could be used to image hypoxia at anatomical ^{1}H MR resolution.

On the basis of these results and with clinical translation in mind, we further validated the use of GdDO3NI as a noninvasive imaging assay for detecting changes in tumor hypoxia. This capability can have profound implications on cancer treatment as it is practiced today. It will allow us to observe positive (reduction of hypoxia) or no response in tumors following hyperoxic gas breathing. It will also help us better understand treatment- induced changes in tumor hypoxia.

To investigate the use of GdDO3NI in detecting changes in the hypoxic fraction of tumors, we chose two tumor lines (Dunning R3327-AT1 and HI) with known responses of hypoxia to oxygen breathing (41,86). Extensive studies using ^{19}F MR oximetry have shown that large AT1 and HI tumors (> 3 cc) are hypoxic while breathing air with mean (± SE) pO_2 values of 3.5 ± 1.5 torr and 12.7 ± 1.1 torr respectively. While HI tumors had shown a rapid response to oxygen breathing (mean pO_2 = 102 torr), AT1 tumors resisted modulation (86).

In AT1 tumors, we did not observe statistically significant differences in GdDO3NI concentration at late time points between air and oxygen breathing. The contrast kinetic profiles of periphery, center and thigh regions were very similar (Fig 3.12). In the HI tumors, no significant difference of GdDO3NI uptake in peripheral and thigh regions was observed at late time points between air and oxygen breathing (Fig 3.13a, c). But we observed a significant decrease in GdDO3NI uptake in the central regions of the tumor when the animals breathed oxygen as compared to air (Fig 3.13b, Fig 3.14b). These observations are in accordance with the previously published data (16).

Another important need in the clinical setting for hypoxia imaging is the resolution of detection. It is important to realize the specific resolution of each hypoxia imaging modality or technique. Figure 3.15 demonstrates the differences in perceived hypoxia distribution when

moving from actual microscopic resolution (Fig 3.15b, 2.5 μm) to anatomical ^{1}H MR resolution (Fig 3.15c, 125 μm) towards ^{1}H MR oximetry or pre-clinical PET imaging resolution (Fig 3.15d, 1 mm). Irrespective of the imaging technique or modality, every value that is obtained is an ensemble average of the microscopic variations present in the measured voxel. The current clinical hypoxia imaging resolution reported using PET imaging of ^{18}F-MISO is ~ 5 mm X 5 mm where as the new pre-clinical PET scanners can achieve 1 mm X 1 mm resolution (87,88). Our contrast agent enables hypoxia detection at anatomical ^{1}H MR resolution of 125 – 200 μm, which is a 20 fold improvement in resolution when compared to the current clinical standard of PET imaging using ^{18}F-MISO and more importantly it is closer to microscopy visually. Also this technique represents a 5 fold improvement in resolution when compared to quantitative PISTOL technique discussed in Chapter 2.

In this study, we have successfully evaluated a novel Gd-based nitroimidazole as a T_1 contrast agent (GdDO3NI) for MR imaging of hypoxia. We demonstrated its hypoxia targeting ability, *in vitro*, using cells incubated under hypoxic conditions. We also determined the contrast agent kinetics of GdDO3NI and its ability to detect changes in tumor oxygenation following oxygen intervention.

CHAPTER 4

A NOVEL CLASS OF S-GAL® ANALOGS AS ^{1}H MR GENE REPORTER MOLECULES FOR *IN VIVO* DETECTION OF β -GALACTOSIDASE

4.1 Abstract

Extensive implementation of gene therapy as a cancer therapeutic strategy has been hampered by difficulties in quantitatively assessing the success of gene transfection and longevity of gene expression. Therefore development of noninvasive reporter techniques based on appropriate molecules and imaging modalities may help to assay gene expression. I have evaluated a series of S-Gal® analogs as novel ^{1}H MR *lacZ* gene-reporter molecules *in vitro* and have identified the molecule, C3-GD as an optimal agent for *in vivo* studies. In the presence of ferric ions (Fe^{3+}), the molecule is cleaved by β-galactosidase encoded in the *lacZ* gene, and forms a paramagnetic iron chelate. This causes a pronounced T_1 & T_2 shortening in MR images. Athymic nude mice (n = 6) implanted subcutaneous with MCF7 (wild type) and *lacZ* transfected MCF7 tumors were used to perform the study. Following baseline imaging, 25µl of a solution with 15 mM C3-GD and 5 mM ferric ammonium citrate (FAC) in water was injected intra-tumorally using a fine needle into each tumor. T_1 & T_2 weighted images were acquired at 1 and 2 hours post injection. MCF7 - *lacZ* tumors showed small but statistically significant changes in T_1 & T_2 values after 2 hours whereas the MCF7 (wild type) tumors showed minimal changes.

4.2 Introduction

Reporter genes are frequently used to assess regulation and transfection of genes in biological pathways. One of the major challenges in the field of gene therapy has been the lack of methods to quantitatively assess the success of gene transfection and the longevity

of gene expression (89). Hence, development of noninvasive reporter techniques based on appropriate molecules and imaging modalities may help to assay gene expression.

Some of the popular reporter genes are those that generate β-galactosidase (β -gal), β-glucuronidase, firefly luciferase, fluorescent proteins (e.g. green fluorescent protein), transferrin and ferritin (90,91). The *lacZ* gene encoding β-gal has been the most extensively used reporter gene with applications ranging from basic science to translational and clinical trials for assaying protein expressions and interactions (92,93).

There are various commercially available reagents (substrates) in regular use to detect *lacZ* gene expression by colorimetric stains and assays, some of which are nitrophenyl-β-D-galactopyranoside (generates yellow color), 4-chloro-3-bromoindole-galactose (X-Gal®, generates a blue stain) and 3,4-cyclohexenoesculetin-β-galactopyranoside (S-Gal® - generates a black stain). These assays have been used extensively for *ex vivo* and/or *in vitro* applications (94-96) with a few reported *in vivo* studies. In recent years, development of novel reporter molecules and techniques for noninvasive *in vivo* detection of *lacZ* transgene expression (β-gal activity) have been reported and they range from optical (97-99), radionuclide (100,101) to MR imaging [^{1}H (102-104) and/or ^{19}F (105,106)]. Lately, ^{19}F NMR spectroscopy based approaches have gained renewed interest due to the advantage of having large observable chemical shifts between substrate and product, which report on the enzymatic reaction kinetics (53,107). The advantages and potential disadvantages of various ^{19}F NMR substrates to assay β-gal activity for *in vivo* imaging have been reviewed recently (108).

In a recently published study, the laboratory of prognostic radiology (LPR) the ability to detect β-gal activity in *lacZ* transfected breast cancer cells (MCF7) *in vitro* and *in vivo* using the commercially available colorimetric substrate; sodium 3,4-cyclohexenoesculetin-β-galactopyranoside (S-Gal® sodium salt- Fig. 4.1) by ^{1}H MRI (104).

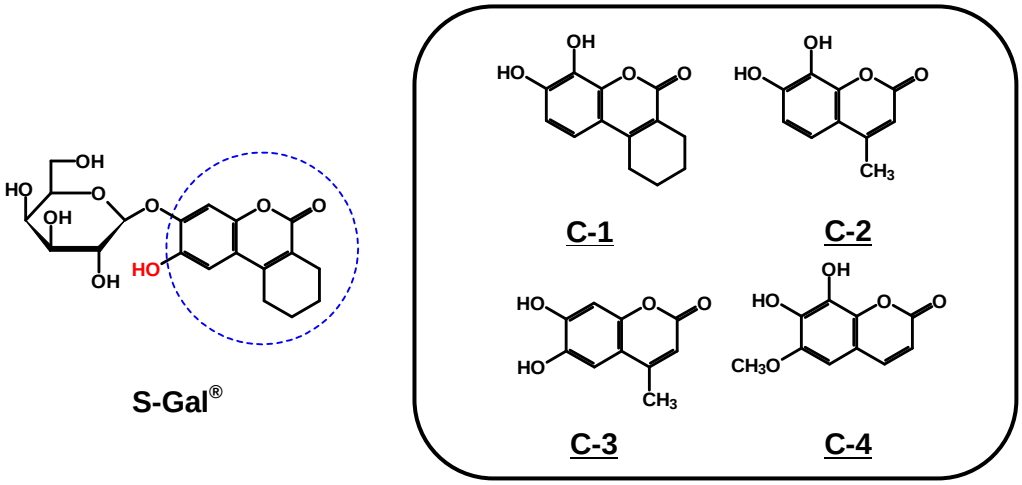

Figure 4.1 Structure of commercial colorimetric *lacZ* gene-reporter, S-gal®. C1 - 4 are analogs of the product of cleavage of S-Gal® by β-galactosidase.

I now report the development and evaluation of a series of S-Gal® analogs as ^{1}H MR gene reporter molecules for detection of β-galactosidase. I also demonstrate the feasibility of *in vivo* imaging using very low dose of the reporter molecule C3 – GD.

4.3 Materials and Methods

3,4-Cyclohexenoesculetin β-D-galactopyranoside (Fig. 4.1), S-Gal® sodium salt, and ferric ammonium citrate (FAC) were purchased from Sigma-Aldrich (St. Louis, MO). The evaluated reporter molecules (Fig 4.2) were synthesized by Dr. Jian-xin Yu and a brief description of the synthesis can be found elsewhere (109). All MR studies were performed on a Varian INOVA 4.7T horizontal-bore MR system equipped with actively shielded gradients.

4.3.1 Detection of β-gal activity in vitro

For *in vitro* measurements, each reporter molecule solution (15 mM in de-ionized water, 40 µl) was mixed with ferric ammonium citrate (5 mM, 40 µl) in 2% agar solution with or without β-gal (5 units, E801A, Sigma-Aldrich, St. Louis, MO) and placed in 4X4 cut section of a 96 well plate. The prepared phantom was left on a heating block maintained at 37 ℃ for 30 mins for enzymatic reaction to stabilize. T_1 and T_2 maps of the phantom were acquired by using

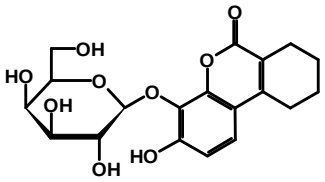

C1 - MGD

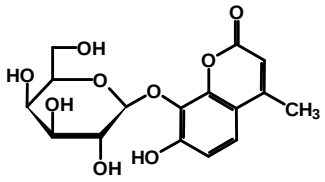

C2 - MGD

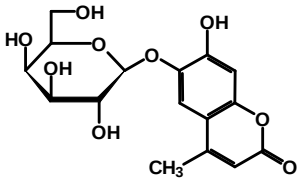

C3- MGD

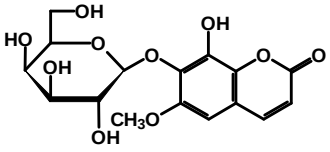

C4 - MGD

(a)

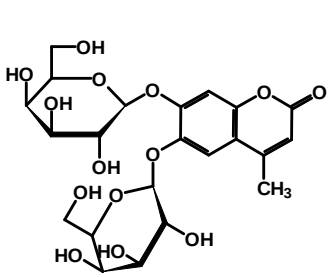

C1 - GD

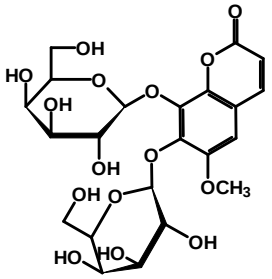

C2 - GD

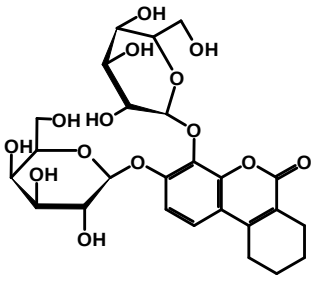

C3 - GD

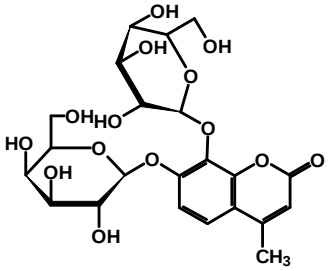

C4 - GD

(b)

Figure 4.2 Structures of novel *lacZ* gene-reporter molecules evaluated in this study. (a) C1 - 4 MGD are mono-galactopyranosides; (b) while C1 - 4 GD are di-galactopyranosides. GD compounds are more soluble in water.

a standard spin echo sequence, using a 3 cm solenoid coil (home-built) at 37 ℃. MRI parameters used were: FOV 40 mm X 40 mm, matrix size 128X128, slice thickness 1mm, T_1 mapping: TE = 12 ms and varying TR (0.2 – 6 s), T_2 mapping: varying TE (0.012 – 0.2 s) and TR = 6 s.

4.3.2 In vivo detection of β-gal activity in MCF7 and MCF7-lacZ tumors

Based on better water solubility and enhanced contrast seen during *in vitro* experiments, C3 - GD was chosen for *in vivo* studies. MCF7 (wild type -1.5X 10^6) and MCF7-*lacZ* (2X10^6) cells were implanted subcutaneously in the flanks of athymic nude mice (N = 6) on contralateral sides. The *lacZ* gene was stably transfected into MCF7 cells by Dr. Li Liu. MRI studies were performed when the tumor size reached 0.75 cm^3. Mice were anesthetized with 1.5% isoflurane in air and were placed in a Litzcage volume coil (Doty Scientific Inc, Columbia, SC) for MRI. Animal body temperature was maintained at 37 ℃ using a circulating warm water pad. Baseline T_1 and T_2 maps of tumor containing slices were acquired by using a spin echo sequence. MRI parameters used were: FOV 100 mm X 50 mm, matrix size 256X128, slice thickness 1 mm, T_1 mapping: TE = 12 ms and varying TR (0.2 – 6 s), T_2 mapping: varying TE (0.012 – 0.2 s) and TR = 6 s. Following baseline imaging, the mouse was removed from the scanner and 25µl of a solution with 15 mM C3-GD and 5 mM FAC in water was injected intra-tumorally using a fine needle into each tumor. After repositioning the mouse carefully, T_1 and T_2 maps were acquired at 1 and 2 hours post injection.

4.3.3 Histology

For postmortem verification of β-gal, the tumors were excised after the MRI study and stored in OCT. 5 µm cut sections of the tissue were then fixed with 4% formaldehyde 0.2% glutaraldehyde in PBS for 10 min, and washed three times in PBS (pH 7.4). These sections were further stained with β-gal-staining solution [1 mg/mL 5-bromo-4-chloro- 3-indolyl- β-D-

galactopyranoside (X-gal), 2mM $MgCl_2$, 5mM $K_4Fe(CN)_6$, and 5mM $K_3Fe(CN)_6$] for 45 minutes at room temperature and then counter stained with Nuclear fast (Poly Scientific, Bay Shore, NY, USA), to reveal β-gal activity and nuclei locations respectively

4.4 Results

4.4.1 Evaluation of reporter molecules in vitro:

In agar gel phantoms, the addition of 5 units of β - gal enzyme to the agent + FAC solution showed a signal enhancement in T_1 wt images and signal loss in T_2 wt images. Figure 4.3 shows the T_1 and T_2 maps of the evaluated reporter molecules + FAC in the absence or presence of β - gal enzyme. Of the evaluated molecules, C3 - GD, C2 - MGD and C3 - MGD showed a change (decrease) in T_1 of 1.12 s, 1.24 s and 1.17 s respectively, which is higher than 1.03 s observed using S-Gal® (Table 4.1, Fig. 4.4). Similarly, C3 - GD and C3 - MGD showed a decrease in T_2 of 0.045 s and 0.095 s respectively which is significantly higher than 0.023 s observed using S-Gal® (Table 4.1, Fig. 4.4). The T_1 and T_2 values decreased significantly for most molecules but C3 - GD was used for further *in vivo* studies due to better water solubility than C3 - MGD.

Table 4.1 Longitudinal and transverse relaxation times (T_1 & T_2 respectively) of the synthesized gene reporter molecules in the absence or presence of β-galactosidase. T_1 and T_2 values of the agents C3 - GD and C3 - MGD decreased significantly in the presence of the enzyme.

Agent	**T_1 (s)**			**T_2 (s)**		
	w/o β-gal	**w/ β-gal**	**ΔR_1 (s^{-1})**	**w/o β-gal**	**w/ β-gal**	**ΔR_2(s^{-1})**
C1-GD	1.76 ± 0.13	1.11 ± 0.09	0.33	0.12 ± 0.03	0.12 ± 0.04	-0.84
C2-GD	1.81 ± 0.15	1.39 ± 0.09	0.17	0.12 ± 0.05	0.11 ± 0.03	0.76
C3-GD	1.83 ± 0.15	0.72 ± 0.12	0.85	0.11 ± 0.04	0.07 ± 0.01	5.97
C4-GD	1.85 ± 0.15	1.18 ± 0.06	0.31	0.13 ± 0.05	0.11 ± 0.04	1.67
S-Gal®	2.07 ± 0.12	1.04 ± 0.05	0.48	0.09 ± 0.03	0.07 ± 0. 01	3.41
C1-MGD	1.79 ± 0.28	1.46 ± 0.19	0.127	0.13 ± 0.04	0. 09 ± 0.03	3.42
C2-MGD	1.83 ± 0.13	0.58 ± 0.05	1.17	0.12 ± 0.05	0.10 ± 0.03	1.72
C3-MGD	1.68 ± 0.12	0.51 ± 0.13	1.36	0.13 ± 0.05	0.03 ± 0.01	22.09
C4-MGD	1.78 ± 0.09	0.84 ± 0.05	0.62	0.13 ± 0.05	0.13 ± 0.03	0.09

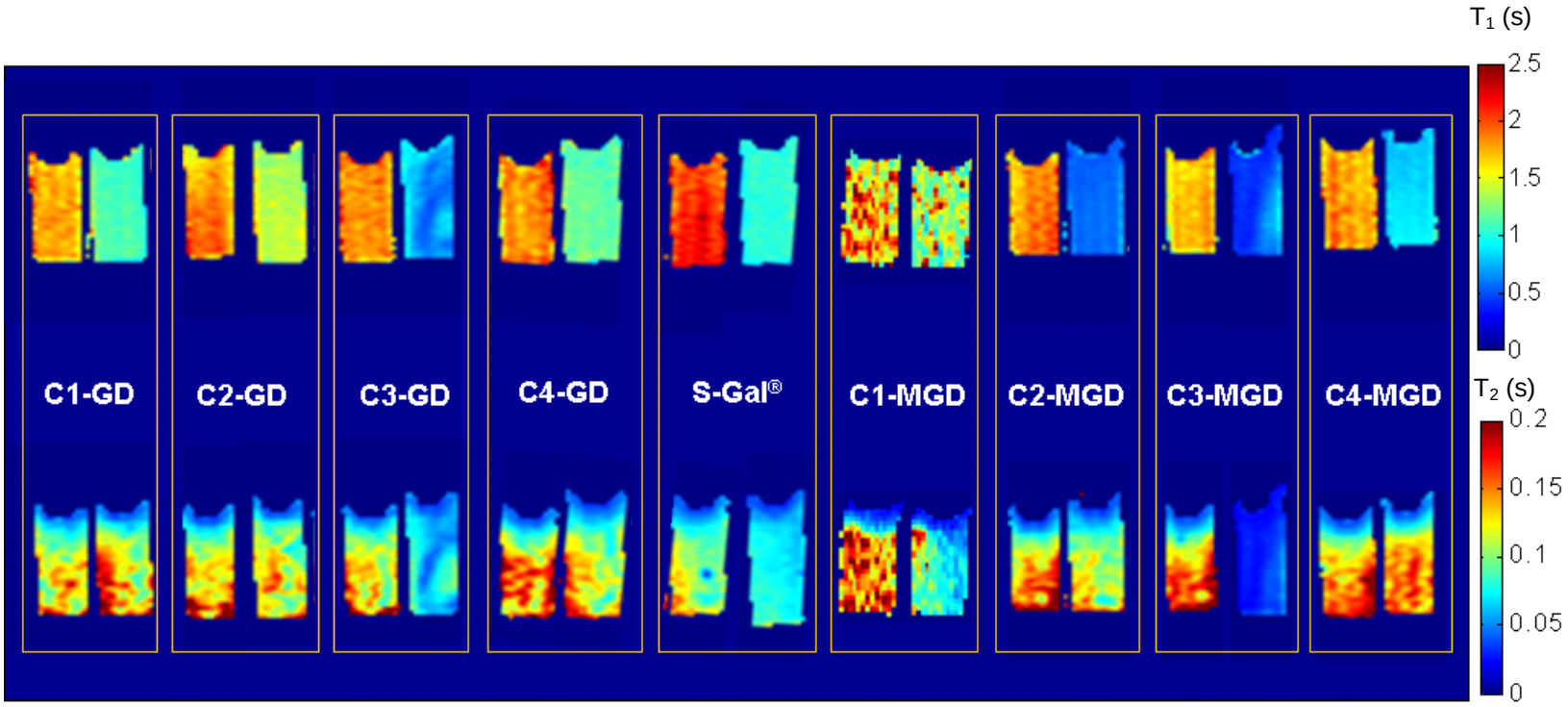

Figure 4.3 *In vitro lacZ* gene reporter activity of various analogs of S-gal ®. The figure shows the T_1 (top row) and T_2 (bottom row) maps. Each sample contained 15 mM Agent + 5 mM FAC in agarose without (left) or with (right sample in each yellow box) 5 units of β-gal enzyme. Pronounced T_1 and T_2 effects are seen for the agents C3 - GD and C3 - MGD.

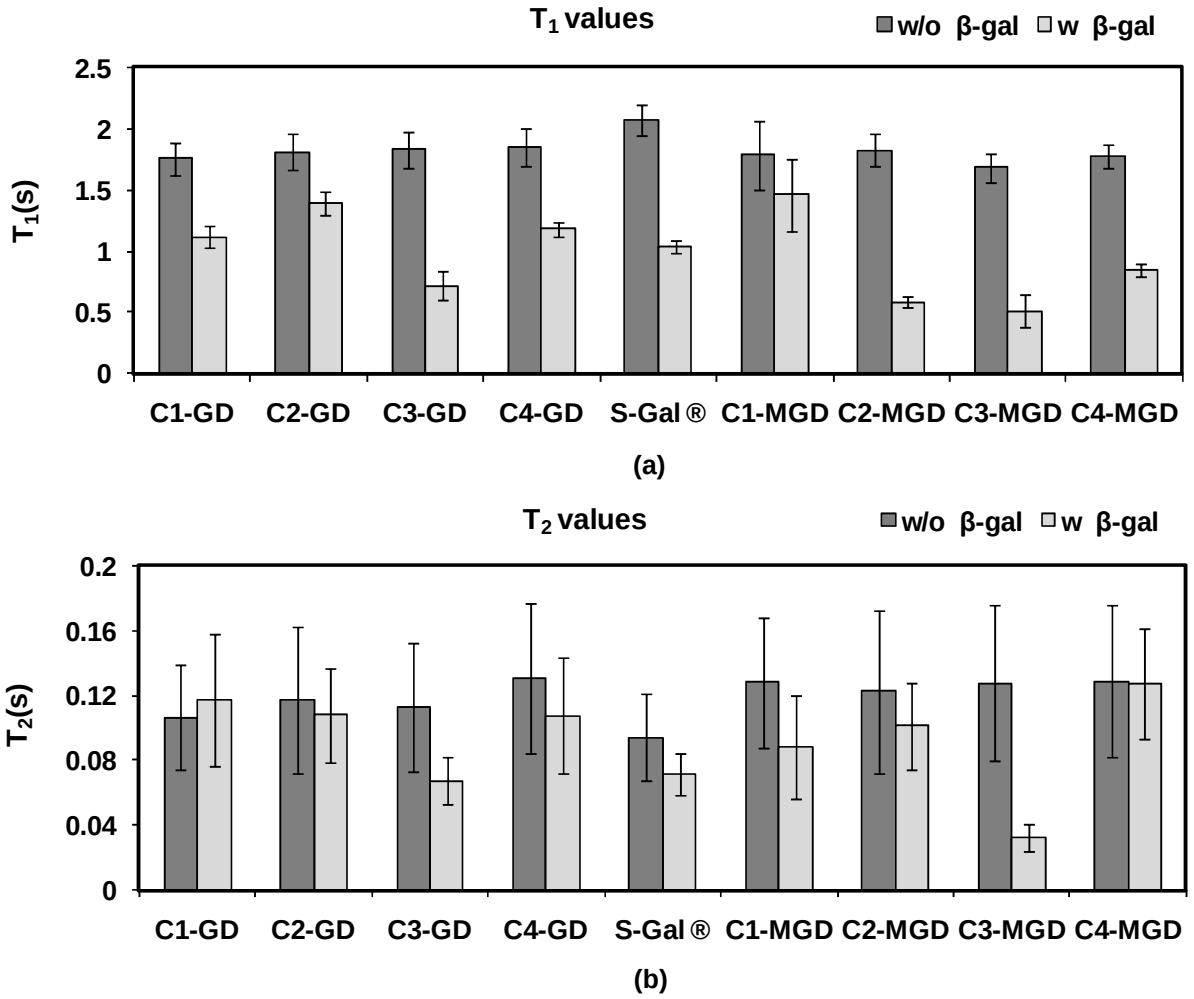

Figure 4.4 (a) T_1 & (b) T_2 values of the synthesized gene reporter molecules in the absence or presence of β-galactosidase. C3 -GD and C3- MGD showed the largest decrease in T_1 and T_2 values compared to S-gal ® in the presence of the enzyme.

4.4.2 Evaluation of reporter molecules in vivo:

T_1 and T_2 maps of athymic nude mice bearing wild type (WT) and *lacZ*-transfected MCF7 tumors were acquired before and after the injection of C3-GD (15 mM) + FAC (5 mM) solution (25 µl vol.). For data analysis (per animal), only the tumor slice with the reporter molecule injection (Fig 4.5) was identified based on T_1 maps (for both WT and *lacZ* tumors) and T_2 maps (for *lacZ* tumors only). Tumor voxels from the injected slice of all animals were pooled with respect to imaging time point (baseline, 1hr and 2 hrs post injection) and statistical analysis was performed.

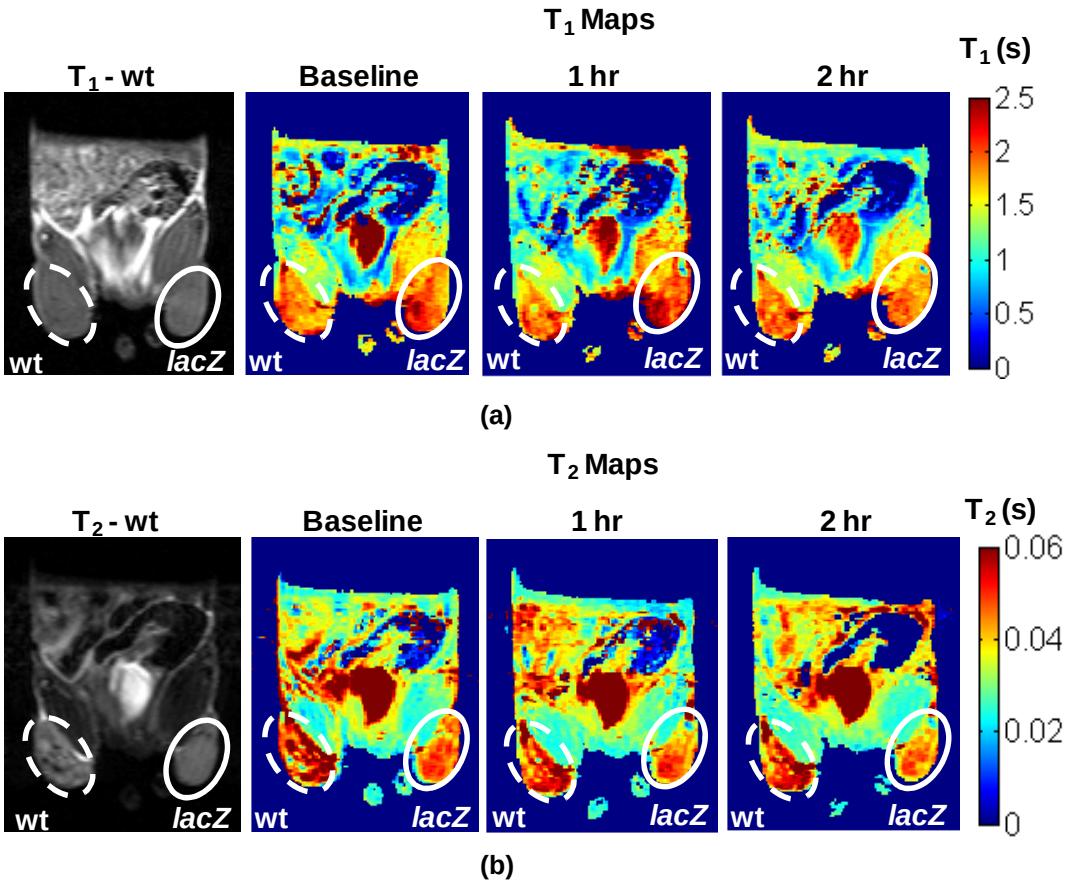

Figure 4.5 *In vivo lacZ* gene reporter activity of C3 - GD. A representative MRI slice of a nude mouse with wild type MCF7 tumor (left - dotted) and *lacZ* transfected MCF7 tumor (right - solid) are shown. a) T_1 - wt images (top row) and T_1 maps (bottom row) and b) T_2 - wt images (top row) and T_2 maps (bottom row).

4.4.2.1 T_1 analysis

Due to very small injected dose, T_1-weighted images showed small hyper intensities which were better perceived from the decrease in T_1 values as seen in the T_1 maps of representative tumor slices (Fig. 4.5 a). There was a small but significant difference between mean baseline T_1 (1.84 ± 0.28 s; WT (n=6) vs. 1.88 ± 0.21 s; *lacZ* (n=6); $p<0.0001$; unpaired t-test) of the two tumor types. Following injection of reporter molecule solution (C3-GD+FAC), T_1 decreased significantly in WT tumors (T_1 = 1.72 ± 0.29 s, $p< 0.0001$) after 1 hr but recovered back by the end of 2 hrs (T_1 = 1.97 ± 0.35 s, $p< 0.0001$). In *lacZ* tumors, T_1 decreased statistically significantly by the end of 1 hr (T_1 = 1.69 ± 0.32 s, $p< 0.0001$) and continued to decrease till 2 hr (T_1 = 1.63 ± 0.25 s, $p< 0.0001$).The statistical analysis was performed using 1 way ANOVA followed by Bonferroni's multiple comparison test.

4.4.2.2 T_2 analysis

ROI analysis of the same slices(as in T_1 analysis) on T_2 maps showed large decrease in T_2 values at later time points for MCF7- *lacZ* tumors when compared to baseline (Fig. 4.5 b). There was a significant difference in the baseline T_2 value of WT and *lacZ* transfected tumors (T_2 = 56 ± 16 ms (WT) vs. T_2 = 51 ± 8 ms (*lacZ*); $p< 0.0001$; unpaired t-test). Following administration of reporter molecule solution (C3-GD+FAC), T_2 decreased statistically significantly in WT tumors (T_2 = 51 ± 16 ms; $p<0.0001$) at 1 hr but returned back to baseline value (T_2 = 57 ± 18 ms; $p>0.05$) at 2 hr. In *lacZ* tumors, T_2 decreased statistically significantly by the end of 1 hr (T_2 = 44 ± 10, $p< 0.0001$) and remained unchanged till 2 hr (T_2 = 44 ± 9, $p< 0.0001$).

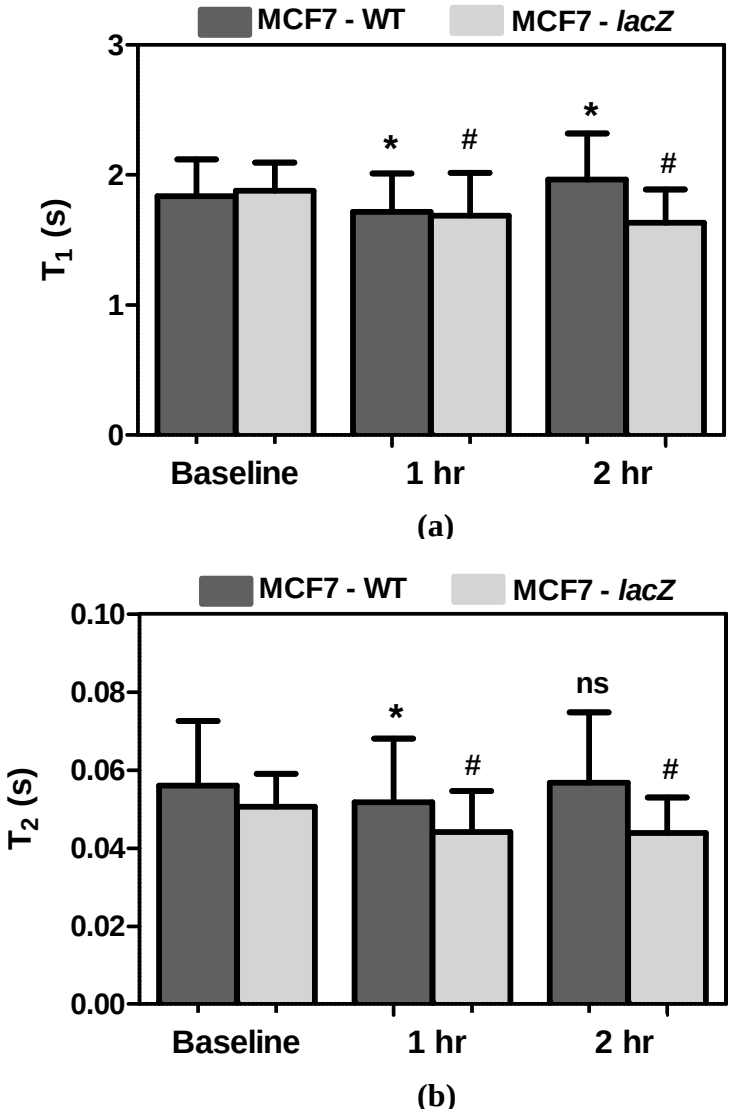

Figure 4.6 (a) Mean T_1 and (b) T_2 values from pooled voxels for all tumors (n=6) pre, 1hr post and 2hr post injection of 25 µl of C3 – GD plus FAC solution. The two time-points post injection were compared to the values pre injection for statistical significance of changes using 1 way ANOVA. * and # represent $p<0.001$ for wild type and *lacZ* tumors respectively.

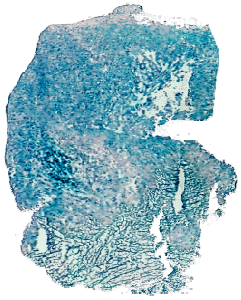

(a)

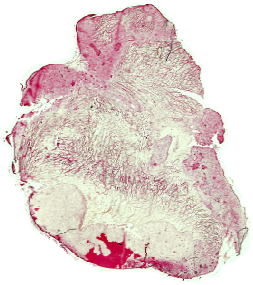

(b)

Figure 4.7 X-gal and Nuclear fast staining of slices (full mount) from the tumors obtained post mortem: (a) MCF7- *lacZ* and (b) MCF7 - WT. Intense blue stain showed β-gal activity for the MCF7 *lacZ* tumor section only.

4.5 Discussion

I have successfully evaluated analogs of the product of cleavage of S-Gal® by β-galactosidase as ^{1}H MR gene reporter molecules by *in vitro* imaging. The synthesized mono- and di- galactopyranosides (MGD and GD respectively) showed differential enhancements. In the presence of ferric ions (Fe^{3+} from FAC), the reporter molecules are cleaved by β-galactosidase encoded in the *lacZ* gene. This aglycone product readily forms a paramagnetic iron chelate causing a pronounced T_1 & T_2 shortening in MR images.

Escherichia coli (*lacZ*) β-gal catalyses the hydrolysis of β-*D*-galactopyranosides by cleavage of the C-O bond between *D*-galactose and the aglycones. The substrate specificities and activities are highly dependent on their various aglycones (110). The detection of *lacZ* using S-Gal® (104,111) in the presence of Fe^{3+} showed that the MRI contrast is produced by the formation of 3,4-cyclohexenoesculetin (aglycone) / Fe (Fe^{3+} from FAC) complex *in situ* (112).

Traditionally iron - based MRI contrast agents are designed to have coordinatively saturated Fe^{3+}-complexes since iron, a redox- active metal may cause oxidative damage *in vivo*. These design considerations eliminate the possibility of inner-sphere coordination of water molecules in Fe^{3+}-based MRI contrast agents. Intermediate between inner-sphere and outer-sphere interactions with water is the second-sphere binding of water molecules to sites within a Fe^{3+}-complexed ligand. This binding of water allows close approach of the bulk water protons to the paramagnetic Fe^{3+} ion, while simultaneously allowing coordinative saturation at the metal center (32,113,114).

Since there exists a thorough understanding on the biochemistry of Fe^{3+} (115), the design of second-sphere MRI contrast agents as organ- or disease-specific diagnostic pharmaceuticals, has raised much interest (113,116-118). Also, literature is available describing the design and evaluation of series of siderophores that contain catechol binding groups (catecholate ligands) to coordinate Fe^{3+} (116-118). These ligands are of particular interest in the development of Fe^{3+}-based second-sphere MRI contrast agents because they have the potential to maintain coordinative saturation while providing the opportunity for H_2O to H-bond to the catecholate O atoms of the Fe-O-R (R=catecholate ligands) linkages. Therefore, Dr. Yu used the coumarin-based catecholate aglycones with modifications on the positions of donor groups, chelator skeleton and substituents, which generally govern Fe-complex formation, stability, specificity and chelation efficacy (119), for synthesizing a novel class of gene-reporter molecules.

From our initial experiments, I observed that the synthesized coumarin-based mono-galactopyranosides showed lower water solubility. In the past, carbohydrates with multiple hydroxyl groups were routinely used to reduce barriers against cellular uptake and improve solubility (120). Therefore, Dr. Yu conjugated an additional β-*D*-galactopyranosyl unit to the mono-galactopyranosides, for improving their hydrophilicity and then to promote their solubility and cellular internalization.

As seen from Fig 4.3, the mono-galactopyranosides always showed better T_1 and T_2 contrast when compared to their associated di-galactopyranosides (For ex: C2 – MGD showed better T_1 & T_2 shortening than C2-GD). This can be attributed to the fact that β-gal enzyme has to act twice on a di-galactopyranoside before liberating the aglycone to form the iron chelate. Also, the presence of additional galactose moieties in the GD reporter molecules had no influence on the T_1 and T_2 of the agent + FAC mixture in the absence of enzyme as seen from the similar T_1 and T_2 values of MGD and GD reporter molecules (Fig 4.4 a and b). For the optimal agent (15 mM) and FAC (5 mM) concentration, C3 –MGD and C3 - GD demonstrated pronounced T_1 & T_2 shortening in the presence of 5 units of β-gal but owing to better water solubility which is preferred for *in vivo* applications, C3-GD was used for *in vivo* studies.

Following intra-tumoral injection of the agent + FAC solution, in wild type tumors, I observed a decrease in T_1 & T_2 values from baseline to 1hr time point which returned to baseline values by 2 hr time point. This initial decrease in T_1 & T_2 values can be attributed to the free ferric ions which eventually get cleared out. In the *lacZ* transfected tumors, formation of iron complexes due to the chelation of aglycones in the presence of ferric ions caused a rapid shortening of T_1 & T_2 values when compared to baseline values.

The X-gal and Nuclear fast staining of tumor slices obtained following the MRI studies clearly showed an intense blue stain representing β-gal activity only in the MCF7 *lacZ* tumor but not in the MCF7 wildtype tumor (Fig 4.7). This further supports our MRI findings.

Table 4.2 Values of T_1 and T_2 obtained from ROI analysis of *in vivo* data (n = 6). MCF7-*lacZ* tumors show a significant decrease in T_1 & T_2 values at 2 hr post injection when compared to baseline.

	MCF7- *lacZ*	**MCF7 - WT**	**MCF7 - *lacZ***	**MCF7 - WT**
	T_1 (s)	**T_1 (s)**	**T_2 (ms)**	**T_2 (ms)**
Baseline	1.88 ± 0.22	1.84 ± 0.28	51 ± 8	56 ± 16
1 hr post injection	1.69 ± 0.33	1.72 ± 0.29	44 ± 10	51 ± 16
2 hr post injection	1.63 ± 0.25	1.97 ± 0.35	44 ± 9	57 ± 18
1 way ANOVA p-value	B – 1hr ******* B – 2hr ******* 1hr – 2 hr *******	B – 1hr *** B – 2hr *** 1hr – 2 hr ***	B – 1hr *** B – 2hr *** 1hr – 2 hr **ns**	B – 1hr *** B – 2hr **ns** 1hr – 2 hr ***
% Change (B – 2 hr)	-13.3	7	-13.7	1.7

A limitation of the present approach is our inability to directly assess substrate cleavage and product formation in real time. A novel approach to overcome this problem has been recently proposed by the use of dual $^{19}F/^{1}H$ MR *lacZ* gene reporter molecules (121). In these molecules, a fluorine atom was introduced into the iron-chelating aglycones of β-*D*-galactopyranosides, which when activated by β-gal, released an aglycone that displayed a distinct ^{19}F chemical shift with respect to the substrate.

In conclusion, I evaluated 8 novel *lacZ* responsive Fe^{3+}-based MR gene reporter molecules. The synthesized mono and di-β-*D*-galactopyranosides demonstrated differential T_1 & T_2 relaxation characteristics in the presence of Fe^{3+} and show great promise as ^{1}H MRI *lacZ* gene reporters. Intra-tumoral injection of 25µl of the reporter molecule solution (15 mM C3-GD and 5 mM FAC in de-ionized water) showed small but statistically significant decrease in the T_1 & T_2 values of MCF7 - *lacZ* tumors after 2 hours whereas the MCF7 (wild type) tumors showed minimal changes.

CHAPTER 5

CONCLUSIONS AND RECOMMENDATIONS

Since the tumor microenvironment plays a crucial role in carcinogenesis and metastasis, it represents a crucial target not only for cancer therapy but also for preventive strategies. Therefore, accurate noninvasive imaging of confounding factors like measurements of pO_2, pH, perfusion, enzymatic and metabolic characteristics in the tumor microenvironment are critical. This dissertation research focuses on the evaluation of novel probes to interrogate the tumor microenvironment, specifically hypoxia and gene expression using proton (^1H) magnetic resonance imaging (MRI).

Previously, we have demonstrated the use of hexamethyldisiloxane as a ^1H MR pO_2 reporter molecule and determined tumor pO_2 values following direct intratumoral (IT) injections. This approach enables the interrogation of any region of interest in the tumor immediately following the injection. Even though IT injection has the advantage of delivering less dose of the reporter molecule, this technique is only limited to probing tumors that are accessible. In chapter 2, I have demonstrated the feasibility of preparing HMDSO loaded nanoemulsions for use as nanoprobes for quantitative ^1H MR oximetry and characterized their sensitivity to changes in pO_2. The similarity in calibration curves between the prepared HMDSO based nanoemulsions containing <5% surfactant and neat HMDSO clearly indicate that the emulsification process didn't hinder the exchange of O_2 between pO_2 nanosensor and surrounding tissue (or solution). The nanoemulsion prepared using 40% v/v HMDSO-5% v/v HS-15 - 55% v/v de-ionized water was identified as optimal formulation based on its calibration curve and particle size data. Further I measured the temperature dependence of the calibration constants A' and B' for this formulation and determined them to be similar to neat HMDSO (42). Based on the temperature-

dependent calibration curve, the calculated error in pO_2 at 37 ^oC was 1.0 torr/^oC, compared to 0.8 torr/^oC for neat HMDSO, when actual pO_2 value was 5 torr.

Given that hypoxic tumors are more resistant to certain therapies, it becomes important to assess tumor oxygenation and its modulation with respect to adjuvant interventions as part of therapeutic planning. Using the HMDSO based nanoemulsion I have shown the ability to measure dynamic changes in tissue pO_2, following normobaric and hyperbaric oxygen breathing interventions. Additionally, I determined the calibration curves of various linear and cyclic siloxanes (of different chain lengths) and investigated their utility as pO_2 sensing reporter molecules. The wide range of boiling points offered by these siloxanes could enable diverse applications of ^1H MR oximetry. This study also helps in determining the choice of siloxane (smaller dynamic range of T_1's across the pO_2 range) for applications requiring faster time resolution.

Since the ultimate goal of this project is to perform tumor oximetry following the systemic delivery of these nanoemulsions, future work should involve the determination of *in vivo* biocompatibility and pharmacokinetics of the injected nanoemulsions. Pharmacokinetics could be determined either by an MR based approach (preferred) or by tagging a fluorescent dye to the nanoemulsion and detection using a fluorescence imager. Current efforts in our lab include the preparation of smaller and more stable nanoemulsions using different surfactant / co-surfactant mixtures. The main limitation of the PISTOL method is that it is limited to the determination of quantitative pO_2 values in a single slice. Implementation of spectral spatial pulses in the excitation scheme of PISTOL could enable multi- slice or even 3D quantitative oximetry. Another drawback of the PISTOL technique is that the attainable spatial resolution will always be limited by the detectability of the HMDSO signal.

In chapter 3, I have successfully evaluated a novel Gd-based nitroimidazole (GdDO3NI) as a T_1 contrast agent for MR imaging of hypoxia. I demonstrated its hypoxia targeting ability, *in vitro*, using cells incubated under hypoxic conditions. The *in vivo* contrast agent kinetics of

GdDO3NI and a control agent GdDO3ABA, in AT1 tumors were determined. The signal enhancement and concentration profiles clearly demonstrated the selective uptake of GdDO3NI agent in the central (poorly perfused and potentially hypoxic) regions of the tumors. I further confirmed the existence of hypoxia in AT1 tumors by pimonidazole staining. The elemental Gd concentration in segmented tumor samples was performed by ICP-MS to cross-validate the MR findings. In accordance with the MRI findings, the ICP-MS Gd concentration in central regions of the tumor samples from animals injected with GdDO3NI was higher than the periphery or GdDO3ABA samples. Using GdDO3NI, I have further shown the ability to detect changes in tumor oxygenation following oxygen intervention in HI tumors. The Gd concentration uptake in central regions of HI tumors was significantly lower when the animals breathed oxygen when compared to air. This observation is in agreement with the previously published studies on response to oxygen breathing of HI tumor using ^{19}F MR oximetry by our research group.

In this study, I have shown the ability of GdDO3NI to detect hypoxia at anatomical MRI resolution using 2D multi-slice data. In the future, characterization of hypoxic threshold based on tumor to blood or tumor to thigh Gd concentration ratios is warranted. Further improvement could be the use of 3D- gradient echo based approaches for imaging the heterogeneous distribution of hypoxia in 3 dimensions. Also studying the binding efficiency of GdDO3NI at various levels of hypoxia, *in vitro*, will help in better understanding the mechanism and quantification of data, potential leading to quantitative oximetry. Since GdDO3NI shows great promise as a hypoxia targeting agent, a further one-to-one comparison study using ^{18}F-MISO-PET in preclinical setting could enhance its potential clinically translatability.

In Chapter 4, I have successfully evaluated analogs of the product of cleavage of S-Gal® by β-galactosidase as ^{1}H MR gene reporter molecules. The synthesized mono- and di-galactopyranosides (MGD and GD respectively) showed differential enhancements in *in vitro* MR imaging of agarose phantoms. The enzyme β-galactosidase encoded by the *lacZ* gene cleaves the galactose moiety from the reporter molecule, forming an aglycone product. This

product in the presence of ferric ions (Fe^{3+} from FAC), readily forms a paramagnetic iron chelate causing a pronounced T_1 & T_2 shortening in MR images. Owing to better water solubility and contrast effects, C3-GD was determined to be the best molecule out of the series of molecules evaluated and was used for animal studies. For *in vivo* studies, I used athymic nude mice implanted subcutaneously with MCF7 (wild type) and *lacZ* transfected MCF7 tumors. Intra-tumoral injection of a very small volume of the reporter molecule solution showed significant changes in the T_1 & T_2 values of MCF7 - *lacZ* tumors after 2 hours whereas the MCF7 (wild type) tumors showed minimal changes. Immunohistology for β-gal expression clearly demonstrated the presence of *lacZ* transfection only in the MCF7- *lacZ* tumors further supporting the MRI findings. The focus of future gene reporter molecule research should be in developing agents that utilize endogenous iron to develop contrast. Also, one can envision applications of the evaluated reporter molecules with suitable cleavage domains for the detection of other endogenous or transfected gene expression with very high sensitivity.

APPENDIX A

LIST OF PUBLICATIONS AND CONFERENCE ABSTRACTS

Peer reviewed publications

1) **Praveen K. Gulaka,** Ujjawal Rastogi, Madalyn McKay, Ralph P. Mason, Vikram D. Kodibagkar, "Hexamethyldisiloxane based emulsions for imaging tissue oxygenation using ^{1}H MRI", 2011: NMR in Biomedicine (epub ahead of print DOI:10.1002/nbm.1678).

2) Ralph P. Mason, Dawen Zhao, Jesus Pacheco-Torres, Weina Cui, Vikram D. Kodibagkar, **Praveen K. Gulaka**, Guiyang Hao, Phil Thorpe, Eric W. Hahn, Peter Peschke. "Multimodality imaging of hypoxia in preclinical settings", Q J Nucl Med Mol Imaging, 54(3), 259-280 (2010).

3) You-Fu Zhou, **Praveen Gulaka**, Jian Zhou, Ming Xiao, Dongsheng Xu, Jer-Tsong Hsieh, Vikram D. Kodibagkar, and Xiankai Sun. "Preparation and Evaluation of a Radioisotope-Incorporated Iron Oxide Core/Au Shell Nanoplatform for Dual Modality Imaging". J. Biomed. Nanotechnol. 4, 474–481 (2008).

4) Vikram D. Kodibagkar, Xianghui Wang, Jesus Pacheco-Torres, **Praveen K. Gulaka**, Ralph P. Mason. "Proton Imaging of Siloxanes to map Tissue Oxygenation Levels (PISTOL): a tool for quantitative tissue oximetry". NMR Biomed. 21,899-907 (2008).

Papers in preparation

1) **Praveen K. Gulaka**, Federico Q. Rojas-Quijano, Zoltan Kovacs, A. Dean Sherry, Vikram D. Kodibagkar. "In vitro and in vivo evaluation of 2-nitroimidazole Gd - chelate as a hypoxia targeting MRI T1 contrast agent".

2) **Praveen K. Gulaka**, Jian-xin Yu, Ralph P. Mason, Vikram D. Kodibagkar. " A novel class of S-Gal® analogs as ^{1}H MR gene reporter molecules for *in vivo* detection of β-galactosidase".

3) Sairam Geethanath**, Praveen K. Gulaka**, Vikram D. Kodibagkar. "Acceleration of conventional data acquisition in dynamic contrast enhancement: comparing keyhole approaches with compressive sensing".

4) Jian-xin Yu, **Praveen K. Gulaka**, Li Liu, Ralph P. Mason, Vikram D. Kodibagkar. "Novel Fe-based ^{1}H MRI gene reporter molecules".

5) Federico A. Rojas-Quijano, Gyula Tircsó, Enikő Tircsóné Benyó, Zsolt Baranyai, Huan Tran Hoang, Ferenc K. Kálmán, **Praveen K. Gulaka**, Vikram Kodibagkar, Silvio Aime, Zoltán Kovács and A. Dean Sherry. "Synthesis and characterization of a hypoxia sensitive probe for MRI Imaging".

Conference abstracts

1) **Praveen K. Gulaka**, Federico Rojas-Quijano, Zoltan Kovacs, Ralph P. Mason, A. Dean Sherry, Vikram D. Kodibagkar, "Imaging hypoxia using a nitroimidazole based T_1 MR contrast agent", Proc. of International Society for Magnetic Resonance in Medicine; Montreal, Canada; May 2011.

2) **Praveen K. Gulaka,** Edmond Richer, Vikram D. Kodibagkar, "Monitoring tissue response to hyperbaric oxygen intervention using PISTOL", Proc. of International Society for Magnetic Resonance in Medicine; Montreal, Canada; May 2011.

3) **Praveen K. Gulaka**, Zoltan Kovacs, Ralph P. Mason, A. Dean Sherry, Vikram D. Kodibagkar, "Differential PARACEST and conventional dynamic contrast enhancement upon treatment in rat breast tumors", Proc. of Southern Biomedical Engineering Conference (SBEC), Arlington, TX - April 2011.

4) **Praveen K. Gulaka**, Jyothi Menon, Tina Darjazanie, Vikram D. Kodibagkar, "Siloxane based dual modality MRI/ Fluorescence nanoprobes for molecular imaging", Proc. of Southern Biomedical Engineering Conference (SBEC), Arlington,TX - April 2011.

5) Vikram D. Kodibagkar, **Praveen K. Gulaka**, Federico Rojas-Quijano, Zoltan Kovacs, Ralph P. Mason, A. Dean Sherry, "In vitro and in vivo evaluation of GdDO3NI as a hypoxia targeting MRI contrast agent", Proc. of International Society for Magnetic Resonance in Medicine; Stockholm, Sweden; May 2010. **Poster award winner (2nd prize) in molecular imaging.**

6) **Praveen K. Gulaka**, Vikram D. Kodibagkar, "New bullets for PISTOL: linear and cyclic reporter molecules for ^{1}H MR oximetry", Proc. of International Society for Magnetic Resonance in Medicine; Stockholm, Sweden; May 2010.

7) **Praveen K. Gulaka**, Vikram D. Kodibagkar, Jian-xin Yu, Ralph P. Mason, "A novel class of S-Gal® analogs as ^{1}H MRI LacZ gene reporter molecules", Proc. of International Society for Magnetic Resonance in Medicine; Stockholm, Sweden; May 2010.

8) **Praveen K. Gulaka**, Tina Darjazanie, Ralph P. Mason, Vikram D. Kodibagkar, "Quantitative ^{1}H MR tissue oximetry using Hexamethyldisiloxane emulsions", Frontiers of biomedical Imaging Science; Vanderbilt University, Nashville, TN; June 2009.

9) **Praveen K. Gulaka**, Tina Darjazanie, Ralph P. Mason, Vikram D. Kodibagkar, "Mapping tissue oxygen tension using ^{1}H MR based nanoemulsions", Proc. of International Society for Magnetic Resonance in Medicine; Honolulu, HI; April 2009.

10) **Praveen K. Gulaka**, Vikram D. Kodibagkar, Jian-XinYu, Ralph P. Mason, “In vivo studies of a novel Fe-based ^{1}H MRI LacZ gene reporter molecule: C3-GD”, American Association for Cancer Research; Denver, CO; April 2009

11) Vikram D. Kodibagkar, **Praveen K. Gulaka**, Zoltan Kovacs, Eul-Hyun Suh, A. Dean Sherry, Ralph P. Mason, “Differential Dynamic Contrast Enhancement of an Albumin-Binding PARACEST Agent in Rat Breast Tumors”, WMIC-World Molecular Imaging Congress, Nice, France, September 2008.

12) **Praveen K. Gulaka**, Xianghui Wang, Ralph P. Mason, Vikram D. Kodibagkar, “Synthesis and Characterization of Nanoprobes for ^{1}H MR Oximetry”, WMIC-World Molecular Imaging Congress, Nice, France, September 2008.

13) Vikram D. Kodibagkar, **Praveen K. Gulaka**, Elena Vinogradov, Zoltan Kovacs, Eul-Hyun Suh, and Dean Sherry, “A novel macromolecular contrast agent based on paramagnetic chemical exchange saturation transfer (PARACEST) for breast cancer studies”, DoD Era of Hope Breast Cancer Research Program, Washington DC, 2008.

14) Vikram D. Kodibagkar, **Praveen K. Gulaka**, Xianghui Wang, Ralph P. Mason, “Nanoprobes for 1H MRI based oximetry ”. Proc. of International Society of Magnetic resonance in Medicine, Toronto, Canada, May 2008.

APPENDIX B

CALIBRATION CURVES OF NEAT HMDSO AND NANOEMULSION (40% HMDSO, 5% HS-15) FROM 0 TORR (N_2) TO 760 TORR (100% O_2)

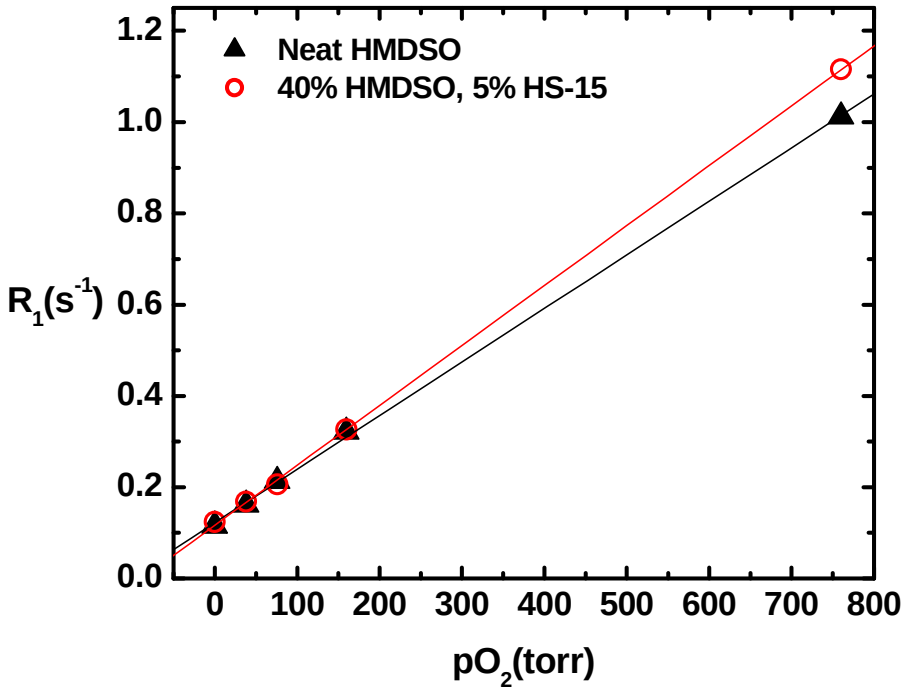

Figure B.1 Calibration curve (R_1 and pO_2) of neat HMDSO and nanoemulsion (40% HMDSO, 5% HS-15). Linear fit to data at 37 ℃ from 0-760 torr yields R_1 [s^{-1}] = 0.1162 + 0.0013* pO_2 [torr] (R^2>0.999) and R_1 [s^{-1}] = 0.1217 + 0.0012* pO_2 [torr] (R^2>0.999) for neat HMDSO and nanoemulsion, respectively. The neat HMDSO calibration data was acquired by Dr. Kodibagkar whereas nanoemulsion calibration data was acquired by Ujjawal Rastogi.

REFERENCES

1. Weinberg RA. The biology of cancer. London: Garland Science; 2006. 864 p.

2. Mbeunkui F, Johann DJ, Jr. Cancer and the tumor microenvironment: a review of an essential relationship. Cancer Chemother Pharmacol 2009;63(4):571-582.

3. Wike-Hooley JL, Haveman J, Reinhold HS. The relavanve of tumor pH to the treatment of malignant disease. Radiother Oncol 1984;2:343-366.

4. Rofstad EK, Mathiesen B, Kindem K, Galappathi K. Acidic extracellular pH promotes experimental metastasis of human melanoma cells in athymic nude mice. Cancer Res 2006;66(13):6699-6707.

5. van Sluis R, Bhujwalla Z, Raghunand N, Ballesteros P, Alvarez J, Cerdan S, Galons J, Gillies R. In vivo imaging of extracellular pH using 1H MRSI. Magn Reson Med 1999;41 743-750.

6. Folkman J. The vascularization of tumors. Sci Am 1976;234(5):58-64, 70-53.

7. Konerding MA, Malkusch W, Klapthor B, van Ackern C, Fait E, Hill SA, Parkins C, Chaplin DJ, Presta M, Denekamp J. Evidence for characteristic vascular patterns in solid tumours: quantitative studies using corrosion casts. Br J Cancer 1999;80(5-6):724-732.

8. Vaupel P, Kallinowski F, Okunieff P. Blood flow, oxygen and nutrient supply, and metabolic microenvironment of human tumors: a review. Cancer Res 1989;49(23):6449-6465.

9. Horsman MR. Measurement of tumor oxygenation. Int J Radiat Oncol Biol Phys 1998;42(4):701-704.

10. Tatum JL, Kelloff GJ, Gillies RJ, Arbeit JM, Brown JM, Chao KS, Chapman JD, Eckelman WC, Fyles AW, Giaccia AJ, Hill RP, Koch CJ, Krishna MC, Krohn KA, Lewis JS, Mason RP, Melillo G, Padhani AR, Powis G, Rajendran JG, Reba R, Robinson SP, Semenza GL, Swartz HM, Vaupel P, Yang D, Croft B, Hoffman J, Liu G, Stone H, Sullivan D. Hypoxia: importance in tumor biology, noninvasive measurement by imaging, and value of its measurement in the management of cancer therapy. Int J Radiat Biol 2006;82(10):699-757.

11. Vaupel P, Mayer A. Hypoxia in cancer: significance and impact on clinical outcome. Cancer Metastasis Rev 2007;26(2):225-239.

12. Gray LH, Conger AD, Ebert M, Hornsey S, Scott OC. The concentration of oxygen dissolved in tissues at the time of irradiation as a factor in radiotherapy. Br J Radiol 1953;26(312):638-648.

13. Denny WA. The role of hypoxia-activated prodrugs in cancer therapy. Lancet Oncology 2000;1(1):25-29.

14. Payen E, Bettan M, Henri A, Tomkiewitcz E, Houque A, Kuzniak I, Zuber J, Scherman D, & Beuzard Y. Oxygen tension and a pharmacological switch in the regulation of transgene expression for gene therapy. J Gene Med 2001;3:498-504.

15. Rofstad EK. Microenvironment-induced cancer metastasis. Int J Radiat Biol 2000;76(5):589-605.

16. Mason RP, Zhao D, Pacheco-Torres J, Cui W, Kodibagkar VD, Gulaka PK, Hao G, Thorpe P, Hahn EW, Peschke P. Multimodality imaging of hypoxia in preclinical settings. Q J Nucl Med Mol Imaging 2010;54(3):259-280.

17. Zhao D, Jiang L, Mason RP. Measuring changes in tumor oxygenation. Methods Enzymol 2004;386:378-418.

18. Griffiths JR, & Robinson SP. The OxyLite: a fibreoptic oxygen sensor. British Journal of Radiology 1999;72:627-630.

19. Takahashi E, Takano T, Nomura Y, Okano S, Nakajima O, Sato M. In vivo oxygen imaging using green fluorescent protein. Am J Physiol Cell Physiol 2006;291:C781-787.

20. Bussink J, Kaanders JH, Strik AM, Vojnovic B, & van der Kogel AJ. Optical sensor-based oxygen tension measurements correspond with hypoxia marker binding in three human tumor xenograft lines. Radiation Research 2000;154:547-555.

21. Xia M, Kodibagkar V, Liu H, Mason RP. Tumour oxygen dynamics measured simultaneously by near-infrared spectroscopy and 19F magnetic resonance imaging in rats. Physics in Medicine & Biology 2006;51(1):45-60.

22. Li L, Yu JM, Xing LG, Yang GR, Sun XD, Xu J, Zhu H, & Yue JB. Hypoxic imaging with 99mTc-HL91 single photon emission computed tomography in advanced nonsmall cell lung cancer. Chin Med J (Engl) 2006;119:1477-1480.

23. Lewis JS, McCarthy DW, McCarthy TJ, Fujibayashi Y, & Welch MJ. Evaluation of 64Cu-ATSM invitro and in vivo in a hypoxic tumor model. J Nucl Med 1999;40:177-183.

24. Mannan RH, Somayaji VV, Lee J, Mercer JR, Chapman JD, & Wiebe LI. Radioiodinated 1- (5-iodo-5-deoxy-beta-D-arabinofuranosyl)-2-nitroimidazole(iodoazomycin arabinoside: IAZA): a novel marker of tissue hypoxia. J Nucl Med 1991;32:1764-1770.

25. Baudelet C, & Gallez B. How does blood oxygen level-dependent (BOLD) contrast correlate with oxygen partial pressure (pO2) inside tumors? Magn Reson Med 2002;48:980-986.

26. Gallez B, Baudelet C, & Jordan BF. Assessment of tumor oxygenation by electron paramagnetic resonance:principles and applications. NMR Biomed 2004;17:240-262.

27. Mason RP. Non-invasive physiology: 19F NMR of perfluorocarbons. Artificial Cells, Blood Substitutes, and Immobilization Biotechnology 1994;22(4):1141-1153.

28. Hunjan S, Zhao D, Constantinescu A, Hahn EW, Antich PP, Mason RP. Tumor oximetry: demonstration of an enhanced dynamic mapping procedure using fluorine-19 echo planar magnetic resonance imaging in the Dunning prostate R3327-AT1 rat tumor. Int J Radiat Oncol Biol Phys 2001;49(4):1097-1108.

29. Krohn KA, Link JM, Mason RP. Molecular imaging of hypoxia. J Nucl Med 2008;49 Suppl 2:129S-148S.

30. Rasey JS, Grunbaum Z, Magee S, Nelson NJ, Olive PL, Durand RE, Krohn KA. Characterization of radiolabeled fluoromisonidazole as a probe for hypoxic cells. Radiat Res 1987;111(2):292-304.

31. Procissi D, Claus F, Burgman P, Koziorowski J, Chapman JD, Thakur SB, Matei C, Ling CC, Koutcher JA. In vivo 19F magnetic resonance spectroscopy and chemical shift imaging of tri-fluoro-nitroimidazole as a potential hypoxia reporter in solid tumors. Clin Cancer Res 2007;13(12):3738-3747.

32. Lauffer RB. Paramagnetic Metal-Complexes as Water Proton Relaxation Agents for Nmr Imaging - Theory and Design. Chem Rev 1987;87(5):901-927.

33. Villaraza AJL, Bumb A, Brechbiel MW. Macromolecules, Dendrimers, and Nanomaterials in Magnetic Resonance Imaging: The Interplay between Size, Function, and Pharmacokinetics. Chem Rev 2010;110(5):2921-2959.

34. Runge VM, Clanton JA, Lukehart CM, Partain CL, James AE, Jr. Paramagnetic agents for contrast-enhanced NMR imaging: a review. AJR Am J Roentgenol 1983;141(6):1209-1215.

35. Kodibagkar VD, Wang X, Mason RP. Physical principles of quantitative nuclear magnetic resonance oximetry. Front Biosci 2008;13:1371-1384.

36. Zhao D, Constantinescu A, Jiang L, Hahn EW, Mason RP. Prognostic radiology: quantitative assessment of tumor oxygen dynamics by MRI. American journal of clinical oncology : the official publication of the American Radium Society 2001;24(5):462-466.

37. Bourke VA, Zhao D, Gilio J, Chang CH, Jiang L, Hahn EW, Mason RP. Correlation of radiation response with tumor oxygenation in the Dunning prostate R3327-AT1 tumor. Int J Radiat Oncol Biol Phys 2007;67(4):1179-1186.

38. Mason RP, Rodbumrung W, Antich PP. Hexafluorobenzene: a sensitive 19F NMR indicator of tumor oxygenation. NMR in Biomedicine 1996;9(3):125-134.

39. Zhao D, Constantinescu A, Chang CH, Hahn EW, Mason RP. Correlation of tumor oxygen dynamics with radiation response of the dunning prostate R3327-HI tumor. Radiat Res 2003;159(5):621-631.

40. Zhao D, Constantinescu A, Hahn EW, Mason RP. Tumor oxygen dynamics with respect to growth and respiratory challenge: investigation of the Dunning prostate R3327-HI tumor. Radiat Res 2001;156(5 Pt 1):510-520.

41. Zhao D, Constantinescu A, Hahn EW, Mason RP. Differential oxygen dynamics in two diverse Dunning prostate R3327 rat tumor sublines (MAT-Lu and HI) with respect to growth and respiratory challenge. Int J Radiat Oncol Biol Phys 2002;53(3):744-756.

42. Kodibagkar VD, Cui W, Merritt ME, Mason RP. Novel 1H NMR approach to quantitative tissue oximetry using hexamethyldisiloxane. Magn Reson Med 2006;55(4):743-748.

43. Kodibagkar VD, Wang X, Pacheco-Torres J, Gulaka P, Mason RP. Proton imaging of siloxanes to map tissue oxygenation levels (PISTOL): a tool for quantitative tissue oximetry. NMR Biomed 2008;21(8):899-907.

44. Zhao D, Constantinescu A, Chang C-H, Hahn EW, Mason RP. Correlation of tumor oxygen dynamics with radiation response of the dunning prostate R3327-HI tumor. Radiation Research 2003;159(5):621-631.

45. Solans C, Izquierdo P, Nolla J, Azemar N, Garcia-Celma MJ. Nano-emulsions. Current Opinion in Colloid & Interface Science 2005;10(3,4):102-110.

46. Sokol RJ, Butler-Simon N, Conner C, Heubi JE, Sinatra FR, Suchy FJ, Heyman MB, Perrault J, Rothbaum RJ, Levy J, et al. Multicenter trial of d-alpha-tocopheryl polyethylene glycol 1000 succinate for treatment of vitamin E deficiency in children with chronic cholestasis. Gastroenterology 1993;104(6):1727-1735.

47. Rajebahadur M, Zia H, Nues A, Lee C. Mechanistic study of solubility enhancement of nifedipine using vitamin E TPGS or solutol HS-15. Drug Deliv 2006;13(3):201-206.

48. Pan SH, Lopez RR, Jr., Sher LS, Hoffman AL, Podesta LG, Makowka L, Rosenthal P. Enhanced oral cyclosporine absorption with water-soluble vitamin E early after liver transplantation. Pharmacotherapy 1996;16(1):59-65.

49. Feng SS, Mu L, Win KY, Huang G. Nanoparticles of biodegradable polymers for clinical administration of paclitaxel. Curr Med Chem 2004;11(4):413-424.

50. Dintaman JM, Silverman JA. Inhibition of P-glycoprotein by D-alpha-tocopheryl polyethylene glycol 1000 succinate (TPGS). Pharm Res 1999;16(10):1550-1556.

51. Coon JS, Knudson W, Clodfelter K, Lu B, Weinstein RS. Solutol HS 15, nontoxic polyoxyethylene esters of 12-hydroxystearic acid, reverses multidrug resistance. Cancer Res 1991;51(3):897-902.

52. Subedi RK, Kang KW, Choi HK. Preparation and characterization of solid lipid nanoparticles loaded with doxorubicin. Eur J Pharm Sci 2009;37(3-4):508-513.

53. Yu JX, Kodibagkar VD, Cui W, Mason RP. 19F: a versatile reporter for non-invasive physiology and pharmacology using magnetic resonance. Curr Med Chem 2005;12(7):819-848.

54. Kaneda MM, Caruthers S, Lanza GM, Wickline SA. Perfluorocarbon nanoemulsions for quantitative molecular imaging and targeted therapeutics. Ann Biomed Eng 2009;37(10):1922-1933.

55. MacDonald RC, MacDonald RI, Menco BP, Takeshita K, Subbarao NK, Hu LR. Small-volume extrusion apparatus for preparation of large, unilamellar vesicles. Biochim Biophys Acta 1991;1061(2):297-303.

56. Kueng W, Silber E, Eppenberger U. Quantification of cells cultured on 96-well plates. Analytical Biochemistry 1989;182(1):16-19.

57. Webster A.J, Cates M.E. Osmotic stabilization of concentrated emulsions and foams. Langmuir 2001;17(3):595-608.

58. Mason T.G, Wilking J. N, Meleson K, Chang C.B, Graves S.M. Nanoemulsions: formation, structure, and physical properties. Journal of Physics: Condensed Matter 2006;18:R635–R666.

59. Parhami P, Fung BM. F-19 Relaxation Study of Perfluoro Chemicals as Oxygen Carriers. J Phys Chem-Us 1983;87(11):1928-1931.

60. McKinley BA, Butler BD. Comparison of skeletal muscle PO2, PCO2, and pH with gastric tonometric P(CO2) and pH in hemorrhagic shock. Crit Care Med 1999;27(9):1869-1877.

61. Seiyama A, Shiga T, Maeda N. Temperature effect on oxygenation and metabolism of perfused rat hindlimb muscle. Adv Exp Med Biol 1990;277:541-547.

62. Sostaric JZ, Pandian RP, Bratasz A, Kuppusamy P. Encapsulation of a highly sensitive EPR active oxygen probe into sonochemically prepared microspheres. J Phys Chem B 2007;111(12):3298-3303.

63. Vahidi N, Clarkson RB, Liu KJ, Norby SW, Wu M, Swartz HM. In vivo and in vitro EPR oximetry with fusinite: a new coal-derived, particulate EPR probe. Magn Reson Med 1994;31(2):139-146.

64. Diepart C, Jordan BF, Gallez B. A New EPR oximetry protocol to estimate the tissue oxygen consumption in vivo. Radiat Res 2009;172(2):220-225.

65. Diepart C, Magat J, Jordan BF, Gallez B. In vivo mapping of tumor oxygen consumption using (19) F MRI relaxometry. NMR Biomed 2011;24(5):458-463.

66. Schultz K, Mollgaard B, Fisher AN, Illum L, Larsen C. Intramuscular rate of disappearance of oily vehicles in rabbits investigated by gamma-scintigraphy. Int J Pharm 1998;169(1):121-126.

67. Higuchi M, Fokin A, Masters TN, Robicsek F, Schmid-Schonbein GW. Transport of colloidal particles in lymphatics and vasculature after subcutaneous injection. J Appl Physiol 1999;86(4):1381-1387.

68. Hockel M, Vaupel P. Tumor hypoxia: definitions and current clinical, biologic, and molecular aspects. J Natl Cancer Inst 2001;93(4):266-276.

69. He F, Deng X, Wen B, Liu Y, Sun X, Xing L, Minami A, Huang Y, Chen Q, Zanzonico PB, Ling CC, Li GC. Noninvasive molecular imaging of hypoxia in human xenografts:

comparing hypoxia-induced gene expression with endogenous and exogenous hypoxia markers. Cancer Res 2008;68(20):8597-8606.

70. Russell J, Carlin S, Burke SA, Wen B, Yang KM, Ling CC. Immunohistochemical detection of changes in tumor hypoxia. Int J Radiat Oncol Biol Phys 2009;73(4):1177-1186.

71. Kedderis GL, Miwa GT. The metabolic activation of nitroheterocyclic therapeutic agents. Drug Metab Rev 1988;19(1):33-62.

72. Begg AC, Sheldon PW, Foster JL. Demonstration of radiosensitization of hypoxic cells in solid tumours by metronidazole. Br J Radiol 1974;47(559):399-404.

73. Sheldon PW, Foster JL, Fowler JF. Radiosensitization of C3H mouse mammary tumours by a 2-nitroimidazole drug. Br J Cancer 1974;30(6):560-565.

74. Brown JM. Selective radiosensitization of the hypoxic cells of mouse tumors with the nitroimidazoles metronidazole and Ro 7-0582. Radiat Res 1975;64(3):633-647.

75. Hodgkiss RJ. Use of 2-nitroimidazoles as bioreductive markers for tumour hypoxia. Anticancer Drug Des 1998;13(6):687-702.

76. Nunn A, Linder K, Strauss HW. Nitroimidazoles and imaging hypoxia. Eur J Nucl Med 1995;22(3):265-280.

77. Piert M, Machulla HJ, Picchio M, Reischl G, Ziegler S, Kumar P, Wester HJ, Beck R, McEwan AJ, Wiebe LI, Schwaiger M. Hypoxia-specific tumor imaging with 18F-fluoroazomycin arabinoside. J Nucl Med 2005;46(1):106-113.

78. Evans SM, Kachur AV, Shiue CY, Hustinx R, Jenkins WT, Shive GG, Karp JS, Alavi A, Lord EM, Dolbier WR, Jr., Koch CJ. Noninvasive detection of tumor hypoxia using the 2-nitroimidazole [18F]EF1. J Nucl Med 2000;41(2):327-336.

79. Rojas-Quijano FA. Synthesis and characterization of contrast agents for targeted magnetic resonance imaging University of Texas at Dallas; 2008.

80. Aime S, Crich SG, Gianolio E, Giovenzana GB, Tei L, Terreno E. High sensitivity lanthanide(III) based probes for MR-medical imaging. Coordin Chem Rev 2006;250(11-12):1562-1579.

81. Sherry AD, Brown RD, Geraldes CFG, Koenig SH, Kuan KT, Spiller M. Synthesis and Characterization of the Gadolinium (3+) Complex of Dota-Propylamide - a Model Dota-Protein Conjugate. Inorganic Chemistry 1989;28(3):620-622.

82. Aime S, Anelli PL, Botta M, Fedeli F, Grandi M, Paoli P, Uggeri F. Synthesis, Characterization, and 1/T(1) Nmrd Profiles of Gadolinium(Iii) Complexes of Monoamide Derivatives of Dota-Like Ligands - X-Ray Structure of the 10-[2-[[2-Hydroxy-1-(Hydroxymethyl)Ethyl]Amino]-1-[(Phenylmethoxy)Methyl]-2-Oxo-Ethyl]-1,4,7,10-Tetraazacyclododecane-1,4,7-Triacetic Acid Gadolinium(Iii) Complex. Inorganic Chemistry 1992;31(12):2422-2428.

83. Norman TJ, Smith FC, Parker D, Harrison A, Royle L, Walker CA. Synthesis and Biodistribution of in-111, Ga-67 and Gd-153-Radiolabeled Conjugates of Nitroimidazoles with Bifunctional Complexing Agents - Imaging Agents for Hypoxic Tissue. Supramol Chem 1995;4(4):305-308.

84. Jounaidi Y, Waxman DJ. Combination of the bioreductive drug tirapazamine with the chemotherapeutic prodrug cyclophosphamide for P450/P450-reductase-based cancer gene therapy. Cancer Res 2000;60(14):3761-3769.

85. Kirkpatrick JP, Cardenas-Navia LI, Dewhirst MW. Predicting the effect of temporal variations in PO2 on tumor radiosensitivity. Int J Radiat Oncol Biol Phys 2004;59(3):822-833.

86. Zhao D, Ran S, Constantinescu A, Hahn EW, Mason RP. Tumor oxygen dynamics: correlation of in vivo MRI with histological findings. Neoplasia 2003;5(4):308-318.

87. Tai YC, Chatziioannou AF, Yang Y, Silverman RW, Meadors K, Siegel S, Newport DF, Stickel JR, Cherry SR. MicroPET II: design, development and initial performance of an improved microPET scanner for small-animal imaging. Phys Med Biol 2003;48(11):1519-1537.

88. Cho H, Ackerstaff E, Carlin S, Lupu ME, Wang Y, Rizwan A, O'Donoghue J, Ling CC, Humm JL, Zanzonico PB, Koutcher JA. Noninvasive multimodality imaging of the tumor microenvironment: registered dynamic magnetic resonance imaging and positron emission tomography studies of a preclinical tumor model of tumor hypoxia. Neoplasia 2009;11(3):247-259, 242p following 259.

89. Gilad AA, Winnard PT, Jr., van Zijl PC, Bulte JW. Developing MR reporter genes: promises and pitfalls. NMR Biomed 2007;20(3):275-290.

90. Contag CH, Ross BD. It's not just about anatomy: in vivo bioluminescence imaging as an eyepiece into biology. J Magn Reson Imaging 2002;16(4):378-387.

91. Hoffman R. Green fluorescent protein imaging of tumour growth, metastasis, and angiogenesis in mouse models. Lancet Oncol 2002;3(9):546-556.

92. de Almeida RA, Burgess D, Shema R, Motlekar N, Napper AD, Diamond SL, Pavitt GD. A Saccharomyces cerevisiae cell-based quantitative beta-galactosidase assay compatible with robotic handling and high-throughput screening. Yeast 2008;25(1):71-76.

93. Kruger A, Schirrmacher V, Khokha R. The bacterial lacZ gene: An important tool for metastasis research and evaluation of new cancer therapies. Cancer Metastasis Rev 1999;17:285-294.

94. Chilvers KF, Perry JD, James AL, Reed RH. Synthesis and evaluation of novel fluorogenic substrates for the detection of bacterial beta-galactosidase. J Appl Microbiol 2001;91(6):1118-1130.

95. Eustice DC, Feldman PA, Colberg-Poley AM, Buckery RM, Neubauer RH. A sensitive method for the detection of beta-galactosidase in transfected mammalian cells. Biotechniques 1991;11(6):739-740, 742-733.

96. Pocsi I, Taylor SA, Richardson AC, Smith BV, Price RG. Comparison of several new chromogenic galactosides as substrates for various beta-D-galactosidases. Biochim Biophys Acta 1993;1163(1):54-60.

97. Josserand V, Texier-Nogues I, Huber P, Favrot MC, Coll JL. Non-invasive in vivo optical imaging of the lacZ and luc gene expression in mice. Gene Ther 2007;14(22):1587-1593.

98. Li L, Zemp RJ, Lungu G, Stoica G, Wang LV. Photoacoustic imaging of lacZ gene expression in vivo. J Biomed Opt 2007;12(2):020504.

99. Tung CH, Zeng Q, Shah K, Kim DE, Schellingerhout D, Weissleder R. In vivo imaging of beta-galactosidase activity using far red fluorescent switch. Cancer Res 2004;64(5):1579-1583.

100. Celen S, Deroose C, de Groot T, Chitneni SK, Gijsbers R, Debyser Z, Mortelmans L, Verbruggen A, Bormans G. Synthesis and evaluation of 18F- and 11C-labeled phenyl-galactopyranosides as potential probes for in vivo visualization of LacZ gene expression using positron emission tomography. Bioconjug Chem 2008;19(2):441-449.

101. Lee KH, Byun SS, Choi JH, Paik JY, Choe YS, Kim BT. Targeting of lacZ reporter gene expression with radioiodine-labelled phenylethyl-beta- d-thiogalactopyranoside. Eur J Nucl Med Mol Imaging 2004;31(3):433-438.

102. Chang YT, Cheng CM, Su YZ, Lee WT, Hsu JS, Liu GC, Cheng TL, Wang YM. Synthesis and characterization of a new bioactivated paramagnetic gadolinium(III) complex [Gd(DOTA-FPG)(H2O)] for tracing gene expression. Bioconjug Chem 2007;18(6):1716-1727.

103. Louie AY, Huber MM, Ahrens ET, Rothbacher U, Moats R, Jacobs RE, Fraser SE, Meade TJ. In vivo visualization of gene expression using magnetic resonance imaging. Nat Biotechnol 2000;18(3):321-325.

104. Cui W, Liu L, Kodibagkar VD, Mason RP. S-Gal, a novel 1H MRI reporter for beta-galactosidase. Magn Reson Med 2010;64(1):65-71.

105. Cui W, Otten P, Li Y, Koeneman KS, Yu J, Mason RP. Novel NMR approach to assessing gene transfection: 4-fluoro-2-nitrophenyl-beta-D-galactopyranoside as a prototype reporter molecule for beta-galactosidase. Magn Reson Med 2004;51(3):616-620.

106. Kodibagkar VD, Yu J, Liu L, Hetherington HP, Mason RP. Imaging beta-galactosidase activity using 19F chemical shift imaging of LacZ gene-reporter molecule 2-fluoro-4-nitrophenol-beta-D-galactopyranoside. Magn Reson Imaging 2006;24(7):959-962.

107. Yu J, Otten P, Ma Z, Cui W, Liu L, Mason RP. Novel NMR platform for detecting gene transfection: synthesis and evaluation of fluorinated phenyl beta-D-galactosides with potential application for assessing LacZ gene expression. Bioconjug Chem 2004;15(6):1334-1341.

108. Yu JX, Kodibagkar VD, Liu L, Mason RP. A 19F-NMR approach using reporter molecule pairs to assess beta-galactosidase in human xenograft tumors in vivo. NMR Biomed 2008;21(7):704-712.

109. Yu JX, Kodibagkar VD, Gulaka PG, Liu L, Mason RP. Development of novel Fe - based ^{1}H MRI *lacZ* gene reporters for *in vivo* assessment. 2008; Nice, France.

110. Sinnott ML. Catalytic Mechanisms of Enzymatic Glycosyl Transfer. Chem Rev 1990;90(7):1171-1202.

111. Bengtsson NE, Brown G, Scott EW, Walter GA. lacZ as a genetic reporter for real-time MRI. Magn Reson Med 2010;63(3):745-753.

112. Shamis M, Barbas CF, Shabat D. A new visual screening assay for catalytic antibodies with retro-aldol retro-Michael activity. Bioorg Med Chem Lett 2007;17(5):1172-1175.

113. Richardson N, Davies JA, Raduchel B. Iron(III)-based contrast agents for magnetic resonance imaging. Polyhedron 1999;18(19):2457-2482.

114. Schwert DD, Davies JA, Richardson N. Non-gadolinium-based MRI contrast agents. Top Curr Chem 2002;221:165-199.

115. Richardson DR. Molecular mechanisms of iron uptake by cells and the use of iron chelators for the treatment of cancer. Curr Med Chem 2005;12(23):2711-2729.

116. Schwert DD, Richardson N, Ji GJ, Raduchel B, Ebert W, Heffner PE, Keck R, Davies JA. Synthesis of two 3,5-disubstituted sulfonamide catechol ligands and evaluation of their iron(III) complexes for use as MRI contrast agents. J Med Chem 2005;48(23):7482-7485.

117. Davies JA, Dutremez SG, Hockensmith CM, Keck R, Richardson N, Selman S, Smith DA, Ulmer CW, Wheatley LS, Zeiss J. Iron-based second-sphere contrast agents for magnetic resonance imaging: Development of a model system and evaluation of iron(III) tris (tironate) complex in rats. Acad Radiol 1996;3(11):936-945.

118. Raymond KN, Muller G, Matzanke BF. Complexation of Iron by Siderophores - a Review of Their Solution and Structural Chemistry and Biological Function. Top Curr Chem 1984;123:49-102.

119. Haas KL, Franz KJ. Application of Metal Coordination Chemistry To Explore and Manipulate Cell Biology. Chem Rev 2009;109(10):4921-4960.

120. Sears P, Wong CH. Carbohydrate mimetics: A new strategy for tackling the problem of carbohydrate-mediated biological recognition. Angew Chem Int Edit 1999;38(16):2301-2324.

121. Hallac RR, Kodibagkar VD, Yu JX, Mason RP. Dual ^{1}H and ^{19}F MR *lac*Z gene reporter molecule. 2010; Stockholm, Sweden. p 1886.

BIOGRAPHICAL INFORMATION

Praveen Kumar Gulaka was born on June 13, 1984 in Andhra Pradesh, India. He received his Bachelor of Technology (B.Tech) degree in Biomedical Engineering from Jawaharlal Nehru Technological University (JNTU), Hyderabad, India in May 2005. In Fall 2005, he started his graduate studies in the Joint Program in Biomedical Engineering at the University of Texas at Arlington and University of Texas Southwestern Medical Center at Dallas and graduated with a Master of Science degree in Summer 2007. In Fall 2007, he started his Doctoral studies in the same program completing it by Summer 2011. His research interests include development of multimodal cancer imaging strategies that provide diverse information about the tumor microenvironment, quantify therapy and aid in prognosis. His projects so far have focused on developing magnetic resonance imaging (MRI) methods to assess tissue oxygenation (using ^{1}H and ^{19}F MR), gene expression and perfusion using targeted contrast agents or reporter molecules, as well as optical imaging methods for the classification of biliary tissues.